A REMARKABLE ADAPTIVE PARADIGM OF HEART PERFORMANCE AND PROTECTION EMERGES IN RESPONSE TO THE CONSTITUTIVE CHALLENGE of MARKED CARDIAC-SPECIFIC OVEREXPRESSION OF ADENYLYL CYCLASE TYPE 8

Kirill V. Tarasov[1], Khalid Chakir[1], Daniel R. Riordon[1], Alexey E. Lyashkov[2], Ismayil Ahmet[1], Maria Grazia Perino[1], Allwin Jennifa Silvester[1], Jing Zhang[1], Mingyi Wang[1], Yevgeniya O. Lukyanenko[2], Jia-Hua Qu[1], Miguel Calvo-Rubio Barrera[2], Magdalena Juhaszova [1], Yelena S Tarasova[1], Bruce Ziman[1], Richard Telljohann[1], Vikas Kumar[1], Mark Ranek[3], John Lammons[1], Rostislav Beshkov[1], Rafael deCabo[2], Seungho Jun[3], Gizem Keceli[3], Ashish Gupta[3], Dongmei Yang[1], Miguel A. Aon[1], Luigi Adamo[3], Christopher H. Morrell[1], Walter Otu[1], Cameron Carroll[1], Shane Chambers[1], Nazareno Paolocci[3], Thanh Huynh[5], Karel Pacak[5], Robert G Weiss[3], Loren Field[4], Steven J. Sollott[1] and Edward G Lakatta[1]*.

[1] LABORATORY of CARDIOVASCULAR SCIENCE, [2]TRANSLATIONAL GERONTOLOGY BRANCH, INTRAMURAL RESEARCH PROGRAM, NATIONAL INSTITUTE ON AGING, NATIONAL INSTITUTES OF HEALTH, BALTIMORE, MARYLAND,
[3] DIVISION OF CARDIOLOGY, DEPARTMENT OF MEDICINE, JOHNS HOPKINS UNIVERSITY SCHOOL OF MEDICINE, BALTIMORE, MD 21205, USA

[4] KRAENNERT INSTITUTE OF CARDIOLOGY, INDIANNA UNIVERSITY SCHOOL OF MEDICINE, INDIANAPOLIS, INDIANA

[5] SECTION ON MEDICAL NEUROENDOCRINOLOGY, EUNICE KENNEDY SHRIVER NATIONAL INSTITUTE OF CHILD HEALTH AND HUMAN DEVELOPMENT, NIH, BETHESDA, MARYLAND, USA

* Corresponding author

Abstract

Adult mice with cardiac-specific overexpression of adenylyl cyclase (AC) type VIII (TG^{AC8}) adapt to an incessantly increased cAMP-induced cardiac workload (~30% increases in heart rate, ejection fraction and cardiac output) for up to a year without signs of heart failure or excessive mortality. Here we show that despite markedly increased cardiac work, classical cardiac hypertrophy markers were absent in TG^{AC8}, total left ventricular (LV) mass was not increased: a reduced LV cavity volume in TG^{AC8} was encased by thicker LV walls harboring an increased number of small cardiac myocytes and a network of small interstitial non-cardiac myocytes, manifesting increased proliferation markers and compared to WT. Protein synthesis, proteosome activity, autophagy, and Nrf-2, Hsp90α, ACC2 protein levels were increased in TG^{AC8}, but LV ATP and phosphocreatine levels in vivo did not differ by genotype. 2,323 transcripts and 2,184 proteins identified in unbiased omics analyses, spanning a wide array of biological processes and molecular functions in numerous cellular compartments differed in TG^{AC8} vs WT; and over 250 canonical signaling pathways characteristic of adaptive survival circuitry of cancers, including PI3K and growth factor signaling, cytokine and T cell receptor signaling, immune responses, ROS scavenging, proliferation, protection from apoptosis, and nutrient sensing, were activated in TG^{AC8}; and compared to WT there was a shift from fatty acid oxidation to increased aerobic glycolysis in the context of increased utilization of the pentose phosphate shunt and nucleotide synthesis. Thus, the adaptive paradigm, that becomes activated in the LV of TG^{AC8} in response to severe chronic, intense AC/PKA/Ca^{2+} signaling embodies many hallmarks of cancer.

Introduction

Adaptations have evolved in all organisms to cope with both acute and chronic internal and environmental stress. For example, even during acute exercise increased autonomic sympathetic-mediated AC/cAMP/PKA/Ca^{2+} signaling, the quintessential mediator of both acute and chronic stress, also activates acute physiologic adaptations to moderate the exercise-induced increase in sympathetic signaling. In response to repeated bouts of acute exercise induced AC/cAMP/PKA/Ca^{2+} stress chronic adaptations emerge (endurance exercise conditioning).[1,2,3]

Prolonged and intense chronic cAMP-mediated stress in experimental animal models results in cardiomyopathy and death.[4,5] During chronic pathophysiologic states e.g. chronic heart failure (CHF) in humans, AC/cAMP/PKA/Ca^{2+} signaling progressively increases as the degree of heart failure progresses, leading to cardiac inflammation, mediated in part, by cyclic-AMP-induced up- regulation of renin-angiotensin system (RAS) signaling. Standard therapies for CHF include β-adrenoreceptor blockers and RAS inhibitors,[6,7] which although effective, are suboptimal in amelioration of heart failure progression.

One strategy to devise novel and better therapies for heart failure, would be to uncover the full spectrum of consilient cardio- protective adaptations that can emerge in response to severe, chronic AC/cAMP/PKA/Ca^{2+} -induced cardiac stress. The young adult TG^{AC8} heart in which cardiac-specific over expression in mice of Adenylyl Cyclase (AC) Type 8, driven by the α myosin heavy chain promoter, markedly enhances AC activity and cAMP signaling, may be an ideal model in which to elucidate the features of a wide-spread an adaptive paradigm that must become engaged in response to incessant chronic activation of cardiac AC/cAMP/PKA/Ca^{2+} signaling. Specifically, concurrent with chronically increased AC activity within the young adult TG^{AC8} sinoatrial node

68 (SAN) and LV,[8,9] increased heart rate (HR), measured via telemetry in the awake, unrestrained
69 state, increased by approximately 30%, persisting in the presence of dual autonomic blockade;[8]
70 and LV EF is also markedly increased in TG^{AC8}.[10] Thus, the cardiac phenotype of the adult TG^{AC8}
71 mimics cardiac responses to AC/cAMP/PKA/Ca^{2+} sympathetic autonomic input during strenuous,
72 acute exercise, but this stressful state persists incessantly. [8] Although this incessant high cardiac
73 load imposes a severe chronic stress on the heart that might be expected to lead to the near term
74 heart failure and demise,[11, 12] adult TG^{AC8} mice maintain this remarkable, hyperdynamic cardiac
75 phenotype up to about a one year of age,[9,13,14,10] when signs of CHF begin to develop and
76 cardiomyopathy ensues.[10]

77 We hypothesized, (1) that a panoply of intrinsic adaptive mechanisms become *concurrently*
78 engaged in order to protect the TG^{AC8} heart during the incessant, high level of cardiac work in
79 several months, and (2) that, some of these mechanisms are those that become activated in the
80 endurance, trained heart, including shifts in mechanisms of energy generation, enhanced protein
81 synthesis and quality control, and increased defenses against reactive O_2 species (ROS) and cell
82 death.[15,16] We reasoned that a discovery bioinformatics approach in conjunction with a deeper
83 phenotypic characterization of TG^{AC8} LV, would generate a number of testable hypotheses about
84 the characteristics of some of these mechanisms utilized to sustain this adaptive paradigm of heart
85 performance and protection in response to severe, chronic adenylyl cyclase-induced cardiac stress.
86 To this end, we performed unbiased, RNASEQ and proteomic analyses of adult TG^{AC8} and WT
87 LVs, and selectively validated genotypic differences in numerous transcripts and proteins. Our
88 results delineate an emergent consilient pattern of adaptations within the TG^{AC8} heart in response
89 to chronically increased AC/cAMP/PKA/Ca^{2+}-signaling and offer numerous testable hypotheses

to further define the details of mechanisms that underlie what we will show here to be a remarkable adaptive heart paradigm.

Materials and Methods

Mice

All studies were performed in accordance with the Guide for the Care and Use of Laboratory Animals published by the National Institutes of Health (NIH Publication no. 85-23, revised 1996). The experimental protocols were approved by the Animal Care and Use Committee of the National Institutes of Health (protocol #441-LCS-2019). A breeder pair of TG^{AC8} over expression mice, generated by ligating the murine α-myosin heavy chain promoter to a cDNA coding for human TG^{AC8}, were a gift from Nicole Defer/Jacques Hanoune, Unite de Recherches, INSERM U- 99, Hôpital Henri Mondor, F-94010 Créteil, France.[9] Mice were bred adult (3 mo) and housed in a climate-controlled room with 12-hour light cycle and free access to food and water, as previously described.[8]

Detailed methodology for RNASEQ and LV Proteome analyses, WB and RT-qPCR analyses, echocardiography, heart and cardiac tissue isolation, isolated perfused working heart experiments, nuclear EdU and BrdU uptake in cells within LV tissue, adenyl cyclase activity, immunohistochemistry, protein synthesis, misfolding and degradation, autophagy, NMR spectroscopy, transmission electron microscopy, mitochondrial permeability transition threshold, are provided in the online supplement.

110 # Results

111 ## Cardiac Structure and Performance.

112 We performed echocardiography and cardiac histology for in-depth characterization of the
113 TG^{AC8} heart structure and function. Representative echocardiograms of TG^{AC8} and WT are
114 illustrated in **Fig.S1**, selected Echo parameters are shown in **Fig. 1**, (and a complete listing of
115 parameters is provided in **Table S.1)**. Both EF and HR were higher in TG^{AC8} than in WT (**Fig. 1**
116 **A, B**), confirming prior reports.[8,10] Because stroke volume did not differ by genotype (**Fig. 1C**),
117 cardiac output was elevated by 30% in TG^{AC8} (**Fig. 1D**) on the basis of its 30% increase in HR.
118 Arterial blood pressure was only mildly increased in TG^{AC8} averaging 3.5 mmHg higher than in
119 WT (**Fig. 1E**).

120 A sustained high cardiac workload is usually expected to result in an increase of a total LV
121 mass,[1,17,18] i.e., cardiac hypertrophy. Although both the LV posterior wall and inter-ventricular
122 septum were thicker in TG^{AC8} vs WT (indicative of an increased LV wall biomass), (**Fig. 1 F, G**)
123 the LV cavity volume was markedly reduced (**Fig. 1 H, I**), and the echo derived **total** LV mass
124 did not differ by genotype (**Fig. 1 J**). Postmortem measurements indicated that although the body
125 weight did not differ between TG^{AC8} and WT (**Fig. 1 K**), the heart weight/body weight (HW/BW)
126 was even actually, modestly reduced in TG^{AC8} vs WT (**Fig. 1 L**).

127 Pathological hypertrophy markers e.g., β-myosin heavy chain (MYH7), ANP (NPPA) or
128 BNP (NPPB) were not increased in TG^{AC8} vs WT by Western Blot (WB) (**Fig. 2A**); curiously, α
129 skeletal actin, commonly considered to be a pathologic hypertrophy marker, was increased in
130 TG^{AC8} vs WT (**Fig. 2A**). Calcineurin (PP2B), which activates the hypertrophic response by

131 dephosphorylating nuclear factor of activated T cells (NFAT),[19] did not differ in WB of TG^{AC8} vs
132 WT (**Fig. 2A**).

133 LV Histologic Analysis

134 The average LV cardiac myocyte size was smaller in TG^{AC8} compared to WT (**Fig. 2 B,**
135 **C**), and LV myocyte size distribution was different by genotype (**Fig. 2 D**). LV collagen content
136 in TG^{AC8} was not increased vs WT (**Fig. S. 2).**

137 To address the issue of DNA synthesis within LV cardiac myocyte we loaded EdU for 28-
138 days. EdU labeled nuclei, detected in both TG^{AC8} and WT whole mount ventricular preparations
139 were randomly scattered throughout the LV from the mitral annulus to the apex. LV myocyte
140 nuclei, however, were rarely EdU labeled. Rather nearly all EdU labelling was detected in small
141 interstitial cells that expressed vimentin or in cells that enclosed the capillary lumina (**Fig. 3 A-**
142 **G)**, suggesting that EdU was also incorporated within the DNA of endothelial cells in both WT
143 and TG^{AC8}. However, total nuclear EdU labeling was 3-fold higher in TG^{AC8} than in WT **Fig. 3 H**.

144 To monitor cardiomyocyte S-phase activity, TG^{AC8} mice were crossed with MHC-nLAC
145 mice (which express a nuclear-localized β-galactosidase reporter under the transcriptional
146 regulation of the mouse α-cardiac MHC promoter; these mice are useful to identify cardiomyocyte
147 nuclei in histologic sections).[20] The resulting TG^{AC8}, MHC-nLAC double-transgenic mice and
148 MHC-nLAC single-transgenic mice were identified and sequestered. At 28-to-30 days of age, the
149 mice were administered BrdU via drinking water (0.5 mg/ml, changed every 2nd day) for a total
150 of 12 days. There was no difference in the level of ventricular cardiomyocyte S-phase activity in
151 the TG^{AC8}, MHC-nLAC double-transgenic vs. the MHC-nLAC single transgenic animals (**Fig. 3**
152 **H-K**).

153 Thus, the adult TG^{AC8} heart has a hyper-dynamic LV with thicker walls, harboring not only
154 an increased number of small **cardiac** myocytes, but also an increased number of small interstitial
155 cells and endothelial cells with increased EdU labeling vs WT. The LV cavity volumes at both
156 end-diastole and end-systole were markedly reduced, and LV EF was markedly increased in TG^{AC8}
157 vs WT. But, neither **total** LV mass, nor collagen content were increased in TG^{AC8} vs WT and the
158 profile of pathologic cardiac hypertrophy markers in TG^{AC8} was absent.

159 AC/cAMP/PKA/Ca^{2+} signaling

160 Given that the transgene in our study was an AC, we next focused on expected differences
161 in AC/cAMP/PKA/Ca^{2+} signaling in TG^{AC8} vs WT. Immunolabeling of single LV myocytes
162 showed that AC8 expression was markedly increased (by 8-9-fold in TG^{AC8} vs WT), and AC
163 activity (measured in membranes isolated from LV tissue) in TG^{AC8} was 50% higher than that in
164 WT (**Fig. 4 A-C**). Expression of the PKA catalytic subunit was increased by 65.6%, and expression
165 of the regulatory subunit was decreased by 26.7% in TG^{AC8} by WB (**Fig. 4 D, E**). PKA activity
166 was increased by 57.8 % in TG^{AC8} vs WT (**Fig. 4 F**).

167 To search for mechanisms that increase contractility within cardiac myocytes we examined
168 the expression of selected proteins downstream of PKA signaling that are involved in
169 excitation/Ca^{2+} release/contraction/relaxation. Western Blot analysis revealed that a number of
170 proteins that determine increase cardiac myocyte performance were upregulated in TG^{AC8} vs WT,
171 including αMHC (MYH6 by 18.7%), SERCA2 (ATP2A2 by 62.0%), L-type Ca Channel (Cav1.2,
172 by 61.8%), and NCX1 (AKA SLC8A1) by 117.6%, and CaMKII by 35.0% (**Fig. 4 G-K**).
173 Immunolabeling of total RyR2 was increased by 66% in TG^{AC8} vs WT (**Fig. 4 L**). This pattern of
174 increased protein expression consistent with increased Ca^{2+} flux into and out of cardiac myocytes,

175 an increased Ca^{2+} cycling between SR and cytosol, and increased myosin cross-bridge kinetics
176 during heart contraction in TG^{AC8} vs WT.

177 Thus, as would be expected in the context of markedly increased transcription of AC type
178 VIII, AC and PKA protein levels and activities, and levels of proteins downstream of PKA
179 signaling were markedly increased and associated with a chronic, marked increase in LV
180 performance.

181 Myocardial and plasma catecholamines.

182 It is well known, that PKA signaling activates a cascade of enzymes beginning with
183 tyrosine hydroxylase (TH), that results in a production of catecholamines (**Fig. S.3 A**). Among
184 these enzymes, dopamine decarboxylase, which converts DOPA to dopamine, was increased in
185 TG^{AC8} vs WT (**Fig. S.3 B**), dopamine b-hydroxylase, which converts dopamine to norepinephrine
186 did not differe by genotype, and phenylethanolamine N-methyltransferase (PNMT), which
187 converts norepinephrine to epinephrine was reduced in TGAC8 vs WT. In the context of these
188 genotypic differences in enzyme levels LV tissue dopamine was increased and DHPG was reduced
189 and NE was borderline reduced (p=0.08) **Fig. S.3 B**.

190 Interestingly, as noted previosly [8], plasma levels of dopa and dopamine were also incresed
191 in TG^{AC8} vs WT, whereas norepinephrine, epinephrine, DOPAC and DHPG were reduced (**Fig.**
192 **S.3 C**).

193 Protein Synthesis, Degradation and Quality Control

194 Because PKA signaling-driven increased cardiac work is known to be associated with
195 increased protein synthesis,[21, 22] we next compared the rate of protein synthesis in TG^{AC8} and WT
196 LV lysates. Despite the absence of increase of total LV mass, the rate of protein synthesis was

197 40% higher in TG^{AC8} than in WT (**Fig. 5 A**). WB analysis indicated that expression or activation
198 of p21Ras, p-c-Raf, MEK1/2, molecules downstream of PKA signaling that are implicated in
199 protein synthesis, were increased in TG^{AC8} vs WT (**Fig. 5 B-C**). The transcription factor CREB1,
200 involved in PKA signaling directed protein synthesis was increased by 58.1% in TG^{AC8} vs WT in
201 WB analysis (**Fig. 5 D).** Expression of CITED4 (family of transcriptional coactivators that bind to
202 several proteins, including CREB-binding protein (CBP)) was increased by 51 % in TG^{AC8} vs WT
203 in WB analysis (**Fig. 5 E).** Expression of protein kinases, that are required for stress-induced
204 activation of CREB1, MSK1 and MNK1, direct substrates of MAPK, were increased by 40% and
205 48% respectively in TG^{AC8} vs WT (**Fig. 5 F** and **G**).

206 **Autophagy**

207 Proteasome activity within LV lysates was increased in TG^{AC8} vs WT **(Fig. 6 A)**. However,
208 although there was a significant increase in the amount of soluble misfolded proteins in TG^{AC8} vs
209 WT **(Fig. 6 B)**, insoluble protein aggregates did not accumulate within the TG^{AC8} LV (**Fig. 6 C**).
210 This suggest that an increase in micro-autophagy of the TG^{AC8} LV circumvents the potential
211 proteotoxic stress of aggregated protein accumulation, which can negatively impact cardiac cell
212 health and function. A 24% increase in the expression of HSP90α (**Fig. 6 D**) in TG^{AC8} also
213 suggested that chaperone-mediated autophagy was involved in preventing an accumulation of
214 insoluble protein aggregates.

215 We reasoned that another type of protein quality control, macro-autophagy, might also be
216 activated in TG^{AC8} vs WT. Indeed, protein levels of several members of the autophagy machinery
217 were increased in TG^{AC8} vs WT: both ATG13, a factor required for autophagosome formation and
218 mitophagy, and the ubiquitin-protein ligase PARKIN, which protects against mitochondrial
219 dysfunction during cellular stress, by coordinating mitochondrial quality control mechanisms in

220 order to remove/replace dysfunctional mitochondrial components, were significantly increased in
221 TG^{AC8} vs WT (**Fig. 6 E, F)**. Furthermore, protein levels of the cysteine protease ATG4B, involved
222 in processing, and the lipidation/delipidation steps (conjugation/removal of
223 phosphatidylethanolamine) and insertion of MAP1LC3, GABARAPL1, GABARAPL2 and
224 GABARAP into membranes, during autophagy and endocytosis, were also increased (**Fig. 6 G)**.
225 In addition, the catalytic subunit of the PI3Kc3, involved in initiation and maturation of
226 autophagosomes and in endocytosis, was also significantly higher in the TG^{AC8} vs WT (**Fig. 6 H)**.
227 Finally, direct measurements in single LV myocytes showed that autophagolysosomes were
228 appreciably increased in TG^{AC8} vs WT, indicating that autophagy (mitophagy) was activated to
229 the greater extent in the TG^{AC8} vs WT. (**Fig. 6 I, J)**.

230 Mitochondrial Structure

231 We employed transmission electron microscopy (TEM) to directly visualize ultrastructural details
232 of the mitochondria and cardiac myofibers in the LVs of TG^{AC8} and WT. Representative panoramic
233 electron micrographs of LV cardiac muscle fibers and mitochondria in TG^{AC8} and WT are
234 illustrated in **Fig. 7 A and B**. Cardiac myocytes presented a very distinctive morphology with high
235 content of myofibrils and a large number of high-electron dense mitochondria and several
236 capillaries surrounding cardiac myocytes are depicted (see white arrows). Cardiac myocyte
237 ultrastructure is depicted in **Fig. 7** panels **C** and **E**, for WT mice, and in panels **D** and **F**, for TG^{AC8}.
238 Asterisks show swollen, disrupted mitochondria with lighter cristae compared to the surrounding
239 healthy mitochondria. **Fig. 7** Panels **G-J** present quantitative stereological analyses of normal and
240 damaged mitochondria. Although there was a mild increase in the number of damaged
241 mitochondria (0.3 %), and in the percent of cell volume occupied by damaged mitochondria (0.4%)
242 in TG^{AC8}, the numbers of healthy mitochondria and the percent of cell volume occupied by healthy

243 mitochondria did not differ between TG^{AC8} and WT. Nevertheless, the presence of mitochondrial
244 deterioration at a young age is uncommon and may be further evidence for enhanced cleaning and
245 recycling mechanisms such as autophagic signaling, (**Fig.s. 6, 7**).

246 Mitochondrial Fitness

247 The healthy functioning and survival of cardiac myocytes during severe, chronic
248 myocardial stress requires close coordination of survival mechanisms and numerous mitochondrial
249 functions that require a high level of mitochondrial fitness.[23,24,25,26] The mitochondrial permeability
250 transition pore (mPTP) is a key regulator of mitochondrial functions, including energy metabolism
251 (e.g., with the pore performing as a "safety valve", opening transiently and reversibly, to prevent:
252 1) the excessive accumulation of certain regulatory species, such as Ca^{2+}; and 2) bioenergetic
253 byproducts/damaging reactive species, such as free radicals, from achieving toxic levels. The
254 mPTP also regulates cell fate: enduring and irreversible pore opening, plays decisive mechanistic
255 roles in mitochondrial and cell life vs death decisions during normal development or pathological
256 stress (e.g., involving excess and damaging free radical exposure). Measurement of the pore
257 susceptibility or resistance to being induced/opened can serve as a biomarker of mitochondrial
258 fitness. **Fig. 7** panels **M** and **N** shows that the mPTP ROS threshold did not differ in TG^{AC8} vs WT,
259 suggesting a comparable degree of mitochondrial fitness in both genotypes.

260 ROS levels and NRF Signaling.

261 Given the incessantly elevated myocardial contractility and heart rate, and increased
262 protein synthesis and quality control mechanisms in TG^{AC8} vs WT, it might be expected that ROS
263 levels are increased in TG^{AC8}. To this end we measured of superoxide radical accumulation in
264 isolated, perfused, isometrically contracting TG^{AC8} hearts that maintained markedly enhanced
265 cardiac workload observed *in vivo* (**Fig. 8 A-B)**. Superoxide radical accumulation did not differ by

266 genotype**,** suggesting that mechanisms to scavenge ROS are increased in TG^{AC8}. Indeed, the level
267 of NRF2 protein, a key regulator of ROS defense signaling was increased by 24% in TG^{AC8} vs
268 WT, suggesting that increased NRF signaling in the TG^{AC8} LV may be a factor that prevents the
269 accumulation of superoxide ROS.

270 High Energy Phosphates.

271 Given the fact, that increased protein synthesis and quality control mechanisms **(Fig. 6**),
272 maintenance of normal ROS levels (**Fig. 8**) and the incessant high cardiac performance of the
273 TG^{AC8} (**Fig. 1)** require increased energy production**,** it is reasonable to assume that the total energy
274 requirements of the TG^{AC8} LV are probably considerably higher than those in WT. It was
275 important, therefore, to assess high energy phosphate levels in TG^{AC8} and WT. A schematic of
276 ATP-creatine energy system is depicted in **Fig. 9A**. Steady state levels of ATP, phosphocreatine
277 and the ATP: phosphocreatine assessed in *vivo,* were maintained at the same level in TG^{AC8} as in
278 WT (**Fig. 9 B-E**), suggesting that the rate of ATP production in the TG^{AC8} LV is adequate to meet
279 its increased energy demands at least when animals rest.

280 Unbiased RNASEQ and Proteome Analyses

281 We performed unbiased, RNASEQ and proteome analyses of adult TG^{AC8} and WT left
282 ventricles (LV) in order to realize facets of the consilience of adaptive mechanisms beyond those,
283 identified in our experiments illustrated in **Fig.s. 1-9**. We reasoned that taking advantage of the
284 knowledge base within bioinformatic tools would also generate a number of testable hypotheses
285 regarding the components of adaptive paradigm of heart performance and protection in response
286 to the constitutive challenge of marked cardiac-specific overexpression adenylyl cyclase type 8.

287 ## LV Transcriptome (RNASEQ)

288 RNA sequencing identified 11,810 transcripts in LV lysates (**Fig. 10 A**, **Table S.2**); of
289 these, 2,323 were differentially expressed in TG^{AC8} vs WT (**Fig. 10 A** and T**able S.3**): 1,201 were
290 significantly upregulated in TG^{AC8} vs WT, and 1,117 were significantly downregulated. A volcano
291 plot and heatmap of these transcripts are shown in **Fig. S.4 panels A and C**. The transcript
292 abundance of human *ADCY8* in TG^{AC8} (LV) myocardium was more than 100-fold higher than the
293 endogenous mouse isoform (**Fig. S.4 E**).

294 ## The LV Proteome

295 6,834 proteins were identified in the LV proteome (**Fig. 10 A**, **Table S.4**); of these, 2,184
296 were differentially expressed (**Table S.5**) in TG^{AC8} vs WT: 2,026 were upregulated and 158 were
297 downregulated in TG^{AC8}. A Volcano plot and heatmap of the proteome are shown in the **Fig. S.4**
298 panels **B and D**.

299 ## Bioinformatic Analyses of the *Total* Transcriptome and Proteome Datasets

300 We employed WEB-based GEne SeT AnaLysis Toolkit (WebGestalt) and Ingenuity
301 Pathway Analysis (IPA), online platforms for in depth analyses of the total 2,323 expressed
302 transcripts (**Fig. 10 A-a**) and the total 2,184 **(Fig. 10 A-b)** proteins that differed by genotype.

303 In Gene Ontology (GO) analysis WebGestalt classifies submitted molecules into three
304 main categories, i.e., Biological Process (BP), Cellular Component (CC), Molecular Function
305 (MF), (**Fig. 10 B)**. Remarkably, transcriptome and proteome gene ontology (GO) terms that
306 differed by genotype in response to overexpression of a single gene, AC Type 8, covered nearly
307 all the biological processes and molecular functions within nearly all compartments of the TG^{AC8}
308 LV myocardium.

309 In order to discover genotypic differences in canonical signaling pathway enrichment, we
310 performed QIAGEN Ingenuity Pathway Analysis (IPA) of the total number of transcripts (2,323)
311 that were differentially expressed by genotype **(Fig. 10 A-c)** and the total number of proteins
312 (2,184 **Fig. 10 A-d**). In IPA analyses 248 canonical pathways in the transcriptome analyses and
313 308 canonical pathways in the proteome differed by genotype $p<0.05$ in *enrichment* (listed in
314 **Tables S. 6A, B**). 154 pathways in transcriptome or proteome were *activated* by genotype (Z-score
315 calculated) and Spearman's correlation coefficient r_s was 0.57, $p < 0.0001$ **Fig. S.5**, and showed
316 moderate correlation between enriched and activated pathways in transcriptome and proteome

317 Although 60 molecules were represented in only a single enriched pathway, 22 molecules
318 were represented in 10 or more pathways, the highest among these being: MAP3K – (68
319 pathways); MAP2K2 – (51 pathways); and PLCG2 – (33 pathways) (**Table S.6C**). Representation
320 of several differentially expressed molecules in multiple canonical signaling pathways that differed
321 by genotype is a plausible explanation accounting for the consilient pattern of pathway enrichment
322 and activation in the TG^{AC8} heart identified in IPA analyses.

323 The top enriched and activated or inactivated pathways are illustrated in **Fig. 10 C**. Of note,
324 several pathways, e.g., Nrf2 signaling, Integrin Signaling, and Cardiac Hypertrophy Signaling
325 were among the top activated pathways that were highly enriched in TG^{AC8} vs WT, whereas fatty
326 acid β-oxidation, tryptophan degradation III, isoleucine degradation and glutaryl Co-A degradation
327 were markedly suppressed in TG^{AC8} vs WT (**Fig. 10 C**). Surprisingly, the top differentially
328 regulated pathways between TG^{AC8} and WT was "leukocyte extravasation signaling" (**Fig. 10 C**).

329 **Bioinformatic Analyses of Transcripts and Proteins that *Both* Significantly**
330 **Differed by Genotype**

331 544 transcripts and proteins **both** differed by genotype **(Fig. 9A-e, Table S.7A)**. Of these
332 544, 339 (62.32%) were significantly **upregulated** in TG^{AC8}; and 99 (18.2%) were significantly
333 downregulated in TG^{AC8}. Thus, of the 544 transcripts and proteins that **both** significantly differed
334 by genotype, 80.5% differed **concordantly** (in the same direction, **Fig. S.6**).

335 We next subjected these 544 molecules to IPA analysis. 170 of the **same** canonical
336 pathways in the transcriptome and proteome differed by genotype in enrichment. Of these, 118
337 pathways also differed by genotype and activation status (**Table S.7B**).

338 In addition to IPA analyses we also used PROTEOMAP platform[27] to visualize functional
339 categories of the 544 proteins that differed by genotype in **Fig. 10 A-e, Fig. S.6**. PROTEOMAP
340 displays a protein data set as functional trees (**Fig. S.7**), each consisting of a number of polygons,
341 the areas of which reflect genotypic differences in protein abundances. Genotypic differences were
342 most marked by increases in TG^{AC8} of: ENVIRONMENTAL INFORMATION PROCESSING
343 (informing on marked differences by **Rap1** and **PI3K-AKT** signaling pathways, harboring the
344 marked increases in expression of ADCY8 and TNC (tenascin) proteins); GENETIC
345 INFORMATION PROCESSING (informing on PROTEIN **translation, folding, sorting and**
346 **degradation** signaling pathways, harboring marked increases in RNF128, MMP2 and WFS1);
347 and CELLULAR PROCESSES (informing on **vesicular transport** and **exosome**, harboring
348 increased NCF1, LCP1 and CTSZ proteins).

349 PROTEOMAP also identified major genotypic changes in BIOSYNTHESIS AND
350 CENTRAL CARBON METABOLISM (**Fig. S.7**), informing on genotypic differences in:

351 **membrane transport,** harboring increased SLC4A2 (regulates intracellular pH, biliary
352 bicarbonate secretion, and chloride uptake); **other metabolic enzyme proteins** (PDK3, SULF2
353 and ALPK2), and carbohydrate metabolism; and **glycolysis**, harboring reduced ALDH1B1.

354 Regulatory Networks Centered on cAMP and Protein Kinase A Signaling

355 Having confirmed that both AC8 protein and AC activity were markedly increased in
356 TG^{AC8} vs WT (**Fig. 4 B, C**) it was reasonable to infer that the multitude of genotypic differences
357 that were identified in WebGestalt, IPA and PROTEOMAP (**Fig.s. 10 B, S6; Table S.6**) might be
358 ultimately (directly or indirectly) linked to increased signaling driven by the high levels of AC
359 activity. Three main downstream targets of cAMP generated by AC activity are: protein kinase A
360 (**PKA**), guanidine-nucleotide exchange proteins activated by cAMP (**EPACs**), and cyclic
361 nucleotide-gated ion channels (**CNGCs**). We found no evidence of activation for 2 of these 3
362 targets. In fact: 1) Neither CNGC subunits α 1-4, nor β 1-2 transcripts or proteins were identified
363 in our omics analysis; 2) omics analysis (**Table S.2, S4**) provided no evidence to suggest that
364 cAMP directed **Epac** signaling was upregulated in the TG^{AC8} LV. More specifically, transcripts
365 of *Rapgef* 1 thru 6 were significantly **downregulated** in TG^{AC8} vs WT (**Table S.3**) and RAPGEF
366 2, 3 and 5 proteins identified in proteomic analyses did not differ by genotype (**Table S.4**). On the
367 contrary, we found clear evidence of activation of PKA. In fact, we had shown that PKA catalytic
368 subunit and PKA activity are substantially higher in TG^{AC8} vs WT (**Fig. 4 D, F**), and PKA signaling
369 was among the top pathways increased and activated in IPA analysis We therefore next focused
370 the IPA knowledge base on the PKA complex as the center of a number of **interacting** pathways.
371 We noticed that in addition to cAMP, another upstream regulator of PKA signaling, ITGA5, was
372 increased in TG^{AC8} vs WT in both the transcriptome and proteome (**Fig. 11**), suggesting increased
373 crosstalk between intra and extra cellular signaling.

374 To further investigate the role of PKA-signaling in the extreme TG^{AC8} phenotype, we next
375 established the protein interaction network centered on PKA (**Fig. 11**). Gene families of these
376 proteins ranged from transcription regulators, kinases, peptidases and other enzymes to
377 transmembrane receptors, ion channels and other protein families (CFH, CD44, HOMER1, and
378 SERPINF1). Although CREB1 protein was not identified in proteome analyses, as noted this
379 canonical transcription factor, and its phosphorylated form activated by PKA were markedly
380 increased in WB analyses (**Fig.s. 5 D**, **S.11 B**). Canonical signaling pathways in which these
381 proteins operate and downstream biological and molecular processes of proteins in these pathways
382 are listed in **Fig. 11** (lower part). See **Table S.8** for the full list of these downstream effects.

383 Shifts in Metabolism

384 The enrichment or activation of the large number of signaling pathways in TG^{AC8} vs WT
385 (**Fig. 10 C, S.6; Table S.6 A, B**) suggested that some aspects of metabolism differed by genotype.
386 A detailed schematic of the genotypic differences in transcripts and proteins that related to
387 metabolism circuits is illustrated in **Fig. 12,** and WB validations of selected proteins are presented
388 in **Fig. S.8.** Bioinformatic analyses suggested that nutrient sensing pathways, including AMPK,
389 insulin and IGF signaling, that induce shifts in aerobic energy metabolism were activated in TG^{AC8}
390 vs WT LV. A close inspection of the bioinformatic analyses of central carbon metabolic processes
391 (**Fig. 12**) suggested that catabolism of glucose is markedly increased in TG^{AC8} vs WT, while the
392 fatty acid β oxidation pathway is concurrently reduced.

393 An increase in myocardial glucose metabolism in TG^{AC8} vs WT was suggested by increases
394 in GLUT1, HK1, GSK3B, GYS1 and PFK, PGK1, PGA and PKM. Interestingly, bioinformatic
395 analyses suggested that, both transcript (down by 86%) and protein (down by 38%) expression of
396 ALDOB were reduced in TG^{AC8} vs WT. Signals related to reduced fatty acid oxidation (FAO)

397 likely stem from reductions in CPT1, CPT2, ACAT1, HADH, HADHA, and HADHB (**Fig. 12**).
398 Further, signals from bioinformatic analyses pointed to reduced utilization of the TCA cycle and
399 mitochondrial respiration within the TG^{AC8} LV vs WT **(Fig. 12)**. Interestingly, omics signals
400 suggested that the malate-aspartate shuttle (MAS), which results in the net transport H+ from
401 cytosol back to the mitochondria, may be suppressed in TG^{AC8} vs WT, because transcripts of *Ldhb,*
402 *Mpc1, Mpc2, Mdh1, Got1, Slc25a11 Slc25a13*, and SLC25A13 protein was also downregulated
403 (**Fig.s. 12, S.9**). Reduced shuttling of aspartate into mitochondria in conjunction with increased
404 level of ACC2 (**Fig. S.10 A, B**) would favor with increased nucleotide synthesis. [28, 29]

405 The results of bioinformatic analyses also pointed to increased expression, in TG^{AC8} vs
406 WT, of the glucose transporter, lactic acid dehydrogenase type A and the glutamine transporter,
407 that are required for enhanced aerobic glycolysis[30] (**Fig. 12**). **Enhanced growth factor** and other
408 PI3K/AKT driven signaling processes in TG^{AC8} suggested by omics analyses (**Fig. 12)** and
409 validated by WB (**Fig. S.8)** are tightly linked to aerobic glycolysis and utilization of pentose
410 phosphate shunt (PPS).[30] Increased utilization of the PPS in TG^{AC8} vs WT is suggested by increases
411 in both the expression of transcripts and proteins of G6PDH, PGD and PRPS2 (**Fig. 12**).

412 Because Acetyl-CoA carboxylase (ACC), a complex multifunctional enzyme system that
413 catalyzes the carboxylation of acetyl-CoA to malonyl-CoA, which limits CPT1 transport of FA
414 into the mitochondria, we inquired whether, in addition to reduction in CPT1 transcripts and
415 reductions in CPT1 and CPT2 proteins in TG^{AC8} vs WT, ACC2 might also be increased in TG^{AC8}
416 LV myocytes. Indeed, immunolabeling of isolated LV cardiomyocytes indicated a clear increased
417 in ACC2 (AKA ACACB) protein expression (**Fig. S.10 A**); and in increase *Acc1* (AKA *Acaca*)
418 mRNA was documented in LV tissue by RT-qPCR (**Fig. S.10 B**). Such an increase of ACC2
419 expression in TG^{AC8} may not only explain a shift from FAO to glucose utilization within the TG^{AC8}

420 LV but may also explain increased utilization of Aerobic glycolysis in TG^{AC8} vs WT, which is
421 linked enhanced utilization of PPS to increase anabolic processes such as nucleotide synthesis
422 (**Fig. 12**). Because it is known that *Acc2* deletion increases FAO and suppresses glucose utilization
423 in the context of LV pressure overload, [28, 29] it is important to recall that cardiac myocytes within
424 TG^{AC8} LV are smaller in size, and not enlarged as those in pathologic cardiac hypertrophy in
425 response to LV pressure overload, [31] and in which ACC2 promotes glucose utilization and reduces
426 FAO.[28, 29] In other terms, an increase in ACC2 appears to promote enhanced glucose utilization,
427 enhanced aerobic glycolysis, enhanced utilization of the PPS, and reduced FAO, and may be
428 involved in the reduction of average LV cardiac myocyte size in TG^{AC8}, and the absence of markers
429 of pathologic hypertrophy within the TG^{AC8} LV.

430 A Schematic of the Circuitry of Enhanced Cardiac Performance and Adaptive 431 Mechanisms within the TG^{AC8} LV Derived from Phenotypic Characterization 432 and Signals from Bioinformatic Analyses

433 **Fig. 13** depicts a hypothetical scheme of physiologic performance and protection circuits
434 that appeared to be concurrently engaged within the TG^{AC8} LV. Because many of the perspectives
435 depicted in the scheme in **Fig. 13** were derived from bioinformatic analyses of cell lysates, it is not
436 implied that all of these circuits are present within the same cell types that reside in the heart (see
437 Discussion). Although the pathways/specific targets and the effector functions/outcomes
438 culminating from the regulation of the components within the circuits in the pathways are
439 represented according to published literature with respect to cardiac-specific context. The circuits
440 (**Fig. 13**) are based upon defined LV phenotypic characteristics (**Fig.s. 1 - 9**, **Fig. S.1, S2, S.9** and
441 **Table S.1**), on signals derived from genotypic differences in transcriptome and proteome and IPA
442 analyses (**Fig.s. 10** and **11, Tables S.2-S.6**), on selected WB, RT-qPCR and immunolabeling

443 analyses performed prior to and following transcriptome and proteome bioinformatic analyses, and
444 WB analyses (**Fig.s. 2, 4-6, 8, S.10, S.15**), and on additional selected post-hoc WB, RT-qPCR
445 (**Fig. S.8-S.12**), performed having visualized the consilience of pathways depicted within the
446 circuit schematic in **Fig. 13**.

447 Discussion

448 Cardiac Structure and Contractile Performance Circuitry.

449 Because it is well known that alterations in heart structure and increased performance in
450 the TG^{AC8} vs WT measured in vivo (**Fig. 1 and S.1, Table S1)** and depicted in the scheme in **Fig.**
451 **13** (left) can result from enhanced cAMP/PKA/Ca^{2+} signaling, we may conclude that the marked
452 increases in AC8 protein level and activity and in PKA expression and activity in TG^{AC8} directly
453 or indirectly lead to the differences in LV structure and performance in TG^{AC8} vs WT (**Fig. 4 A-**
454 **F**).

455 Left ventricular structure.

456 Although the TG^{AC8} LV wall thickness was increased, neither LV mass assessed via
457 echocardiograms nor post-mortem LV weight, differed from WT (**Fig. 1**), because the thicker LV
458 walls in TG^{AC8} encompassed an LV cavity size that was markedly reduced at both end-diastole
459 and end-systole compared to WT. Thus, because left ventricular hypertrophy, is strictly defined as
460 an increase in LV mass, [17,18] the TG^{AC8} LV is not technically hypertrophied. Furthermore,
461 pathologic hypertrophy markers were not increased in TG^{AC8}. It's of interest, however, that KO
462 of, Protein Tyrosine Phosphatase Non-Receptor Type 1 (PTP1B AKA PTPN1), which protects
463 against pathologic hypertrophy and increase in fetal gene markers in response to transverse aortic
464 constriction[32] was increased by 2.5-fold in RNSEQ and 25% in proteome (**Table S.3, S.5**). The

465 lack of an increase in LV mass in TG^{AC8} may be attributable, in part, to reduced LV wall stress
466 (diastolic stretch), due to reduced filling volume, in TG^{AC8} vs WT, linked to the reduction in
467 diastolic filling time, on the bases of the increased heart rate. Of note in this regard, the left atrial
468 size was not enlarged in TG^{AC8} vs WT.

469 Histologic analysis of the thickened TG^{AC8} LV posterior wall revealed a cardiac myocyte
470 profile that was shifted to cells that were smaller in size than WT (**Fig. 2**). Thus, an increased
471 density (per unit area) of smaller cardiac myocytes contributed to the increase in LV posterior wall
472 thickness in TG^{AC8}. The LV wall collagen fraction did not differ by genotype (**Fig. S2**), even
473 though TGF β protein, TGF β receptor, and downstream signaling molecules were all upregulated
474 (**Fig. 13**). This suggests that additional adaptations that uncouple TGF β signaling from its effect
475 increase fibrosis may become activated at this age in TG^{AC8} LV.

476 **Left Ventricular Contractile Performance**

477 Neither the early, nor the late diastolic filling rates, or early/late ratio differed by genotype
478 (**Table S.1**), indicating that the smaller LV EDV in TG^{AC8} vs WT was not associated with reduced
479 diastolic functional measures. LV myocardial contractility was markedly increased in TG^{AC8} vs
480 WT as evidenced by markedly increased EF *in vivo* (**Fig. 1**), as previously reported.[10] A 30%
481 increase cardiac output in TG^{AC8} vs WT is attributable to the 30% increase in heart rate, because
482 stroke volume did not differ by genotype (**Fig. 1**).

483 As expected, expression of proteins that underly numerous cellular mechanisms driven by
484 PKA signaling that determine cardiac myocyte contractile performance, were also upregulated in
485 the transcriptome (**Table S.3**), proteome (**Table S.5**) or in both transcriptome and proteome **(Fig.**
486 **S.5**, **Table S.7**) or in WB analyses (**Fig. 4 G-J**) in TG^{AC8} vs WT. Both KCNJ2 and KCNQ1 K^+

487 channels which modulate cardiomyocyte membrane potential and action potential characteristics
488 were upregulated in TG^{AC8} vs WT (**Fig. 11**): KCNQ1 transcripts increased by 2.3-fold and protein
489 increased by 26%; KCNJ2 transcripts increased by 3.2-fold and protein 32% (**Tables S.3, S5**). Of
490 note, KCNJ2 regulation is mechanical sensitive and its increase in TG^{AC8} likely relates, at least in
491 part, to the hypercontractile state of the TG^{AC8} LV.

492 It bears emphasis that the cardiac structural and resting performance profiles of the TG^{AC8}
493 LV (**Fig. 1**), therefore differ from those, observed in LV remodeling induced by chronic exercise
494 endurance training, in which the diastolic cavity size, and stroke volume are increased at rest, [33]
495 resting HR is reduced and cardiac output is unchanged. The cardiac myocyte profile in TG^{AC8} also
496 differs from that induced in chronic exercise in which the LV myocytes size are increased but the
497 myocyte number is unchanged.[34] The marked differences in cardiac structure and function between
498 TG^{AC8} and the endurance-trained heart, in large part, likely to be attributable to increased vagal
499 tone at rest in the latter, but not in the former,[8] in which an exercise functional profile is maintained
500 around the clock at rest. In other terms the TG^{AC8} heart does not have an opportunity to rest
501 between bouts of dynamic exercise as do the hearts of endurance trained organisms.

502 Cell Cycle, Proliferation, and Growth and Developmental Circuits

503 PKA signaling links many pathways involved in protein synthesis, (**Fig. 11**) which was
504 increased in the TG^{AC8} vs WT LV (**Fig. 5A)**. Regulation of the synthesis of numerous proteins
505 related to cell cycle, cell proliferation, and growth and development were increased in TG^{AC8}
506 (**Tables S.3, S.5, S.10**). For example, the *Mras* oncogene transcript increased by 40%, and as
507 noted, RAS protein was increased by 40% in TG^{AC8} vs WT (**Fig. 5 B)**. Numerous molecules
508 downstream of RAS were increased and activated in TG^{AC8} LV including: RAF, MEK1/2 and

509 ERK1/2 **(Fig. 5 B, C**), indicating that MEK/ERK signaling, associated with enhanced cardiac
510 proliferation[35] is activated to a greater extent in TG^{AC8} compared to WT (**Fig. 13**, ERK arm).

511 AKT2 protein level and phosphorylation state were markedly increased in TG^{AC8} vs WT
512 (see WB in **Fig. S.8 A**). Numerous growth factor signaling molecules upstream of AKT were
513 upregulated in TG^{AC8} vs WT (**Fig. S.8, Fig.s. 12, 13**) including periostin, which was increased by
514 more than 100% in the transcriptome, and by 39% in proteome **(Tables S.10)** and by antibody
515 array (**Fig. S.14**). Of note, periostin plays a role in tissue regeneration, including wound healing,
516 and ventricular remodeling following myocardial infarction. [36-38] *Egfr*, *Hdgf*, and *Igf1* transcripts
517 were also increased in TG^{AC8}, and IGF1R protein was also borderline increased (**Table S.10).**
518 Interestingly, some features of endurance exercise conditioning involve upregulation of IGF
519 signaling via PIK3CA.[39] PIK3CA expression was increased in TG^{AC8} **(Fig. S.7 A)**, as well as IGF
520 signaling (**Table S.6A, B**).

521 Other molecules related to cell cycle, cell proliferation and growth and development that
522 were increased in TG^{AC8} vs WT included: CDK2 (increased by 19%), CDK6 (increased by 36%),
523 NOTCH1 (increased by 12%), beta1 catenin protein (increased by 17%), and PCNA (increased by
524 12%), *Hand2* (increased by 100%), and *Tbx5* and *Tbx20* transcripts both increased by 30% **(Table**
525 **S.10)**.

526 Nuclear EdU labeling in cardiac myocytes did not differ by genotype. EdU labeling of non-
527 cardiac myocytes, however, was substantially increased (**Fig. 3**) in TG^{AC8} vs WT. Leading
528 candidates of this regenerating cell network include endothelial cells, fibroblasts, immune cells,
529 pericytes and most importantly, telocytes.[40]

530 **Shifts in Metabolism**

531 A greater **rate** of energy production in TG^{AC8} vs WT is likely required to support, not only
532 the higher HR and increased contractility during each heartbeat compared to WT, but also
533 increased growth factor and other PI3K-directed signaling pathways, e.g. autophagy, protein
534 synthesis and protein quality control (**Fig.s. 5, 6, 13**). The increased "energy requirements" of the
535 TG^{AC8} LV are apparently being paid in full, because there is no indication that the TG^{AC8} LV is
536 chronically hypoxic, as HIF-1α transcripts are down regulated (**Table S.2**) and HIF-1α protein
537 level is reduced (**Fig. S.8 B**). Further, steady levels of ATP and phosphocreatine in the WT LV *in*
538 *vivo* at rest did not differ in TG^{AC8} vs WT (**Fig. 9**). A prior study, in fact, indicates that exercise
539 capacity of TG^{AC8} exceeds that of WT. [41]

540 Bioinformatic signals suggested that catabolism of glucose is markedly increased in TG^{AC8}
541 vs WT (**Fig. 12**). Enhancement of myocardial glucose catabolism was suggested by increases in
542 GLUT1 (AKA Slc2a1) HK1 and PFK in TG^{AC8} vs WT LV (**Fig. 11**). Of note, GLUT1 is the
543 embryonic type of glucose transporter; [42, 43] and not the canonical heart form, GLUT4 (AKA
544 Slc2a4) observed in the adult heart in response to myocardial stress.[44, 45]

545 Phosphorylation of GSK3B by AKT1 deactivates GSK3B. Inactivation of GSK3B via its
546 phosphorylation is a key conversion point of a numerous processes that confer cardioprotection.
547 [24] Although WB analysis indicated that GSK3B phosphorylation did not differ between genotypes,
548 total GSK3B protein was significantly increased in TG^{AC8} vs WT (**Fig. S.8 A**). Gys1 and
549 phosphorylase kinase (PhK) were increased in the TG^{AC8} vs WT both the transcriptome and
550 proteome (**Tables S.3 and S.5**) suggesting that a high turnover (increased synthesis and increased
551 degradation) of glycogen may be involved in the marked increase in glucose catabolism within the

552 in TG^{AC8} LV (**Fig. 12**). LV glycogen staining was modestly increased in the TG^{AC8} vs WT **(Fig.**
553 **S.13 B).**

554 Enhanced growth factor and other PI3K/AKT-driven signaling processes in TG^{AC8}
555 suggested by omics analyses and validated in **Fig. 12, 13, S.8, S.11** are tightly linked to ***aerobic***
556 ***glycolysis***.[30,46] It is well established that the **rate** at which ATP is generated in aerobic glycolysis
557 is *greater* than that generated in oxidative phosphorylation via the TCA cycle and respiration.[30]

558 Bioinformatic analyses also indicated that in addition to increased expression of the
559 glucose transporters, lactic acid dehydrogenase type A (cytosolic isoform of LDH) and the
560 glutamine transporter, which are required for ***aerobic glycolysis***[30] are also increased in TG^{AC8} vs
561 WT (**Fig.s. 12, S.9**), suggesting that, relative to WT, the TG^{AC8} heart may utilize ***aerobic glycolysis***
562 to fulfill part of its energy needs. This idea is underscored by the absence of an increase in HIF1α
563 (**Fig. S.11 B**), suggesting the absence of hypoxia in the TG^{AC8} LV.[47, 48]

564 Aerobic glycolysis promotes utilization of the pentose phosphate shunt (PPS). PPS
565 activation facilitates amino acid and nucleotide synthesis. Overexpression in TG^{AC8} LV of genes
566 and proteins that are operative within the glucose metabolic pathway, e.g. G6PDH, PGD and
567 PRPS2. (**Fig.s. 12, S.8 C**), suggests that the PPS is more highly utilized in the TG^{AC8} vs WT LV.

568 Enhanced utilization of PPS in TG^{AC8} may be involved in re-synthesis of crucial amino
569 acids and nucleotides following their degradation, (via increased autophagy, mitophagy and
570 proteosome activity in TG^{AC8} vs WT, **Fig. 6 D, G, I, J)**. PPS and may also be involved in catalyzing
571 the replenishment of NADPH in TG^{AC8} via LDH and increased G6PDH and PGD (**Fig. 12**).
572 Further ACLY, which catalyzes the **synthesis** of fatty acids (FA), leading to the formation of
573 AcCoA, linking to synthesis of FA, lipids, phospholipids, and ceramides, was increased in TG^{AC8}

574 vs WT proteome analysis (**Fig.s. 12, S.7, Table S.5**). Enhancement of these processes in TG^{AC8}
575 via increased utilization of PPS may be linked to signals pointing to increased cell cycle, cell
576 proliferation and growth and development in TG^{AC8} vs WT. In this context aerobic glycolysis and
577 increased utilization of PPS in TG^{AC8} resembles heart **embryonic** differentiation and growth prior
578 to the onset of the fetal stage when respiratory enzymes, e.g., COX7 are induced.[49] Thus, increased
579 utilization of the PPS, in TG^{AC8} may be a crucial factor that underlies increased cardiac biomass
580 (thicker LV walls vs WT containing an increased number of small myocytes, and an increased
581 number of EdU-labeled non-cardiac myocyte nuclei, **(Fig. 1 and 2)** in the absence of increased
582 collagen deposition (**Fig. S.2**)).

583 Bioinformatic signals suggested that the fatty acid β oxidation pathway and pathways that
584 degrade branched chained amino acids are concurrently reduced, possibly due to reductions in
585 CPT1, CPT2, ACAT1, HADH, HADHA, and HADHB (**Fig. 12**). Bioinformatic analyses also
586 suggested that utilization of TCA cycle and mitochondrial respiration within the TG^{AC8} LV are
587 reduced compared to WT, even though the mitochondrial number and volume do not differ by
588 genotype (**Fig. 7 G, H**).

589 Downregulation of transcripts or proteins operative within the MAS, (*Ldhb, Mpc1, Mpc2,*
590 *Mdh1, Got1, Slc25a11 Slc25a13*, and SLC25A13) **Fig. 12 and Fig. S.9** suggested that in
591 conjunction with reduced TCA cycle and mitochondrial respiration in TG^{AC8} vs WT the
592 translocation of H+ from cytosol to mitochondria to restore the level of mitochondrial NADH is
593 also reduced in TG^{AC8}. An interaction between cytosolic lactate and the MAS has been proposed:
594 cytosolic lactate formed during glycolysis may be used as a mitochondrial energy source via
595 translocation of lactate via lactate-MAS within the same cell. Lactate can also be exported from
596 one cell and taken up by other cells. [50] In heart, lactate can also regenerate cytosolic NAD^+ from

597 cytosolic LDH.[51, 52] Under conditions when shuttling of NADH from cytosol into the mitochondria
598 via the MAS is limited, an increase in cytosolic lactate concentration might be expected to favor
599 cytosolic NAD^+ regeneration via the LDH reaction. Thus, it might be expected that persistent high
600 cardiac workloads that are characteristic of TG^{AC8} heart, in conjunction with reduced MAS and
601 reduced expression of proteins involved in TCA cycle and mitochondrial respiration in TG^{AC8} vs
602 WT, are associated with increased replenishment of cytosolic NADH from NAD+, at the expense
603 of replenishment of mitochondrial NADH from NAD^+ within mitochondria. It is important to note
604 that both transcripts and protein levels of IDH, which catalyze the oxidative decarboxylation of
605 isocitrate to α-ketoglutarate, are reduced in TG^{AC8} vs WT, because during high cardiac workloads,
606 as in the TG^{AC8} heart, the α-ketoglutarate/malate transporter located within the inner mitochondrial
607 membrane does not compete favorably with mitochondrial matrix α -ketoglutarate dehydrogenase
608 for α-ketoglutarate their common substrate.[52] It is well known that even in the presence of adequate
609 oxygen during strenuous exercise requiring increased energy utilization, plasma lactate
610 concentration becomes increased, suggesting that cytosolic lactate is increased[53] in the TG^{AC8}
611 heart, favoring NAD^+ regeneration in the cytosol. [54]

612 ROS Regulation

613 Although increased rates and amounts of ATP production and utilization in the TG^{AC8} heart
614 to support simultaneous increased cardiac performance and growth factor signaling are likely to
615 be associated with a substantial increase in ROS generation, ROS levels were not increased in the
616 TG^{AC8} LV (**Fig. 8 B**). Because ATP production via aerobic glycolysis generates less ROS
617 compared respiration,[30] increased utilization of aerobic glycolysis would be one mechanism to
618 limit ROS production within the TG^{AC8} LV. Other mechanisms to reduce ROS levels that appeared
619 to be utilized to the greater extent in TG^{AC8} vs WT include NRF2 signaling, one of the top enriched

620 and activated pathways **(Fig.s. 8 A, 10 C),** SOD3 (transcripts increased by 3.2-fold and protein by
621 20%), and HMOX1 (transcripts increased by 54% and protein by 32%; **Table S.7**) which not only
622 protects tissue against oxidative stress, but also protects against apoptosis.[55, 56] HMOX1 is an
623 important activator of NRF1, which has been recently discovered to be involved in heart
624 regeneration and repair, promoted by NRF1 signaling.[57] Importantly, four members of the family
625 of glutathione peroxidases involved in the termination reaction of ROS pathways were increased
626 in TG^{AC8} vs WT: Gpx3 (transcripts by 103%, proteins by 30%); Gpx7 (transcripts by 40%, proteins
627 by 21%); Gpx8 (transcripts by 20%, proteins by 16%); Gpx1 (transcripts by 39%, proteins by
628 12%). Several members of glutathione transferases were differentially expressed in TG^{AC8} vs WT:
629 Gsta3 (transcripts and proteins upregulated by 55% and 26% respectively); GSTM5 (proteins
630 upregulated by 23%), GSTM1 (proteins upregulated by 14%); mitochondrial glutathione reductase
631 GSR was also upregulated, while GSTM7 (transcripts and proteins were decreased by 21%, and
632 9%) and GSTO1 (protein was decreased by 9%).

633 ## Cardiac Protection Circuitry

634 ### Negative feedback on βAR-cAMP-PKA-Ca signaling

635 Numerous molecules that **inhibit** βAR signaling, (e.g. Grk5 by 2.6 fold in RNASEQ and
636 30% in proteome; Dab2 by 1.14 fold in RNASEQ and 18% in proteome; and β-arrestin by 1.2 fold
637 in RNASEQ and 14% in proteome) were upregulated in the TG^{AC8} vs WT LV (**Table S.3, S.5** and
638 **S.9)**, suggesting that βAR signaling is downregulated in TG^{AC8} vs WT, and prior studies indicate
639 that βAR stimulation-induced contractile and HR responses are blunted in TG^{AC8} vs WT.[8,11] The
640 heart, itself, produces catecholamines, (**Fig. S.3 A**). It is interesting to note that βARs become
641 desensitized in TG^{AC8} (**Fig. S.3 B**), even though neither plasma norepinephrine, nor epinephrine
642 are increased, but reduced in TG^{AC8} vs WT[8] (**Fig. S.3 C**).

643 Both the RNASEQ and proteome analyses indicated that PI3K/AKT signaling, which
644 promotes survival,[58] is activated in TG^{AC8} vs WT (**Fig. 11** and **13**). Numerous studies have
645 indicated that PI3K signaling is involved in βAR internalization,[59,60] and is also involved in cAMP
646 metabolism by acting as an essential component of a complex controlling PDE3B
647 phosphodiesterase-mediated cAMP destruction.[61,62]

648 In cultured cardiomyocytes, βAR stimulation increases PI3K activity.[63, 64] Both the β1AR
649 and β2AR have been reported to transactivate PI3K in vitro.[65, 66] Moreover, βAR stimulation-
650 induced increases in heart weight, contractile abnormalities, and myocardial fibrosis, and cardiac
651 "fetal" genes were markedly attenuated in the absence of PI3K expression.[67] Although this
652 formidable evidence in most cases has identified PI3Kγ to be specifically involved in
653 cardioprotection with response to G-protein coupled receptor signaling, PI3Kγ was not identified
654 in our transcriptome or proteome analyses, but RT-qPCR assay detected significant increase of
655 catalytic subunit of PI3Kγ (*Pi3kcg)* expression (**Table S.9**). Tyrosine receptor coupled PI3KCA,
656 AKT and PDK1 were increased in TG^{AC8} vs WT proteome, and these proteins, as well as PTEN
657 (WB) and PIP3 (ELISA) were increased TG^{AC8} vs WT (**Fig. 12, Fig. S.7**).

658 A blunted response to βAR stimulation in a prior report was linked to a smaller increase in
659 L-type Ca^{2+} channel current in response to βAR stimulation in the context of increased PDE
660 activity.[13, 14] WB analyses showed that PDE3A and PDE4A expression increased by 94% and 36%,
661 respectively in TG^{AC8} vs WT, whereas PDE4B and PDE4D did not differ statistically by genotype
662 (**Fig. S.11 A**). In addition to mechanisms that limit cAMP signaling, the expression of endogenous
663 PKI-inhibitor protein (PKIA), which limits signaling of downstream of PKA was increased by
664 93% ($p<0.001$) in TG^{AC8} vs WT (**Table S.3**). Protein phosphatase 1 (PP1) was increased by 50%
665 (**Fig. S.11 A**). The Dopamine-DARPP-32 feedback on cAMP signaling pathway was enriched and

666 also activated in TG^{AC8} vs WT (**Fig. 12**), the LV and plasma levels of dopamine were increased,
667 and DARPP-32 protein was increased in WB by 269% (**Fig. S.11 A**).

668 Thus, mechanisms that limit signaling downstream of AC-PKA signaling (βAR
669 desensitization, increased PDEs, PKI inhibitor protein, and phosphoprotein phosphatases, and
670 increased DARPP-32, cAMP (dopamine- and cAMP-regulated phosphoprotein)) are crucial
671 components of the cardio-protection circuit that emerge in response to chronic and marked
672 increases in AC and PKA activities (**Fig. 4 C, F**).

673 **Upregulation of stress response pathways.**

674 Beyond the adaptations to limit the degree to which cAMP/PKA signaling is activated,
675 numerous canonical stress-response signaling circuits were concurrently enriched in TG^{AC8} (**Fig.**
676 **13**). Multiple parallel cascades of stress response receptor signaling within circuits downstream of
677 AC signaling (**Fig. 13)**, include: RTKs (PI3K/AKT, ERK-MAPK); cytokine receptors (JNK1/2,
678 JAK2/STAT3), pattern recognition receptor RAGE (S100/calgranulins) and T-cell receptor (NF-
679 κB) (**Fig. 13**). The main functional category of genotypic changes identified in PROTEOMAP
680 analysis, **Environmental Information Processing** (**Fig. S.7**), points to an integration of these
681 stress response pathways. The consilience of cardio-protective adaptations that result from
682 integrated activation of signaling cascades that were enriched in TG^{AC8} included: cell survival
683 initiation, protection from apoptosis, proliferation, prevention of cardiac-myocyte hypertrophy,
684 increased protein synthesis and quality control, increased inflammatory and immune responses,
685 facilitation of tissue damage repair and regeneration and increased aerobic energetics (**Fig. 13**).

686 Pathways downstream of receptor tyrosine kinase (RTK), a classical cognate receptor,
687 amongst others, transmits signals to promote the activation of PI3 kinase and RAS-RAF-MEK1/2-

688 ERK1/2 (**Fig. 13**). Receptor activation by adrenergic agonists and growth factors (such as
689 periostin, increased by 39% in omics and validated by antibody array (**Table S.5, Fig. S.14**) bind
690 to β-AR and RTK, respectively. Ras-p21 functions as a molecular link for membrane GPCR and
691 RTK to transduce signals from these receptors to downstream signaling machinery (**Fig. 13**, ERK
692 arm). Ras-Raf-MEK-ERK pathway plays a key role in cardioprotection in the context of ischemia-
693 reperfusion injury and oxidative stress.[68] Downstream of Ras-p21, c-Raf is subsequently induced,
694 which, in turn, sequentially activates MEK1/2 and ERK1/2 to achieve their downstream effects
695 (**Fig. 13**, ERK arm, **Fig. 4 B, C**). MEK/ERK1/2 activation promotes tissue repair that is essential
696 for repair of damaged cells or cell regeneration (see below) in response to cardiac stress in vivo
697 (**Fig. 13**, ERK arm), especially those observed in genetically engineered animal models.[69]

698 Ras-p21 signaling also exerts protective influences on cell reparative and regenerative
699 capacity, presumably via activation of ERK-independent downstream pathways of PI3K/AKT
700 signaling[70, 35]. Increased expression of the catalytic subunit PIK3CA in TG^{AC8} by 15 % in WB
701 (**Fig. S.8 A**) may be linked to the activation of the downstream targets, including PDK1
702 phosphorylation on serine 241, subsequent phosphorylation of AKT2 (i.e., threonine 308 and
703 serine 473) and of the transcription factor, Foxo1, at serine 256 (**Fig. S.11 B, Fig. 13**, PI3K arm,
704 bottom panel). Activation of AKT inhibits hypertrophic signaling in adult hearts in vivo, [71 72 73 18]
705 while inducing protein synthesis and activating protein quality control signaling [74] (**Fig. 13**, PI3K
706 arm). This anti-hypertrophic effect of AKT in TG^{AC8} may be linked to the lack of increased
707 myocyte size and absence of increased LV mass in TG^{AC8} (**Fig.s. 1J, 2B, C, D**), (see below), even
708 in the presence of elevated α-skeletal-actin and MYH6 (**Fig. 4 G, Fig. 13,** bottom panel).

709 The tumor suppressor PTEN is a lipid phosphatase that regulates cell growth, survival and
710 migration by catalyzing the dephosphorylation of the phospholipid phosphatidylinositol (3,4,5)-

711 trisphosphate PtdIns (3,4,5)P3 or PIP3, an integral second messenger molecule for the PI3K-AKT
712 signaling, thus antagonizing this pathway. PTEN protein abundance was increased by
713 approximately 28% ($p<0.01$) in the TG^{AC8} LV compared to WT by WB (**Fig. S.8 E**), in
714 concordance with proteomics data, which showed a 22% increase in PTEN ($p=0.053$) in the TG^{AC8}
715 LV. Phosphorylation of sites within the PTEN C-terminal domain, including S380, T382 and
716 T383, have been demonstrated to be involved in the regulation of stability and activity, with a loss
717 in phosphorylation leading to membrane recruitment and greater activity followed by rapid
718 proteosome-mediated degradation.[75,76,77] Phosphorylation of Ser380 residues was significantly
719 lower in TG^{AC8} vs WT (-35%, $p<0.05$) as was the ratio of p-PTEN Ser380/Total PTEN (-50.15%,
720 $p<0.005$) (**Fig. S.8**), suggesting that PTEN activity is increased in the TG^{AC8} vs WT. A 2-fold
721 higher expression of PIP3 in TG^{AC8} vs WT, determined by ELISA, along with increases in PI3K
722 catalytic subunit abundance and AKT activity, strongly suggest that PTEN does not exert **a net**
723 negative regulatory effect in TG^{AC8} on this pathway. Rather, an increase in PTEN in TG^{AC8} may
724 be necessary to maintain the available pool of PIP2 that is required for phospholipid metabolism,
725 and other signaling pathways, such as e.g. PLC/IP3/DAG signaling (important in Ca^{2+} regulation),
726 or in functional processes like e.g. Endocytosis and Actin cytoskeleton remodeling,[78] that are
727 enriched and activated in TG^{AC8} vs WT (**Fig. 10 C and Table S.6 A,B**).

728 Integral components of the PI3K-AKT and RAS-RAF-MEK1/2-ERK1/2 survival-
729 associated pathways converge to suppress apoptosis[79,80,81] (**Fig. 13**, PI3K and ERK arms).
730 Caspase-3 levels were increased (**Fig. S.11 B**). The barely detectable or low protein expression of
731 hallmarks of apoptosis in TG^{AC8} LV, including *cleaved* caspase-3 and its downstream *cleaved*
732 PARPs, suggest that apoptosis suppression signaling mechanisms become activated in the TG^{AC8}
733 LV (**Fig. S.11 B and Fig. 13**, PI3K and ERK arms top and bottom panels). That full-length

caspase-3 expression was increased in TG^{AC8} vs WT, but not cleaved (**Fig. S.11 B and Fig. 12**),[82] provides strong evidence of activation anti-apoptotic functions of caspase-3 activation in the TG^{AC8} LV. Further, there was no indication of increased apoptotic nuclei in TG^{AC8} LV tissue (**Fig. S.13 A**).

Proteostasis

Many upregulated transcripts and proteins in TG^{AC8} vs WT (**Fig. S.7, Tables S3, S.5**), including the serine/threonine-protein kinases, MSK1 and MNK1, might signal within cardio-protective pathways (**Fig.s. 5 F, G; 13**). Specifically, MSK1 is involved in regulation of the transcription factors CREB1, ATF1, RELA and STAT3. MNK1 is involved in the initiation of protein translation by interacting with eIF4G and phosphorylating eIF4E.

The Small Proline Rich Protein 1 **Sprr1a,** which is linked to induction of protein synthesis (**Fig. 13**, bottom panel), was the most abundantly overexpressed transcript **and** protein in the TG^{AC8} **LV (Table S.7 A).** Immunolabeling of Sprr1a in single LV myocytes isolated from TG^{AC8} is illustrated in **Fig. S.15**. Sprr1a is associated with inflammation, cellular stress, and repair[83,84] and has been linked to protection against cardiomyocyte death in the setting of ischemia–reperfusion injury.[85,86] Sprr1a stimulates the expression of Rtn4 (**Fig. S.15**), a member of the reticulon encoding gene family associated with endoplasmic reticulum that is involved in neuroendocrine secretion or in membrane trafficking in neuroendocrine cells.[87, 88] Rtn4, which was also overexpressed in TG^{AC8} vs WT (transcripts increased by 50% and proteins increased by 30%, **Fig.** S.**15**, **Table S.7 A)**.

Derlin1, a protein that was also markedly overexpressed in TG^{AC8} vs WT (by 132%, **Table S.5**) participates in the ER associated protein degradation by recognizing and selecting misfolded

756 or unfolded proteins and translocating these from the ER lumen to the cytosol for proteasomal
757 degradation. Calnexin, and calreticulin both members of the CALR/CN cycle, which ensures the
758 quality and folding of newly synthesized molecules within the endoplasmic reticulum, were also
759 both increased by WB in TG^{AC8} (**Fig. S.11 D**). Numerous other molecules involved in unfolded
760 protein response signaling significantly differed by genotype in omics analyses: transcripts
761 included ATF4, ATF6, Caspase 3, CALR, HSP90 (**Table S.3**); proteins included: CASP3, CASP6,
762 HSP90α (**Table S.5**).

763 **Autophagy**

764 Forced changes in energy metabolism, downstream of markedly increased levels of
765 AC/cAMP/PKA signaling in TG^{AC8}, and resultant adaptations to this stress (**Fig. 13)**, may produce
766 excess wear-and-tear damage in cellular components, requiring an adaptively higher
767 autophagy/mitophagy machinery. The preserved level of mitochondrial fitness (**Fig. 6 I, J; Fig. 7**
768 **M, N**) in TG^{AC8}, in the context of marked chronic AC-driven cellular stress, likely reflects one
769 such autophagic adaptation. Protein levels of ATG13, ATG4B and PARKIN, members of the
770 autophagy machinery were upregulated in TG^{AC8} vs WT (**Fig. 6 E-G**). Specifically, the cysteine
771 protease ATG4B processes pro-MAP1LC3 and pro-GABARAP in the early stages of autophagy
772 and endocytosis pathways, before their lipidation (addition of the phosphatidylethanolamine) by
773 ATG7 and ATG3. Being also involved in MAP1LC3/GABARAP delipidation, it plays a key role
774 in their turnover. The autophagy-related protein ATG13 is a factor required for autophagosome
775 formation and part of the initiation complex with ULK1 and RB1CC1. It is also involved in
776 mitophagy, together with the E3 ubiquitin-protein ligase PARKIN, which acts downstream of
777 PINK1. Upregulation of these proteins protects against mitochondrial dysfunction during cellular

778 stress by coordinating mitochondrial quality control mechanisms that remove and replace
779 dysfunctional mitochondrial components.

780 Inflammation/Immune Signaling.

781 The myocardium is intimately connected with the immune system and activation of the
782 immune system has been shown to have both protective and maladaptive effects on the heart. [89]
783 This inherent duality of the immune system has spurred a quest for tools to harvest the protective
784 effect of the innate and adaptive immune response without experiencing their detrimental effects.
785 [90] On this background, it is remarkable that the most upregulated pathway in the TG^{AC8} hearts was
786 "leukocyte extravasation signaling" (**Fig. 10 C**) and that the TG^{AC8} was characterized by up
787 regulation of several inflammatory molecules and pathways, both in the "omics analysis" and in
788 western blot based or RT-qPCR based validation analyses. TG^{AC8} hearts in fact showed
789 upregulation of *IL-6*, *IL-10*, ICAM1, and CCL12 (**validated in Fig. S.12 A**). Furthermore, they
790 showed upregulation of MAGUK and MALT1 of the CBM complex together with its downstream
791 NF-κB signaling (NF-κB coactivators TRAF2/6 and ATF3 (**Fig. 13,** NF-κB arm, **Fig. S.7**, **Table**
792 **S3, S.5 and Fig. S.12 A**)). The TG^{AC8} heart was also characterized by phosphorylation of JNK1/2
793 on threonine 183 and tyrosine 185 (**Fig. 13**, JNK arm, and **Fig. S.8**) that paralleled gene expression
794 changes consistent with activation of the JNK1/2 signaling pathway in TG^{AC8} vs WT (**Tables S.3,**
795 **S.5, S.6 B**).

796 The fact that we detected upregulation of T cell receptor signaling and B cell receptor
797 signaling (**Table S.6 A, B**) together with the fact that we detected upregulation of the CBM
798 complex (central in B and T cell activation) suggests that the AC8 heart might be characterized by
799 recruitment of T and B cells to the myocardium. [91] Specific subclasses of lymphocytes have been
800 shown to have protective effect on the heart. [89] JNK1/2 activation is centrally involved in

801 inflammatory signaling[92] but also linked to inhibition of cardiac hypertrophy[93] and promotion of
802 reparative and regenerative capacities. [94] Taken together, these observations raise the intriguing
803 possibility that the AC8 overexpressing heart might manage to cope with continuous stress also
804 through the activation of a cardio-protective immune responses.

805 TG^{AC8} LV protection circuits resemble some adaptive mechanisms that 806 accompany disease states.

807 We next performed IPA analyses in order to ascertain the extent to which cardiac protection
808 circuits identified in the TG^{AC8} LV (**Fig. 13**) might be utilized as adaptations to the stress of various
809 disease states. The top disease categories identified in both the TG^{AC8} transcriptome and proteome
810 were **Organismal Injury and Abnormalities and Cancer (Fig. S.16),** the latter being subsumed
811 within the former category. This is not surprising, because the sequalae of marked chronically
812 increased AC/cAMP/PKA signaling illustrated in TG^{AC8} LV protection circuitry **(Fig. 13),** are
813 very similar to the "**Hallmarks of Cancer**",[15, 16] and included: protection from apoptosis, survival,
814 aerobic glycolysis, increased proliferation, enhanced protein synthesis and quality control,
815 increased inflammatory and immune response, enhanced tissue damage repair and regeneration.
816 Thus, the TG^{AC8} LV utilizes a consilient pattern of adaptive mechanisms that emerge in many
817 cancer cell types for self-protection.[15,16] This protection circuitry allows the adult TG^{AC8} heart to
818 cope (for at least up to a year),[10] with numerous, marked cell-tissue stressors driven by the
819 markedly augmented AC-cAMP-PKA-Ca^{2+} signaling. "Limited versions" of this cardio-protective
820 profile that emerges within TG^{AC8} LV have also been previously discovered to be central to cardiac
821 ischemic pre-conditioning[95] and exercise endurance cardiac conditioning.[1,96]

822 **Opportunities for Future Scientific Inquiry Afforded by the Present Results**

823 By design our systems approach to elucidate some general foundations of the consilient
824 adaptation profile that protects the chronically high performing TG^{AC8} heart, represents only a
825 "first port of call", defining some general features of the TG^{AC8} cardiac performance/protection
826 profile. Because many of the perspectives depicted in the scheme in **Fig. 13** were derived from
827 bioinformatic analyses of cell lysates, it is not implied that all of these circuits are present or
828 become activated in all cell types that reside in the LV myocardium. It is apparent, however, from
829 our results, consilient shifts in enrichment or activation of numerous stress response pathways
830 accrue to allow for the chronic high-level performance of the TG^{AC8} LV. Similarly, a consilience
831 of shifts in numerous stress response pathways may be of biological significance in pathologic
832 states, for example, e.g. consilient adaptations may be allowed for proper healing in disease state,
833 e.g. myocardial infarction or chronic heart failure.

834 A most important aspect of our results, is that they identify numerous hypotheses that can
835 be tested in future, more in depth studies aimed at: (1) defining the precise cardiac cell types in
836 which protection circuitry is activated in the chronically over-worked TG^{AC8} heart; (2) providing
837 deeper definitions of the multitude of signaling pathways that differed significantly in enrichment
838 and activation status among cell types in TG^{AC8} vs WT (**Fig.s. 10-13, Table S.6 A, B**). This will
839 lead to identification of novel associations among the concurrently activated adaptive mechanisms
840 within and among cell types in TG^{AC8} LV that are not intuitively linked to cardiac protection in
841 the context of our current state of knowledge. For example, elucidation of specific details within
842 the leukocyte extravasation pathway, the top activated IPA canonical pathway in TG^{AC8}, and of
843 other highly activated canonical signaling pathways in TG^{AC8} vs WT (**Fig. 10 C** and **Table S.6 A,**
844 **B)**, that are not usually addressed in the field of cardiac research. This will permit detection of

845 crosstalk between cardiac myocytes and other cell types such as immune cells and others that is
846 likely to be critical to the cardiac protective and performance-enhancing circuitry that is harbored
847 within TG^{AC8} heart (**Fig. 13**). (3) Identification post-translational protein modifications e.g. via
848 delineations of changes in the TG^{AC8} LV phosphoproteome, ubiquitome, acetylome, and 14-3-3
849 interactome; (4) identifying specific types of intersticial cells that proliferate within the LV
850 myocardium that was predicted by our omics results, and validated by EdU and BrdU labeling of
851 the young adult TG^{AC8} heart between 2 and 3 mo (**Fig. 3**). (5) precisely defining shifts in
852 metabolism within the cell types that comprise the TG^{AC8} LV myocardium via metabolomic
853 analyses, including fluxomics.[97] It will be also important that future metabolomics studies
854 elucidate post-translational modifications (e.g. phosphorylation, acetylation, ubiquitination and
855 14-3-3 binding) of specific metabolic enzymes of the TG^{AC8} LV, and how these modifications
856 affect their enzymatic activity.

857 Finally, chronic consilient utilization of numerous adaptive pathways, however, may
858 present a double-edged sword, compensating for chronic stress in the "short run", but becoming
859 maladaptive when utilized over prolonged periods of time. In fact, TG^{AC8} mice have a reduced
860 (about 30%),[10] a median life span, and later in life (at about 12 mo) marked LV fibrosis and dilated
861 cardiomyopathy occur. Future studies are required to precisely discover how the consilience of
862 cardio-protective adaptations harbored within the TG^{AC8} heart at 3 mo of age that were defined in
863 present study fails over a protracted time-course are extremely important. It is noteworthy in this
864 regard, when our omics data were specifically filtered for "**cardiovascular system"** and
865 "**cardiovascular disease"** in bioinformatic analyses, features common to variety of
866 cardiomyopathies were predicted in the "super-performing" TG^{AC8} LV (**Table S.11 A, B**). The
867 basis of this prediction may stem from the fact that omics "knowledge" generated by findings in

prior cross-sectional studies of experimental heart failure, it seems to us may have often been misinterpreted to be **causal** factors of the heart failure, rather than adaptations that react to ameliorate the heart failure, due to a lack of longitudinal prospective. Thus studies, conducted *longitudinally* over the TG^{AC8} life course, to generate testable hypothesis about which of these correlated findings are *cause-and-effect* vs those that are simply *associated* are required to dissect out which factors that enable the "super performing heart" of the TG^{AC8} during young adulthood, gradually fail over a prolonged period of time, resulting not only in accelerated aging, but also in and frank, severe, dilated cardiomyopathy.[10]

Acknowledgments

We thank the NIDA Confocal and Electron Microscopy Core for access to their equipment, and specifically Zhang Shiliang (Core manager) and Marisela Morales (Director). We wish to thank Loretta Lakatta for her superb editorial assistance.

Funding

This research was supported by the Intramural Research Program of the NIH, National Institute on Aging (USA).

883 # Fig. Legends

884 **Fig. 1. (A-K), Echocardiographic parameters (N= 28 for TG^{AC8}; WT=21); L**
885 **heart weight/body weight at sacrifice (N=75 for TG^{AC8} and N=85 for WT). See**
886 **Table S.1 for additional Echo parameters.**

887 **Fig. 2. (A) WB of Pathologic hypertrophy markers, *(B, C)* cardiac myocyte size**
888 **and distributions of cardiac myocytes, (*D) Representative LV sections depicting***
889 ***cardiac myocyte diameters,***

890 **Fig. 3 (A-G) representative examples of confocal images (400x) of LV WGA**
891 **(red), vimentin (Cyan), EdU (yellow), DAPI (blue), (H) average number of EdU**
892 **labeled nuclei positive field counts in LV TG^{AC8} vs WT (N=3 mice in each**
893 **genotype). Detection of cardiomyocyte S-phase activity. (I) Section from the**
894 **heart of a TG^{AC8}, MHC-nLAC double-transgenic mouse subjected to 12 days of**
895 **BrdU treatment. The section was processed for β-galactosidase (to identify**
896 **cardiomyocyte nuclei, red signal) and BrdU (to identify DNA synthesis, green**
897 **signal) immune reactivity, and then counterstained with Hoechst (which stains**
898 **all nuclei, blue signal). (J) Example of an S-phase cardiomyocyte nucleus**
899 **detected with this assay. The upper panel shows β-galactosidase immune**
900 **reactivity (red channel), the middle panel shows BrdU immune reactivity**
901 **(green channel), and the lower panel shows a red and green color combined**
902 **image of the same field. The arrow identifies an S-phase cardiomyocyte nucleus,**
903 **as evidenced by the overlay of β-galactosidase and BrdU immune reactivity,**
904 **which appears yellow in the color combined image. (H) Graph representing S-**
905 **phase activity in the TG^{AC8}, MHC-nLAC double-transgenic vs. the MHC-**
906 **nLAC single transgenic animals (mean +/- SEM, p=0.315; 5 mice per genotype**
907 **and 3 sections per mouse were analyzed).**

908 **Fig. 4. (A)** Representative examples of ADCY8 immunolabeling in TG^{AC8} and WT
909 LV cardiomyocytes, **(B)** Average AC8 fluorescence in LV cardiomyocytes and **(C)**
910 Average AC activity in TG^{AC8} vs WT, **(D, E)** Expression levels of PKA catalytic
911 and regulatory subunits, and **(F)** PKA activity in TG^{AC8} vs WT, **(G-M)** Western Blot
912 analysis of selected proteins involved in excitation - Ca release – contraction-
913 relaxation coupling TG^{AC8} vs WT LV. **(L)** RyR2 immunolabeling. Antibodies
914 employed are listed in supplemental methods. (N=199 WT cells and 195 TG^{AC8} cells
915 (each from 3 mice)**.**

916 **Fig. 5. (A)** Rate of global protein synthesis and **(B-G)** mechanisms downstream of
917 PKA signaling involved in protein synthesis in the TG^{AC8} and WT**.**

918 **Fig. 6. (A)** Proteosome activity assay and **(B, C)** accumulated proteins in soluble
919 and insoluble fractions of LV lysates in TG^{AC8} vs WT. **(D)** WB of HSP90 in TG^{AC8}
920 and WT, **(E-H)** Expression levels of selected proteins involved in the autophagy
921 process. **(I, J)** Autophagolysosome accumulation is enhanced in AC8 mice. The
922 statistical significance is indicated by **($p<0.01$) and t ($p<0.01$ in one-tailed t test).

923 **Fig. 7. (A, B)** Representative panoramic electron micrographs and **(C-F)** higher
924 resolution images of LV cardiac muscle fibers and mitochondria in TG^{AC8} and WT.
925 White arrowheads depict lipid droplets; asterisks show swollen, disrupted
926 mitochondria with lighter cristae compared to the surrounding, healthy
927 mitochondria. **(G, H)** Average mitochondrial number of quantitative stereological
928 analyses of normal mitochondrial number and volume, **(I, J)** damaged mitochondria**,**
929 **(K, L)** number of lipid droplets per cell area and volume of lipid droplets. **(M, N)**
930 mPTP-ROS threshold, measured in a single LV cardiac myocyte, did not differ
931 between TG^{AC8} and WT mice. Insulin was employed as a positive control. (N=3 in
932 each genotype) (** $p<0.01$, *** $p <0.001$)**.**

933 **Fig. 8 (A) WB analysis of Nrf2 expression in LV TGA^{C8} vs WT. (B) LV**
934 **performance and the rate of superoxide (ROS) generation in isolated working**
935 **TG^{AC8} and WT hearts.**

936 **Fig. 9 (A) A schematic of ATP creatine energy system, (B) Representative $_{P}$31**
937 **NMR spectra of TGAC8 and WT hearts. (C-E) average levels of ATP, PCr, and**
938 **ATP/PCr in TGAC8 and WT hearts derived from NMR spectra.**

939 **Fig. 10 (A) Schematic of the total number of transcripts (subset "a" – 11,810),**
940 **and proteins (subset "b" 6,834), identified in LV lysates, the number of**
941 **transcripts (subset "d" 2,323), and proteins (subset "d" 2,184), that differed by**
942 **genotype, and number of identified transcripts and proteins that both differed**
943 **by genotype (subset "e" - 544). (B) WEBGESTALT analysis of the XX**
944 **transcripts (Panel A subset "c") and YY proteins (Panel A subset "d") that**
945 **significantly differed by genotype. Biological Processes (BP), Cell**
946 **Compartment (CC), Molecular Functions (MF). (C) Top canonical signaling**
947 **pathways differing in enrichment (-log(pvalue) >1.3) and activation status by**
948 **genotype (Z-score: Fig. key) in IPA analysis of transcripts and proteins.**

949

950 **Fig. 11 Regulatory Networks Centered on Adenylyl Cyclase and Protein Kinase**
951 **A Signaling.**

952 Gene families of proteins regulated by PKA ranged from transcription regulators, kinases,
953 peptidases and other enzymes, transmembrane receptors, ion channels and other gene families.
954 Canonical signaling pathways in which these proteins operate and downstream biological and
955 molecular processes of proteins in these pathways are also displayed (lower part). See **Table S.8**
956 for the full list of these downstream effects of PKA signaling.

957

958 **Fig. 12 Growth and Metabolism.**

959 A schematic of growth and metabolism circuitry based on signals derived from bioinformatic
960 analyses of the transcriptome and proteome and on selected WBs. Catabolism of glucose is

961 markedly increased in TG^{AC8} vs WT as reflected in increased expression of Glut1, HK1 and PFK
962 and other glycolytic enzymes, whilst fatty acid β oxidation pathway is concurrently reduced, as
963 reflected in reduced expression of Cpt1, Cpt2, Acat1, Hadh, Hadha, and Hadhb. in TG^{AC8} vs WT
964 LV. Shifts in the transcription of genes and translation of proteins that are operative within PPS
965 pathway, i.e. G6PDH, PGD and PRPS2 suggests that PPS is more highly activated in the TG^{AC8}
966 vs WT. The combination of increased expression of the glucose transporter, lactic acid
967 dehydrogenase type A and the glutamine transporter in TG^{AC8}, suggests that, relative to WT, the
968 TG^{AC8} heart utilizes aerobic glycolysis to fulfill part of its energy needs. Enhanced growth factor
969 and other PI3/AKT driven signaling processes increased in TG^{AC8} vs WT are also known to be
970 linked to aerobic glycolysis.

971

972 **Fig. 13. Schematic of TG^{AC8} Heart Performance and Protection Circuits that**
973 **appeared to be concurrently engaged in the TG^{AC8} LV.**

974 The pathways/specific targets and the effector functions/outcomes culminating from the regulation of the
975 components within the circuits in the pathways are represented according to published literature with
976 respect to cardiac-specific context (See Discussion). **Pink colors** represent proteins that differed by
977 genotype in WB. Molecular targets or components in **red**, **green,** and **grey** represent molecular targets or
978 components that are increased or upregulated, decreased or downregulated, or unchanged, respectively, in
979 TG^{AC8} vs WT.

980 # Supplements

981 ## Supplemental Tables

982 **Table S.1. List of Echo parameters recorded in TG^{AC8} heart vs WT.**

983 **Table S.2. A Listing of all 11810 identified transcripts.**

984 **Table S.3. A listing of 2323 transcripts that significantly differed in expression by**
985 **genotype.**

986 **Table S.4. A listing of all 6834 identified proteins.**

987 **Table S.5 A listing of 2184 proteins that significantly differed in expression by**
988 **genotype.**

989 **Table S.6. A listing of canonical pathways in IPA analysis of the total number of (A)**
990 **transcripts and (B) proteins that were differentially enriched or activated in TG^{AC8}**
991 **vs WT. (C) A listing of molecules with indication of involvement in number of**
992 **pathways.**

993 **Table S.7. (A) A listing of 544 molecules of which both transcripts and proteins**
994 **differed by genotype. (B) A listing of canonical pathways that were differentially**
995 **enriched by genotype in IPA analysis of 544 transcripts and proteins.**

996 **Table S.8. A Complete list of downstream effects of enriched canonical signaling**
997 **pathways in TG^{AC8}, depicted on Fig. 11.**

998 **Table S.9. RT-qPCR analysis of selected transcripts related to G-protein Coupled**
999 **Receptor Signaling, that differed by genotype in RNASEQ.**

1000 **Table S.10 Transcripts and proteins involved in Cell Cycle/Cell Proliferation, and**
1001 **Growth and Developmental Circuits that differed between TG^{AC8} vs WT.**

1002 **Table S.11 IPA representation of top cardiovascular disease-related functions within**
1003 **the LV (A) transcriptome and (B) proteome of TG^{AC8} and WT.**

1004 **Table S.12 Primers used in RT-qPCR analyses**

1005 **Table S.13 Antibodies used in WB analyses and antibody arrays**

1006

1007 ## Supplemental Fig.s

1008 **Fig. S.1 Representative images of echocardiograms.**

1009 **Fig. S.2 Representative LV sections, and average collagen density.**

1010 **Fig. S.3 Pathway for catecholamine synthesis and breakdown, myocardial and**
1011 **plasma catecholamine levels.**

1012 **Fig. S.4 Volcano plots and heat maps of transcripts and proteins.**

1013 **Fig. S.5. Spearman's correlations of Z-scores of IPA transcriptome and**
1014 **proteome canonical pathways that significantly differed by genotype.**

1015 **Fig. S6. Correlation plot of 544 identified molecules of which *both* transcripts**
1016 **and proteins differed by genotype.**

1017 **Fig. S.7. PROTEOMAP.**

1018 **Fig. S.8 WB analyses of Selected Proteins that mediate PIP3 Kinase Signaling**
1019 **and Metabolism.**

1020 **Fig. S.9 Detailed schematic malate-aspartate shuttle based on signals derived**
1021 **from bioinformatic analyses of the transcriptome and proteome and on selected**
1022 **WBs.**

1023 **Fig. S.10 Representative examples of (A) ACACB immunolabeling of TG^{AC8}**
1024 **and WT LV myocytes; (B) average ACACB fluorescence in LV cardiomyocytes**
1025 **(n=25 for each group); (C) Relative Quantification of Acaca mRNA expression**
1026 **in LV tissue (n=4 for each group).**

1027 **Fig. S.11 WB Analyses of Selected Proteins Within the Performance and**
1028 **Protection Circuitry Depicted in Fig. 13. (A) Negative feedback adaptations on**
1029 **AC/PKA signaling, (B) WB analysis of selected proteins involved in**
1030 **Jak/Stat/Jnk/Caspase signaling. (C) WB analysis of selected proteins involved**
1031 **in angiotensin receptor signaling. (D) WB analysis of Calnexin and Calreticulin,**
1032 **proteins involved in ER protein processing.**

1033 **Fig. S.12 RT-qPCR analysis of genes regulating cytokines level in the LV genes**
1034 **and Cytokines levels measured from heart tissue lysates.**

1035 **Fig. S.13 LV Tissue Staining for apoptosis and Glycogen.**

1036 **Fig. S.14 Periostin levels detected in TG^{AC8} vs WT LV (Growth Factor**
1037 **Quantibody Array)**

1038 **Fig. S.15 Sprr1 signaling network, Immunolabeling of Sprr1a in isolated LV**
1039 **myocytes, and WB analysis of RTN4 expression.**

1040 **Fig. S.16. IPA representation of top Disease-related functions within the LV**
1041 **transcriptome and proteome of TG^{AC8} and WT.**

1042

1043

1044

1045 # References

1046 1. Vega RB, Konhilas JP, Kelly DP and Leinwand LA. Molecular Mechanisms Underlying Cardiac
1047 Adaptation to Exercise. *Cell Metab*. 2017;25:1012-1026.
1048 2. Ventura-Clapier R, Mettauer B and Bigard X. Beneficial effects of endurance training on cardiac
1049 and skeletal muscle energy metabolism in heart failure. *Cardiovasc Res*. 2007;73:10-8.
1050 3. Lovallo WR. Cardiovascular reactivity: mechanisms and pathways to cardiovascular disease. *Int J*
1051 *Psychophysiol*. 2005;58:119-32.
1052 4. Zhang X, Szeto C, Gao E, Tang M, Jin J, Fu Q, Makarewich C, Ai X, Li Y, Tang A, Wang J, Gao H,
1053 Wang F, Ge XJ, Kunapuli SP, Zhou L, Zeng C, Xiang KY and Chen X. Cardiotoxic and cardioprotective
1054 features of chronic beta-adrenergic signaling. *Circ Res*. 2013;112:498-509.
1055 5. Antos CL, Frey N, Marx SO, Reiken S, Gaburjakova M, Richardson JA, Marks AR and Olson EN.
1056 Dilated cardiomyopathy and sudden death resulting from constitutive activation of protein kinase a. *Circ*
1057 *Res*. 2001;89:997-1004.
1058 6. Squire IB and Barnett DB. The rational use of beta-adrenoceptor blockers in the treatment of
1059 heart failure. The changing face of an old therapy. *Br J Clin Pharmacol*. 2000;49:1-9.
1060 7. Werner CM and Bohm M. The therapeutic role of RAS blockade in chronic heart failure. *Ther Adv*
1061 *Cardiovasc Dis*. 2008;2:167-77.
1062 8. Moen JM, Matt MG, Ramirez C, Tarasov KV, Chakir K, Tarasova YS, Lukyanenko Y, Tsutsui K,
1063 Monfredi O, Morrell CH, Tagirova S, Yaniv Y, Huynh T, Pacak K, Ahmet I and Lakatta EG. Overexpression
1064 of a Neuronal Type Adenylyl Cyclase (Type 8) in Sinoatrial Node Markedly Impacts Heart Rate and
1065 Rhythm. *Front Neurosci*. 2019;13:615.
1066 9. Lipskaia L, Defer N, Esposito G, Hajar I, Garel MC, Rockman HA and Hanoune J. Enhanced Cardiac
1067 Function in Transgenic Mice Expressing a Ca2+-Stimulated Adenylyl Cyclase. *Circulation Research*.
1068 2000;86:795-801.
1069 10. Mougenot N, Mika D, Czibik G, Marcos E, Abid S, Houssaini A, Vallin B, Guellich A, Mehel H,
1070 Sawaki D, Vandecasteele G, Fischmeister R, Hajjar RJ, Dubois-Rande JL, Limon I, Adnot S, Derumeaux G
1071 and Lipskaia L. Cardiac adenylyl cyclase overexpression precipitates and aggravates age-related
1072 myocardial dysfunction. *Cardiovasc Res*. 2019;115:1778-1790.
1073 11. Liu Y, Zhou K, Li J, Agvanian S, Caldaruse AM, Shaw S, Hitzeman TC, Shaw RM and Hong T. In
1074 Mice Subjected to Chronic Stress, Exogenous cBIN1 Preserves Calcium-Handling Machinery and Cardiac
1075 Function. *JACC Basic Transl Sci*. 2020;5:561-578.
1076 12. Zhang GX, Kimura S, Nishiyama A, Shokoji T, Rahman M, Yao L, Nagai Y, Fujisawa Y, Miyatake A
1077 and Abe Y. Cardiac oxidative stress in acute and chronic isoproterenol-infused rats. *Cardiovasc Res*.
1078 2005;65:230-8.
1079 13. Georget M, Mateo P, Vandecasteele G, Jurevicius J, Lipskaia L, Defer N, Hanoune J, Hoerter J and
1080 Fischmeister R. Augmentation of cardiac contractility with no change in L-type Ca2+ current in
1081 transgenic mice with a cardiac-directed expression of the human adenylyl cyclase type 8 (AC8). *FASEB J*.
1082 2002;16:1636-8.
1083 14. Georget M, Mateo P, Vandecasteele G, Lipskaia L, Defer N, Hanoune J, Hoerter J, Lugnier C and
1084 Fischmeister R. Cyclic AMP compartmentation due to increased cAMP-phosphodiesterase activity in
1085 transgenic mice with a cardiac-directed expression of the human adenylyl cyclase type 8 (AC8). *FASEB J*.
1086 2003;17:1380-91.

1087 15. Hanahan D and Weinberg RA. The hallmarks of cancer. *Cell*. 2000;100:57-70.
1088 16. Hanahan D and Weinberg RA. Hallmarks of cancer: the next generation. *Cell*. 2011;144:646-74.
1089 17. Dorn GW, 2nd. The fuzzy logic of physiological cardiac hypertrophy. *Hypertension*. 2007;49:962-
1090 70.
1091 18. Maillet M, van Berlo JH and Molkentin JD. Molecular basis of physiological heart growth:
1092 fundamental concepts and new players. *Nat Rev Mol Cell Biol*. 2013;14:38-48.
1093 19. Wilkins BJ and Molkentin JD. Calcium-calcineurin signaling in the regulation of cardiac
1094 hypertrophy. *Biochem Biophys Res Commun*. 2004;322:1178-91.
1095 20. Soonpaa MH, Koh GY, Klug MG and Field LJ. Formation of nascent intercalated disks between
1096 grafted fetal cardiomyocytes and host myocardium. *Science*. 1994;264:98-101.
1097 21. Pinson A, Schluter KD, Zhou XJ, Schwartz P, Kessler-Icekson G and Piper HM. Alpha- and beta-
1098 adrenergic stimulation of protein synthesis in cultured adult ventricular cardiomyocytes. *J Mol Cell*
1099 *Cardiol*. 1993;25:477-90.
1100 22. Yamazaki T, Komuro I, Zou Y, Kudoh S, Shiojima I, Hiroi Y, Mizuno T, Aikawa R, Takano H and
1101 Yazaki Y. Norepinephrine induces the raf-1 kinase/mitogen-activated protein kinase cascade through
1102 both alpha 1- and beta-adrenoceptors. *Circulation*. 1997;95:1260-8.
1103 23. Zorov DB, Filburn CR, Klotz LO, Zweier JL and Sollott SJ. Reactive oxygen species (ROS)-induced
1104 ROS release: a new phenomenon accompanying induction of the mitochondrial permeability transition
1105 in cardiac myocytes. *J Exp Med*. 2000;192:1001-14.
1106 24. Juhaszova M, Zorov DB, Kim SH, Pepe S, Fu Q, Fishbein KW, Ziman BD, Wang S, Ytrehus K, Antos
1107 CL, Olson EN and Sollott SJ. Glycogen synthase kinase-3beta mediates convergence of protection
1108 signaling to inhibit the mitochondrial permeability transition pore. *J Clin Invest*. 2004;113:1535-49.
1109 25. Zorov DB, Juhaszova M and Sollott SJ. Mitochondrial reactive oxygen species (ROS) and ROS-
1110 induced ROS release. *Physiol Rev*. 2014;94:909-50.
1111 26. Aon MA, Cortassa S, Juhaszova M, Gonzalez-Reyes JA, Calvo-Rubio M, Villalba JM, Lachance AD,
1112 Ziman BD, Mitchell SJ, Murt KN, Axsom JEC, Alfaras I, Britton SL, Koch LG, de Cabo R, Lakatta EG and
1113 Sollott SJ. Mitochondrial health is enhanced in rats with higher vs. lower intrinsic exercise capacity and
1114 extended lifespan. *NPJ Aging Mech Dis*. 2021;7:1.
1115 27. Liebermeister W, Noor E, Flamholz A, Davidi D, Bernhardt J and Milo R. Visual account of protein
1116 investment in cellular functions. *Proc Natl Acad Sci U S A*. 2014;111:8488-93.
1117 28. Matsuura TR, Leone TC and Kelly DP. Fueling Cardiac Hypertrophy. *Circ Res*. 2020;126:197-199.
1118 29. Ritterhoff J, Young S, Villet O, Shao D, Neto FC, Bettcher LF, Hsu YA, Kolwicz SC, Jr., Raftery D and
1119 Tian R. Metabolic Remodeling Promotes Cardiac Hypertrophy by Directing Glucose to Aspartate
1120 Biosynthesis. *Circ Res*. 2020;126:182-196.
1121 30. Vander Heiden MG, Cantley LC and Thompson CB. Understanding the Warburg effect: the
1122 metabolic requirements of cell proliferation. *Science*. 2009;324:1029-33.
1123 31. Dorn GW, 2nd, Robbins J and Sugden PH. Phenotyping hypertrophy: eschew obfuscation. *Circ*
1124 *Res*. 2003;92:1171-5.
1125 32. Gogiraju R, Schroeter MR, Bochenek ML, Hubert A, Munzel T, Hasenfuss G and Schafer K.
1126 Endothelial deletion of protein tyrosine phosphatase-1B protects against pressure overload-induced
1127 heart failure in mice. *Cardiovasc Res*. 2016;111:204-16.
1128 33. Fleg JL, Schulman S, O'Connor F, Becker LC, Gerstenblith G, Clulow JF, Renlund DG and Lakatta
1129 EG. Effects of acute beta-adrenergic receptor blockade on age-associated changes in cardiovascular
1130 performance during dynamic exercise. *Circulation*. 1994;90:2333-41.
1131 34. Moore RL, Musch TI, Yelamarty RV, Scaduto RC, Jr., Semanchick AM, Elensky M and Cheung JY.
1132 Chronic exercise alters contractility and morphology of isolated rat cardiac myocytes. *Am J Physiol*.
1133 1993;264:C1180-9.

1134 35. Rose BA, Force T and Wang Y. Mitogen-activated protein kinase signaling in the heart: angels
1135 versus demons in a heart-breaking tale. *Physiol Rev*. 2010;90:1507-46.
1136 36. Dixon RE, Hwang SJ, Kim BH, Sanders KM and Ward SM. Myosalpinx Contractions Are Essential
1137 for Egg Transport Along the Oviduct and Are Disrupted in Reproductive Tract Diseases. *Adv Exp Med*
1138 *Biol*. 2019;1124:265-294.
1139 37. Stansfield WE, Andersen NM, Tang RH and Selzman CH. Periostin is a novel factor in cardiac
1140 remodeling after experimental and clinical unloading of the failing heart. *Ann Thorac Surg*.
1141 2009;88:1916-21.
1142 38. Zhao S, Wu H, Xia W, Chen X, Zhu S, Zhang S, Shao Y, Ma W, Yang D and Zhang J. Periostin
1143 expression is upregulated and associated with myocardial fibrosis in human failing hearts. *J Cardiol*.
1144 2014;63:373-8.
1145 39. Ikeda H, Shiojima I, Ozasa Y, Yoshida M, Holzenberger M, Kahn CR, Walsh K, Igarashi T, Abel ED
1146 and Komuro I. Interaction of myocardial insulin receptor and IGF receptor signaling in exercise-induced
1147 cardiac hypertrophy. *J Mol Cell Cardiol*. 2009;47:664-75.
1148 40. Varga I, Polak S, Kyselovic J, Kachlik D, Danisovic L and Klein M. Recently Discovered Interstitial
1149 Cell Population of Telocytes: Distinguishing Facts from Fiction Regarding Their Role in the Pathogenesis
1150 of Diverse Diseases Called "Telocytopathies". *Medicina (Kaunas)*. 2019;55.
1151 41. Esposito G, Perrino C, Ozaki T, Takaoka H, Defer N, Petretta MP, De Angelis MC, Mao L, Hanoune
1152 J, Rockman HA and Chiariello M. Increased myocardial contractility and enhanced exercise function in
1153 transgenic mice overexpressing either adenylyl cyclase 5 or 8. *Basic Res Cardiol*. 2008;103:22-30.
1154 42. Fajardo VM, Feng I, Chen BY, Perez-Ramirez CA, Shi B, Clark P, Tian R, Lien CL, Pellegrini M,
1155 Christofk H, Nakano H and Nakano A. GLUT1 overexpression enhances glucose metabolism and
1156 promotes neonatal heart regeneration. *Sci Rep*. 2021;11:8669.
1157 43. Smoak IW and Branch S. Glut-1 expression and its response to hypoglycemia in the embryonic
1158 mouse heart. *Anat Embryol (Berl)*. 2000;201:327-33.
1159 44. Brosius FC, 3rd, Liu Y, Nguyen N, Sun D, Bartlett J and Schwaiger M. Persistent myocardial
1160 ischemia increases GLUT1 glucose transporter expression in both ischemic and non-ischemic heart
1161 regions. *J Mol Cell Cardiol*. 1997;29:1675-85.
1162 45. Razeghi P, Young ME, Alcorn JL, Moravec CS, Frazier OH and Taegtmeyer H. Metabolic gene
1163 expression in fetal and failing human heart. *Circulation*. 2001;104:2923-31.
1164 46. Wang KC, Botting KJ, Zhang S, McMillen IC, Brooks DA and Morrison JL. Akt signaling as a
1165 mediator of cardiac adaptation to low birth weight. *J Endocrinol*. 2017;233:R81-R94.
1166 47. Sousa Fialho MDL, Abd Jamil AH, Stannard GA and Heather LC. Hypoxia-inducible factor 1
1167 signalling, metabolism and its therapeutic potential in cardiovascular disease. *Biochim Biophys Acta Mol*
1168 *Basis Dis*. 2019;1865:831-843.
1169 48. Krishnan J, Suter M, Windak R, Krebs T, Felley A, Montessuit C, Tokarska-Schlattner M, Aasum E,
1170 Bogdanova A, Perriard E, Perriard JC, Larsen T, Pedrazzini T and Krek W. Activation of a HIF1alpha-
1171 PPARgamma axis underlies the integration of glycolytic and lipid anabolic pathways in pathologic cardiac
1172 hypertrophy. *Cell Metab*. 2009;9:512-24.
1173 49. West MD, Labat I, Sternberg H, Larocca D, Nasonkin I, Chapman KB, Singh R, Makarev E, Aliper A,
1174 Kazennov A, Alekseenko A, Shuvalov N, Cheskidova E, Alekseev A, Artemov A, Putin E, Mamoshina P,
1175 Pryanichnikov N, Larocca J, Copeland K, Izumchenko E, Korzinkin M and Zhavoronkov A. Use of deep
1176 neural network ensembles to identify embryonic-fetal transition markers: repression of COX7A1 in
1177 embryonic and cancer cells. *Oncotarget*. 2018;9:7796-7811.
1178 50. Brooks GA. Mammalian fuel utilization during sustained exercise. *Comp Biochem Physiol B*
1179 *Biochem Mol Biol*. 1998;120:89-107.
1180 51. Safer B, Smith CM and Williamson JR. Control of the transport of reducing equivalents across the
1181 mitochondrial membrane in perfused rat heart. *J Mol Cell Cardiol*. 1971;2:111-24.

1182 52. Kane DA. Lactate oxidation at the mitochondria: a lactate-malate-aspartate shuttle at work.
1183 *Front Neurosci*. 2014;8:366.
1184 53. O'Donnell JM, Kudej RK, LaNoue KF, Vatner SF and Lewandowski ED. Limited transfer of cytosolic
1185 NADH into mitochondria at high cardiac workload. *Am J Physiol Heart Circ Physiol*. 2004;286:H2237-42.
1186 54. Robergs RA, Ghiasvand F and Parker D. Biochemistry of exercise-induced metabolic acidosis. *Am*
1187 *J Physiol Regul Integr Comp Physiol*. 2004;287:R502-16.
1188 55. Yet SF, Tian R, Layne MD, Wang ZY, Maemura K, Solovyeva M, Ith B, Melo LG, Zhang L, Ingwall
1189 JS, Dzau VJ, Lee ME and Perrella MA. Cardiac-specific expression of heme oxygenase-1 protects against
1190 ischemia and reperfusion injury in transgenic mice. *Circ Res*. 2001;89:168-73.
1191 56. Zhao Y, Zhang L, Qiao Y, Zhou X, Wu G, Wang L, Peng Y, Dong X, Huang H, Si L, Zhang X, Zhang L,
1192 Li J, Wang W, Zhou L and Gao X. Heme oxygenase-1 prevents cardiac dysfunction in streptozotocin-
1193 diabetic mice by reducing inflammation, oxidative stress, apoptosis and enhancing autophagy. *PLoS One*.
1194 2013;8:e75927.
1195 57. Cui M, Atmanli A, Morales MG, Tan W, Chen K, Xiao X, Xu L, Liu N, Bassel-Duby R and Olson EN.
1196 Nrf1 promotes heart regeneration and repair by regulating proteostasis and redox balance. *Nat*
1197 *Commun*. 2021;12:5270.
1198 58. Vanhaesebroeck B, Guillermet-Guibert J, Graupera M and Bilanges B. The emerging mechanisms
1199 of isoform-specific PI3K signalling. *Nat Rev Mol Cell Biol*. 2010;11:329-41.
1200 59. Nienaber JJ, Tachibana H, Naga Prasad SV, Esposito G, Wu D, Mao L and Rockman HA. Inhibition
1201 of receptor-localized PI3K preserves cardiac beta-adrenergic receptor function and ameliorates pressure
1202 overload heart failure. *J Clin Invest*. 2003;112:1067-79.
1203 60. Naga Prasad SV, Laporte SA, Chamberlain D, Caron MG, Barak L and Rockman HA.
1204 Phosphoinositide 3-kinase regulates beta2-adrenergic receptor endocytosis by AP-2 recruitment to the
1205 receptor/beta-arrestin complex. *J Cell Biol*. 2002;158:563-75.
1206 61. Patrucco E, Notte A, Barberis L, Selvetella G, Maffei A, Brancaccio M, Marengo S, Russo G,
1207 Azzolino O, Rybalkin SD, Silengo L, Altruda F, Wetzker R, Wymann MP, Lembo G and Hirsch E.
1208 PI3Kgamma modulates the cardiac response to chronic pressure overload by distinct kinase-dependent
1209 and -independent effects. *Cell*. 2004;118:375-87.
1210 62. Perino A, Ghigo A, Damilano F and Hirsch E. Identification of the macromolecular complex
1211 responsible for PI3Kgamma-dependent regulation of cAMP levels. *Biochem Soc Trans*. 2006;34:502-3.
1212 63. Morisco C, Zebrowski D, Condorelli G, Tsichlis P, Vatner SF and Sadoshima J. The Akt-glycogen
1213 synthase kinase 3beta pathway regulates transcription of atrial natriuretic factor induced by beta-
1214 adrenergic receptor stimulation in cardiac myocytes. *J Biol Chem*. 2000;275:14466-75.
1215 64. Schluter KD, Goldberg Y, Taimor G, Schafer M and Piper HM. Role of phosphatidylinositol 3-
1216 kinase activation in the hypertrophic growth of adult ventricular cardiomyocytes. *Cardiovasc Res*.
1217 1998;40:174-81.
1218 65. Jo SH, Leblais V, Wang PH, Crow MT and Xiao RP. Phosphatidylinositol 3-kinase functionally
1219 compartmentalizes the concurrent G(s) signaling during beta2-adrenergic stimulation. *Circ Res*.
1220 2002;91:46-53.
1221 66. Leblais V, Jo SH, Chakir K, Maltsev V, Zheng M, Crow MT, Wang W, Lakatta EG and Xiao RP.
1222 Phosphatidylinositol 3-kinase offsets cAMP-mediated positive inotropic effect via inhibiting Ca2+ influx
1223 in cardiomyocytes. *Circ Res*. 2004;95:1183-90.
1224 67. Oudit GY, Crackower MA, Eriksson U, Sarao R, Kozieradzki I, Sasaki T, Irie-Sasaki J, Gidrewicz D,
1225 Rybin VO, Wada T, Steinberg SF, Backx PH and Penninger JM. Phosphoinositide 3-kinase gamma-
1226 deficient mice are protected from isoproterenol-induced heart failure. *Circulation*. 2003;108:2147-52.
1227 68. Lips DJ, Bueno OF, Wilkins BJ, Purcell NH, Kaiser RA, Lorenz JN, Voisin L, Saba-El-Leil MK,
1228 Meloche S, Pouyssegur J, Pages G, De Windt LJ, Doevendans PA and Molkentin JD. MEK1-ERK2 signaling
1229 pathway protects myocardium from ischemic injury in vivo. *Circulation*. 2004;109:1938-41.

1230 69. Bassat E, Mutlak YE, Genzelinakh A, Shadrin IY, Baruch Umansky K, Yifa O, Kain D, Rajchman D,
1231 Leach J, Riabov Bassat D, Udi Y, Sarig R, Sagi I, Martin JF, Bursac N, Cohen S and Tzahor E. The
1232 extracellular matrix protein agrin promotes heart regeneration in mice. *Nature*. 2017;547:179-184.
1233 70. de Jonge N, Goumans MJ, Lips D, Hassink R, Vlug EJ, van der Meel R, Emmerson CD, Nijman J, de
1234 Windt L and Doevendans PA. Controlling cardiomyocyte survival. *Novartis Found Symp*. 2006;274:41-51;
1235 discussion 51-7, 152-5, 272-6.
1236 71. DeBosch B, Treskov I, Lupu TS, Weinheimer C, Kovacs A, Courtois M and Muslin AJ. Akt1 is
1237 required for physiological cardiac growth. *Circulation*. 2006;113:2097-104.
1238 72. Antos CL, McKinsey TA, Frey N, Kutschke W, McAnally J, Shelton JM, Richardson JA, Hill JA and
1239 Olson EN. Activated glycogen synthase-3 beta suppresses cardiac hypertrophy in vivo. *Proc Natl Acad Sci*
1240 *U S A*. 2002;99:907-12.
1241 73. Moc C, Taylor AE, Chesini GP, Zambrano CM, Barlow MS, Zhang X, Gustafsson AB and Purcell NH.
1242 Physiological activation of Akt by PHLPP1 deletion protects against pathological hypertrophy. *Cardiovasc*
1243 *Res*. 2015;105:160-70.
1244 74. Freed DH, Borowiec AM, Angelovska T and Dixon IM. Induction of protein synthesis in cardiac
1245 fibroblasts by cardiotrophin-1: integration of multiple signaling pathways. *Cardiovasc Res*. 2003;60:365-
1246 75.
1247 75. Das S, Dixon JE and Cho W. Membrane-binding and activation mechanism of PTEN. *Proc Natl*
1248 *Acad Sci U S A*. 2003;100:7491-6.
1249 76. Torres J and Pulido R. The tumor suppressor PTEN is phosphorylated by the protein kinase CK2
1250 at its C terminus. Implications for PTEN stability to proteasome-mediated degradation. *J Biol Chem*.
1251 2001;276:993-8.
1252 77. Vazquez F, Ramaswamy S, Nakamura N and Sellers WR. Phosphorylation of the PTEN tail
1253 regulates protein stability and function. *Mol Cell Biol*. 2000;20:5010-8.
1254 78. Czech MP. PIP2 and PIP3: complex roles at the cell surface. *Cell*. 2000;100:603-6.
1255 79. Yang B, Yan P, Gong H, Zuo L, Shi Y, Guo J, Guo R, Xie J and Li B. TWEAK protects cardiomyocyte
1256 against apoptosis in a PI3K/AKT pathway dependent manner. *Am J Transl Res*. 2016;8:3848-3860.
1257 80. Abeyrathna P and Su Y. The critical role of Akt in cardiovascular function. *Vascul Pharmacol*.
1258 2015;74:38-48.
1259 81. Ghigo A and Li M. Phosphoinositide 3-kinase: friend and foe in cardiovascular disease. *Front*
1260 *Pharmacol*. 2015;6:169.
1261 82. Khalil H, Bertrand MJ, Vandenabeele P and Widmann C. Caspase-3 and RasGAP: a stress-sensing
1262 survival/demise switch. *Trends Cell Biol*. 2014;24:83-9.
1263 83. Choi J, Park JE, Tsagkogeorga G, Yanagita M, Koo BK, Han N and Lee JH. Inflammatory Signals
1264 Induce AT2 Cell-Derived Damage-Associated Transient Progenitors that Mediate Alveolar Regeneration.
1265 *Cell Stem Cell*. 2020;27:366-382 e7.
1266 84. Lindborg JA, Tran NM, Chenette DM, DeLuca K, Foli Y, Kannan R, Sekine Y, Wang X, Wollan M,
1267 Kim IJ, Sanes JR and Strittmatter SM. Optic nerve regeneration screen identifies multiple genes
1268 restricting adult neural repair. *Cell Rep*. 2021;34:108777.
1269 85. Pradervand S, Yasukawa H, Muller OG, Kjekshus H, Nakamura T, St Amand TR, Yajima T,
1270 Matsumura K, Duplain H, Iwatate M, Woodard S, Pedrazzini T, Ross J, Firsov D, Rossier BC, Hoshijima M
1271 and Chien KR. Small proline-rich protein 1A is a gp130 pathway- and stress-inducible cardioprotective
1272 protein. *EMBO J*. 2004;23:4517-25.
1273 86. Shah H, Hacker A, Langburt D, Dewar M, McFadden MJ, Zhang H, Kuzmanov U, Zhou YQ, Hussain
1274 B, Ehsan F, Hinz B, Gramolini AO and Heximer SP. Myocardial Infarction Induces Cardiac Fibroblast
1275 Transformation within Injured and Noninjured Regions of the Mouse Heart. *J Proteome Res*.
1276 2021;20:2867-2881.

1277 87. Steiner P, Kulangara K, Sarria JC, Glauser L, Regazzi R and Hirling H. Reticulon 1-
1278 C/neuroendocrine-specific protein-C interacts with SNARE proteins. *J Neurochem*. 2004;89:569-80.
1279 88. van de Velde HJ, Roebroek AJ, Senden NH, Ramaekers FC and Van de Ven WJ. NSP-encoded
1280 reticulons, neuroendocrine proteins of a novel gene family associated with membranes of the
1281 endoplasmic reticulum. *J Cell Sci*. 1994;107 (Pt 9):2403-16.
1282 89. Adamo L, Rocha-Resende C, Prabhu SD and Mann DL. Reappraising the role of inflammation in
1283 heart failure. *Nat Rev Cardiol*. 2020;17:269-285.
1284 90. Adamo L, Staloch LJ, Rocha-Resende C, Matkovich SJ, Jiang W, Bajpai G, Weinheimer CJ, Kovacs
1285 A, Schilling JD, Barger PM, Bhattacharya D and Mann DL. Modulation of subsets of cardiac B
1286 lymphocytes improves cardiac function after acute injury. *JCI Insight*. 2018;3.
1287 91. Juilland M and Thome M. Role of the CARMA1/BCL10/MALT1 complex in lymphoid
1288 malignancies. *Curr Opin Hematol*. 2016;23:402-9.
1289 92. Craige SM, Chen K, Blanton RM, Keaney JF, Jr. and Kant S. JNK and cardiometabolic dysfunction.
1290 *Biosci Rep*. 2019;39.
1291 93. Sadoshima J, Montagne O, Wang Q, Yang G, Warden J, Liu J, Takagi G, Karoor V, Hong C, Johnson
1292 GL, Vatner DE and Vatner SF. The MEKK1-JNK pathway plays a protective role in pressure overload but
1293 does not mediate cardiac hypertrophy. *J Clin Invest*. 2002;110:271-9.
1294 94. Kaiser RA, Liang Q, Bueno O, Huang Y, Lackey T, Klevitsky R, Hewett TE and Molkentin JD.
1295 Genetic inhibition or activation of JNK1/2 protects the myocardium from ischemia-reperfusion-induced
1296 cell death in vivo. *J Biol Chem*. 2005;280:32602-8.
1297 95. Juhaszova M, Rabuel C, Zorov DB, Lakatta EG and Sollott SJ. Protection in the aged heart:
1298 preventing the heart-break of old age? *Cardiovasc Res*. 2005;66:233-44.
1299 96. Fulghum K and Hill BG. Metabolic Mechanisms of Exercise-Induced Cardiac Remodeling. *Front*
1300 *Cardiovasc Med*. 2018;5:127.
1301 97. Cortassa S, Caceres V, Bell LN, O'Rourke B, Paolocci N and Aon MA. From metabolomics to
1302 fluxomics: a computational procedure to translate metabolite profiles into metabolic fluxes. *Biophys J*.
1303 2015;108:163-72.

1304

Figure 1

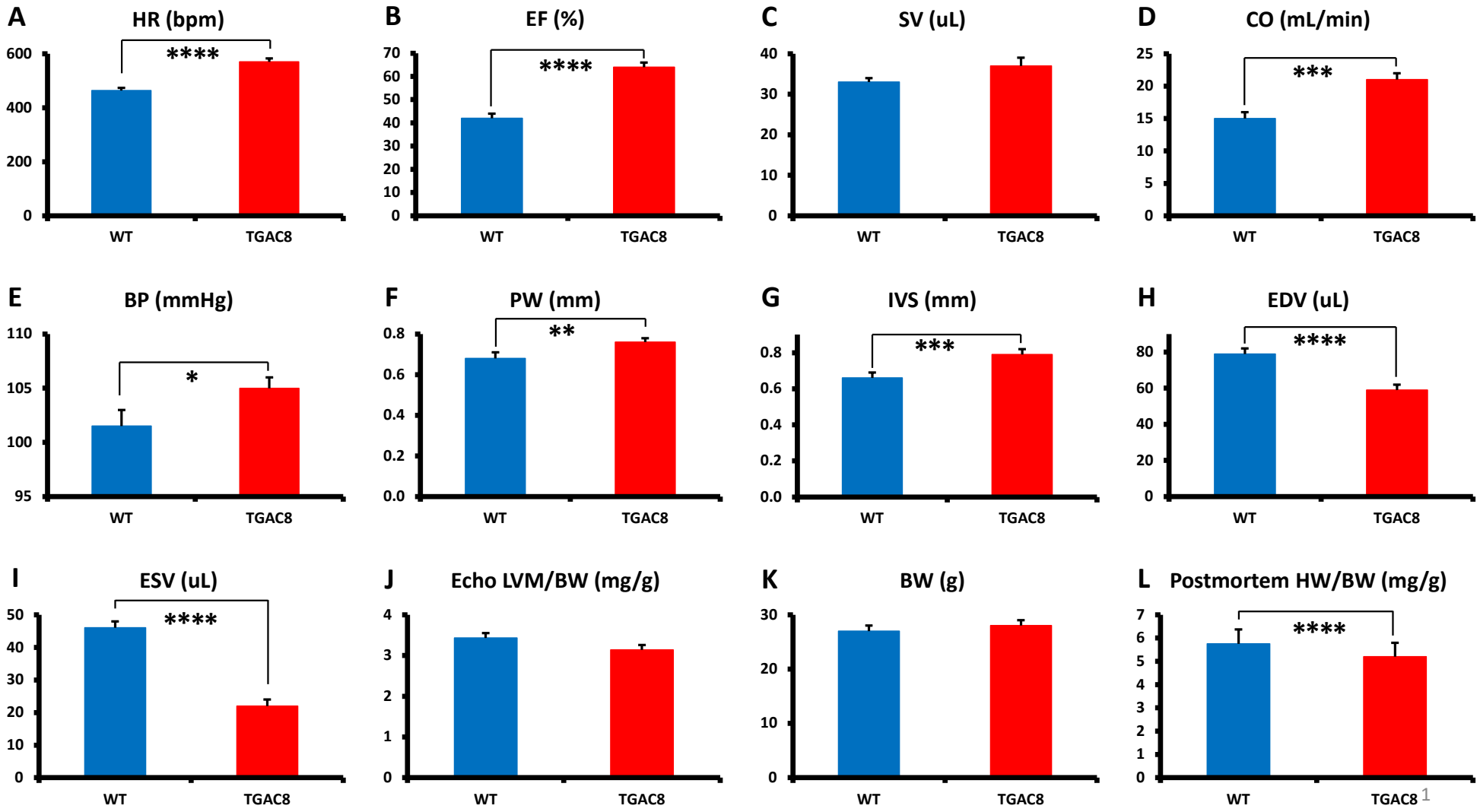
A
HR (bpm)
600
400
200
0
****
WT
TGAC8
B
EF (%)
70
60
50
40
30
20
10
0
****
WT
TGAC8
C
SV (uL)
40
30
20
10
0
WT
TGAC8
D
CO (mL/min)
25
20
15
10
5
0
***
WT
TGAC8
E
BP (mmHg)
110
105
100
95
*
WT
TGAC8
F
PW (mm)
0.8
0.6
0.4
0.2
0.0
**
WT
TGAC8
G
IVS (mm)
0.8
0.6
0.4
0.2
0.0
***
WT
TGAC8
H
EDV (uL)
80
60
40
20
0
****
WT
TGAC8
I
ESV (uL)
50
40
30
20
10
0
****
WT
TGAC8
J
Echo LVM/BW (mg/g)
4
3
2
1
0
WT
TGAC8
K
BW (g)
30
20
10
0
WT
TGAC8
L
Postmortem HW/BW (mg/g)
7
6
5
4
3
2
1
0
****
WT
TGAC8

Figure 2

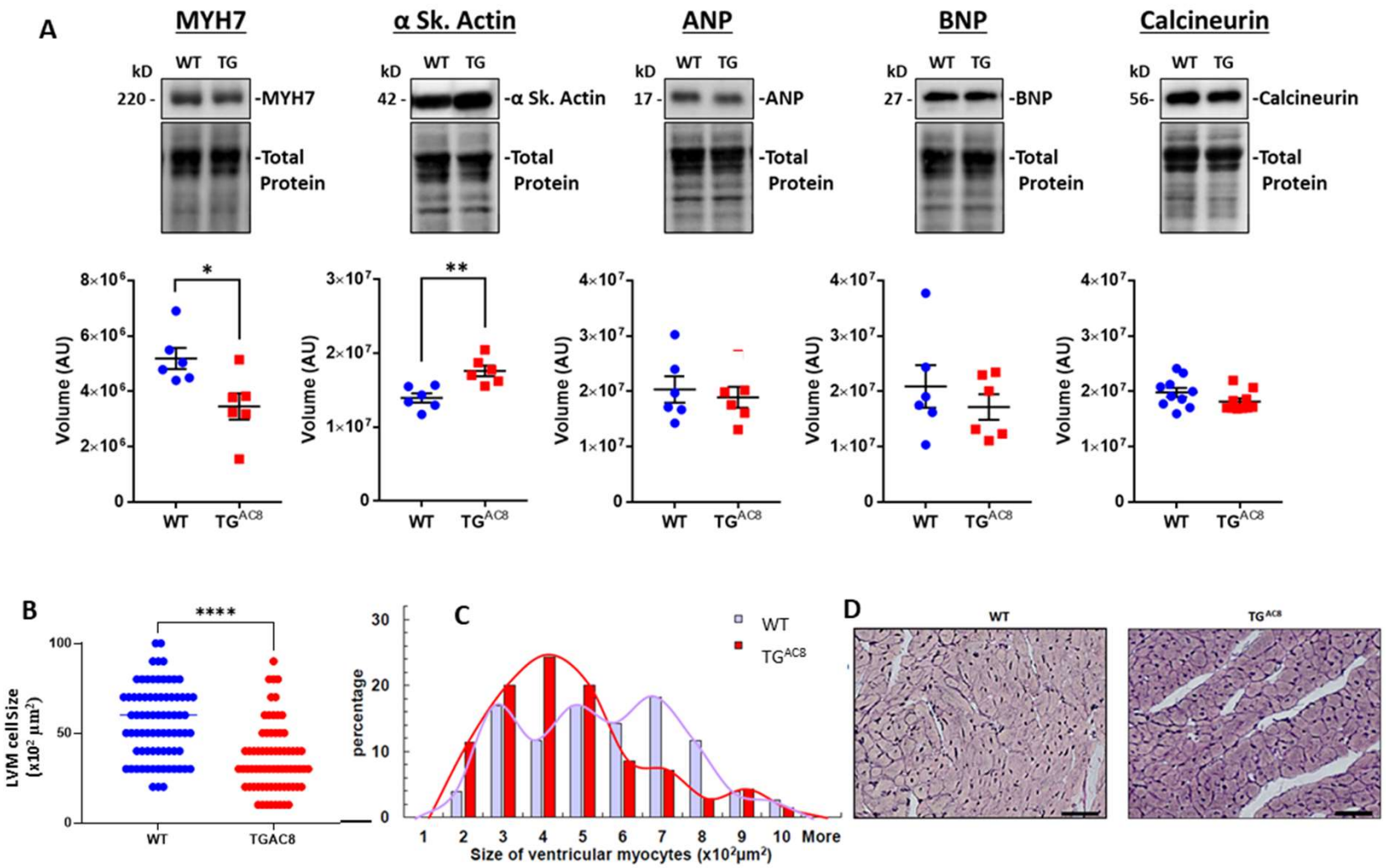
A
MYH7
α Sk. Actin
ANP
BNP
Calcineurin
kD
WT TG
220 -
-MYH7
42 -
-α Sk. Actin
17 -
-ANP
27 -
-BNP
56-
-Calcineurin
-Total Protein
Volume (AU)
WT
TGAC8
B
****
LVM cell Size (x10² µm²)
TGAC8
C
percentage
Size of ventricular myocytes (x10²µm²)
More
D

Figure 3

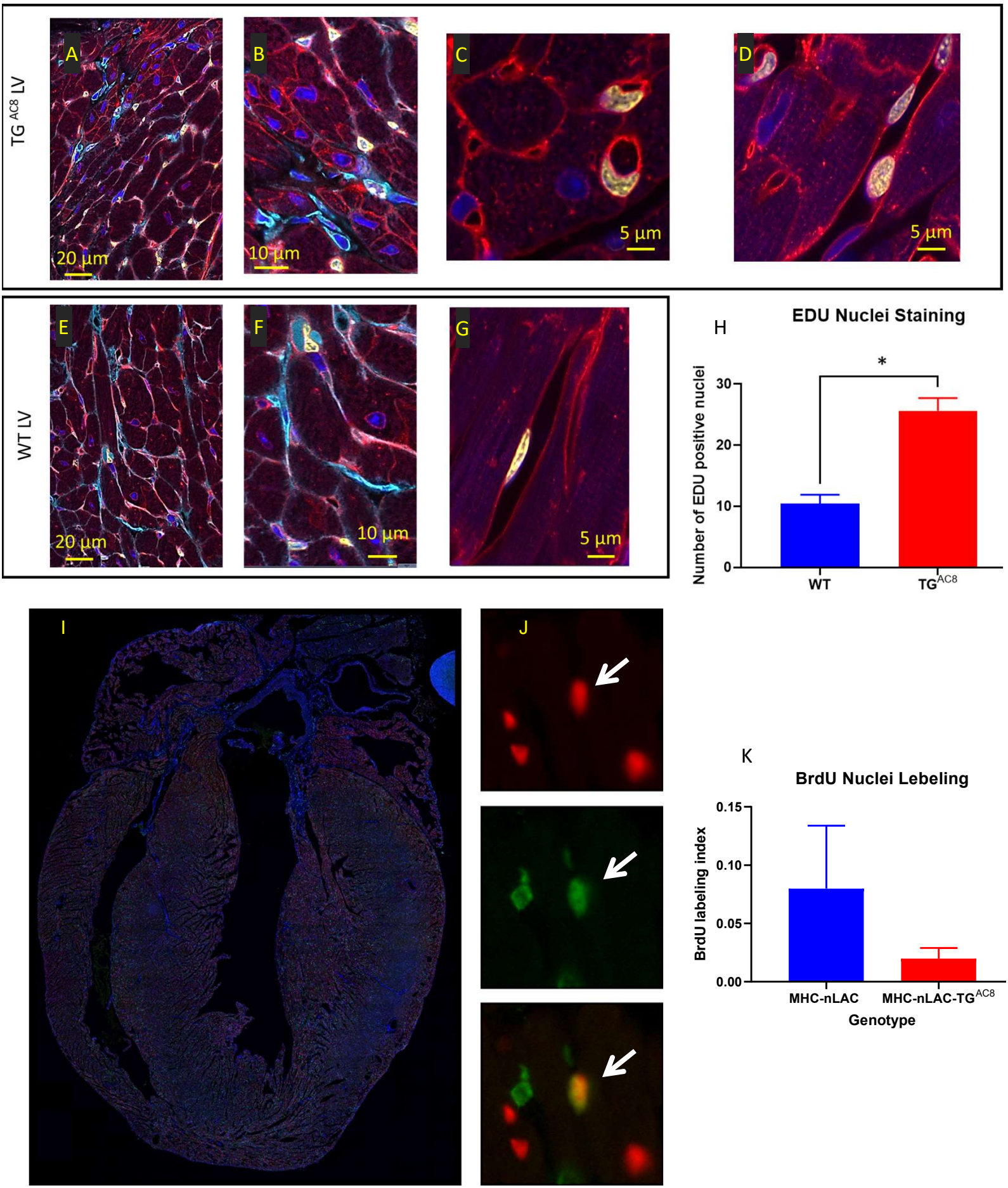
TG AC8 LV
A
20 µm
B
10 µm
C
5 µm
D
5 µm
WT LV
E
20 µm
F
10 µm
G
5 µm
H
EDU Nuclei Staining
Number of EDU positive nuclei
30
20
10
0
*
WT
TG AC8
I
J
K
BrdU Nuclei Lebeling
BrdU labeling index
0.15
0.10
0.05
0.00
MHC-nLAC
MHC-nLAC-TG AC8
Genotype

Figure 4

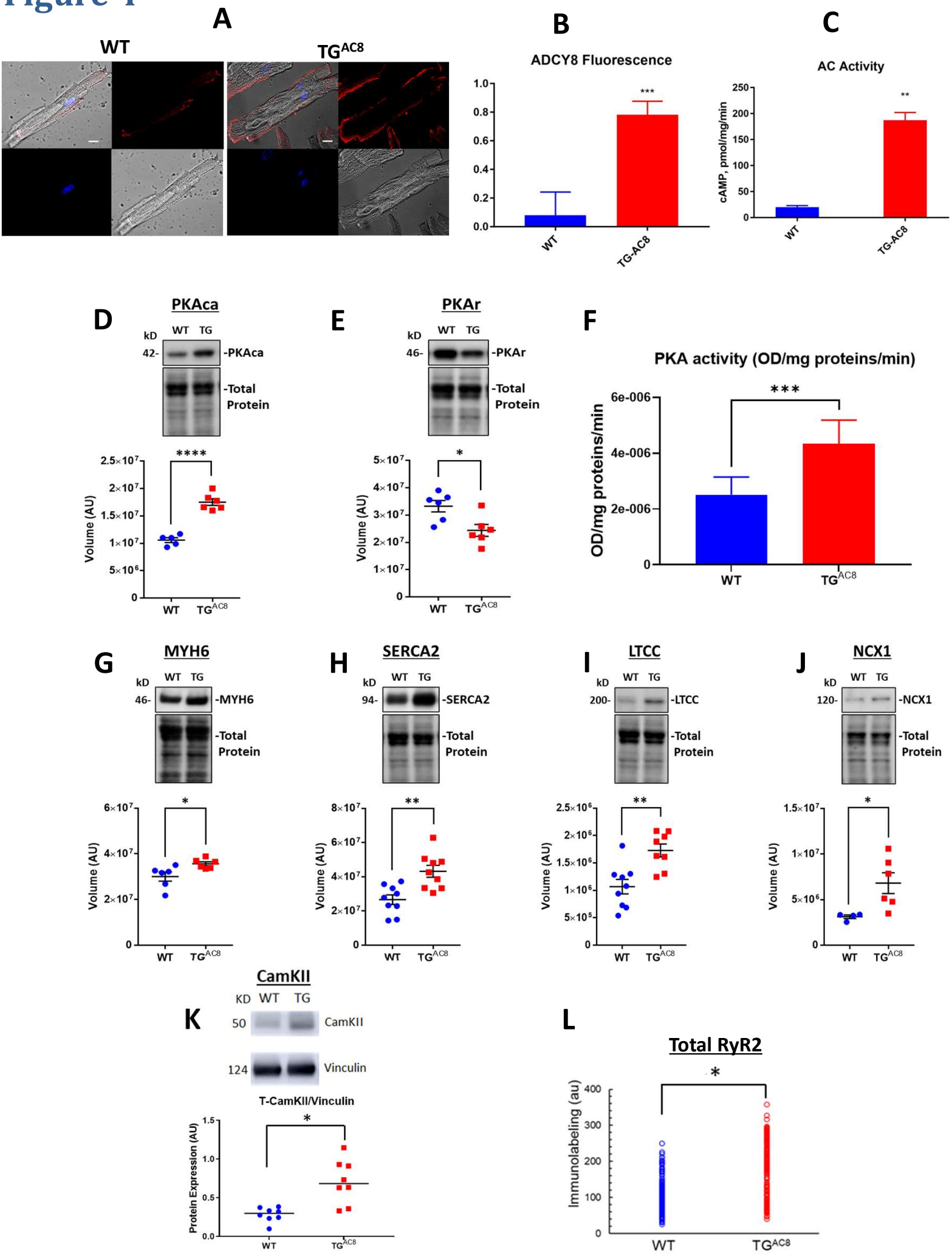
A
WT
TGAC8
B
ADCY8 Fluorescence
***
WT
TG-AC8
C
AC Activity
cAMP, pmol/mg/min
**
WT
TG-AC8
D
PKAca
kD
WT TG
42-
-PKAca
-Total Protein
****
Volume (AU)
WT
TGAC8
E
PKAr
kD
WT TG
46-
-PKAr
-Total Protein
*
Volume (AU)
WT
TGAC8
F
PKA activity (OD/mg proteins/min)
***
OD/mg proteins/min
WT
TGAC8
G
MYH6
kD
WT TG
46-
-MYH6
-Total Protein
*
Volume (AU)
WT
TGAC8
H
SERCA2
kD
WT TG
94-
-SERCA2
-Total Protein
**
Volume (AU)
WT
TGAC8
I
LTCC
kD
WT TG
200-
-LTCC
-Total Protein
**
Volume (AU)
WT
TGAC8
J
NCX1
kD
WT TG
120-
-NCX1
-Total Protein
*
Volume (AU)
WT
TGAC8
K
CamKII
KD
WT TG
50
CamKII
124
Vinculin
T-CamKII/Vinculin
*
Protein Expression (AU)
WT
TGAC8
L
Total RyR2
*
Immunolabeling (au)
WT
TGAC8

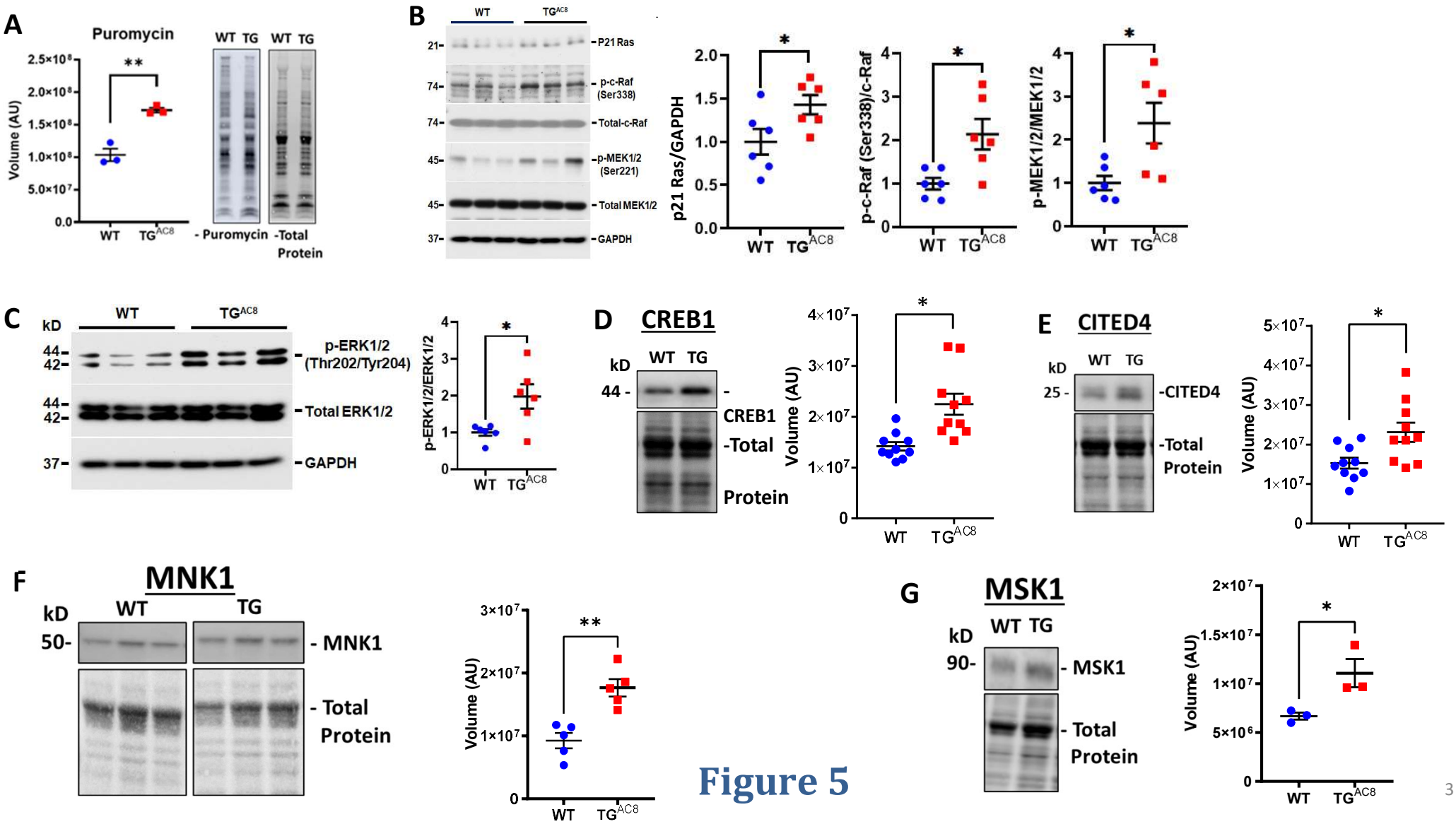
A
Puromycin
Volume (AU)
WT
TGAC8
- Puromycin
-Total Protein
B
P21 Ras
p-c-Raf (Ser338)
Total-c-Raf
p-MEK1/2 (Ser221)
Total MEK1/2
GAPDH
p21 Ras/GAPDH
p-c-Raf (Ser338)/c-Raf
p-MEK1/2/MEK1/2
C
kD
p-ERK1/2 (Thr202/Tyr204)
Total ERK1/2
GAPDH
p-ERK1/2/ERK1/2
D
CREB1
-Total Protein
E
CITED4
-CITED4
-Total Protein
F
MNK1
- MNK1
- Total Protein
G
MSK1
- MSK1
- Total Protein

Figure 5

Figure 6

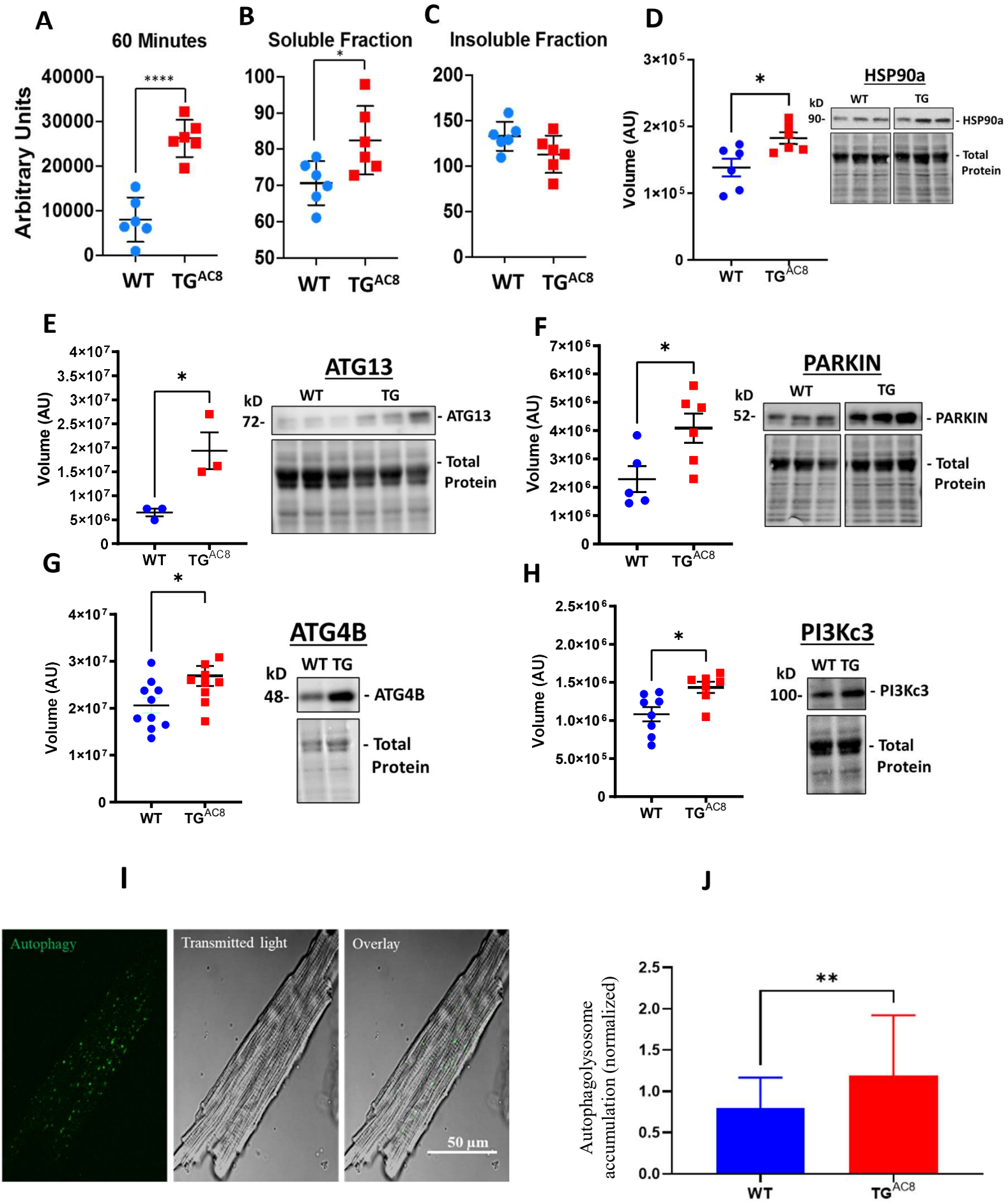
A
60 Minutes
Arbitrary Units
40000
30000
20000
10000
0
****
WT
TGAC8
B
Soluble Fraction
100
90
80
70
60
50
*
WT
TGAC8
C
Insoluble Fraction
200
150
100
50
0
WT
TGAC8
D
3×10^5
2×10^5
1×10^5
0
Volume (AU)
*
WT
TGAC8
HSP90a
kD
90-
WT
TG
- HSP90a
- Total Protein
E
4×10^7
3.5×10^7
3×10^7
2.5×10^7
2×10^7
1.5×10^7
1×10^7
5×10^6
0
Volume (AU)
*
WT
TGAC8
ATG13
kD
72-
WT
TG
- ATG13
- Total Protein
F
7×10^6
6×10^6
5×10^6
4×10^6
3×10^6
2×10^6
1×10^6
0
Volume (AU)
*
WT
TGAC8
PARKIN
kD
52-
WT
TG
- PARKIN
- Total Protein
G
4×10^7
3×10^7
2×10^7
1×10^7
0
Volume (AU)
*
WT
TGAC8
ATG4B
kD
48-
WT TG
- ATG4B
- Total Protein
H
2.5×10^6
2.0×10^6
1.5×10^6
1.0×10^6
5.0×10^5
0
Volume (AU)
*
WT
TGAC8
PI3Kc3
kD
100-
WT TG
- PI3Kc3
- Total Protein
I
Autophagy
Transmitted light
Overlay
50 µm
J
Autophagolysosome accumulation (normalized)
2.5
2.0
1.5
1.0
0.5
0.0
**
WT
TGAC8

Figure 7

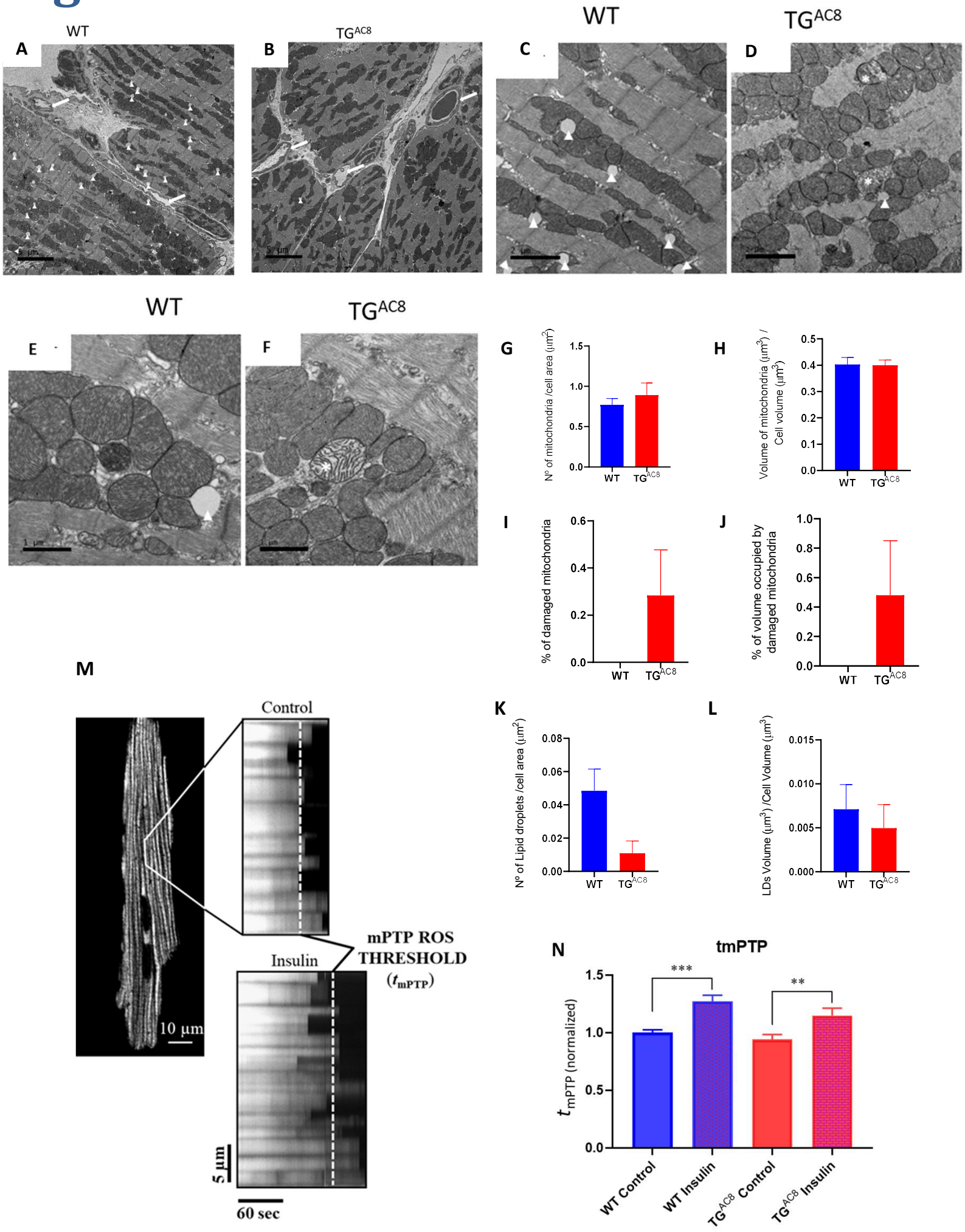
A
WT
B
TGAC8
C
WT
D
TGAC8
E
WT
F
TGAC8
G
Nº of mitochondria /cell area (µm2)
H
Volume of mitochondria (µm3) / Cell volume (µm3)
I
% of damaged mitochondria
J
% of volume occupied by damaged mitochondria
K
Nº of Lipid droplets /cell area (µm2)
L
LDs Volume (µm3) /Cell Volume (µm3)
M
Control
Insulin
mPTP ROS THRESHOLD (t_{mPTP})
10 µm
5 µm
60 sec
N
tmPTP
t_{mPTP} (normalized)
***
**
WT Control
WT Insulin
TGAC8 Control
TGAC8 Insulin

Figure 8

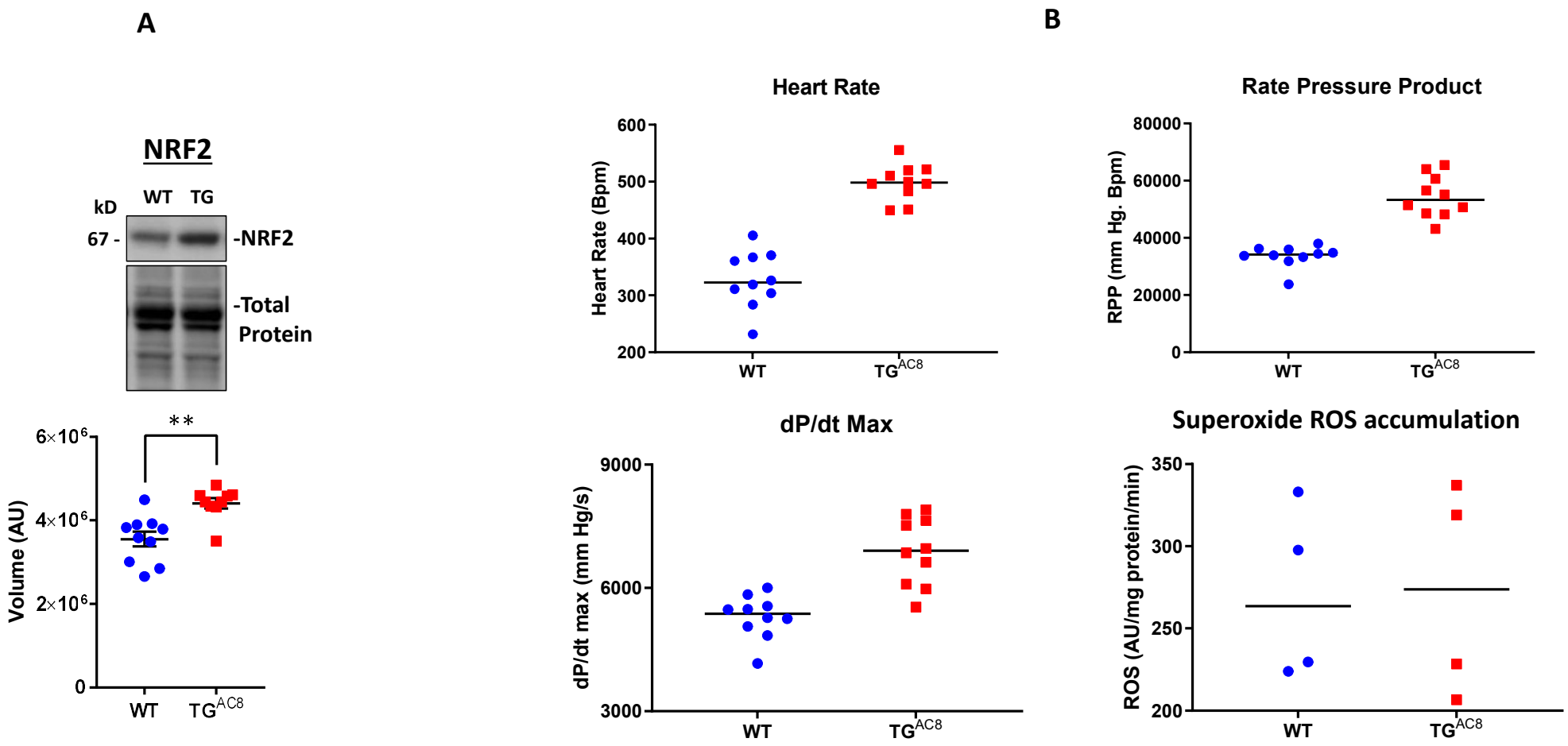
A
NRF2
kD
WT
TG
67 -
-NRF2
-Total
Protein
**
6×10⁶
4×10⁶
2×10⁶
0
Volume (AU)
WT
TGAC8
B
Heart Rate
Heart Rate (Bpm)
600
500
400
300
200
WT
TGAC8
Rate Pressure Product
RPP (mm Hg. Bpm)
80000
60000
40000
20000
0
WT
TGAC8
dP/dt Max
dP/dt max (mm Hg/s)
9000
6000
3000
WT
TGAC8
Superoxide ROS accumulation
ROS (AU/mg protein/min)
350
300
250
200
WT
TGAC8

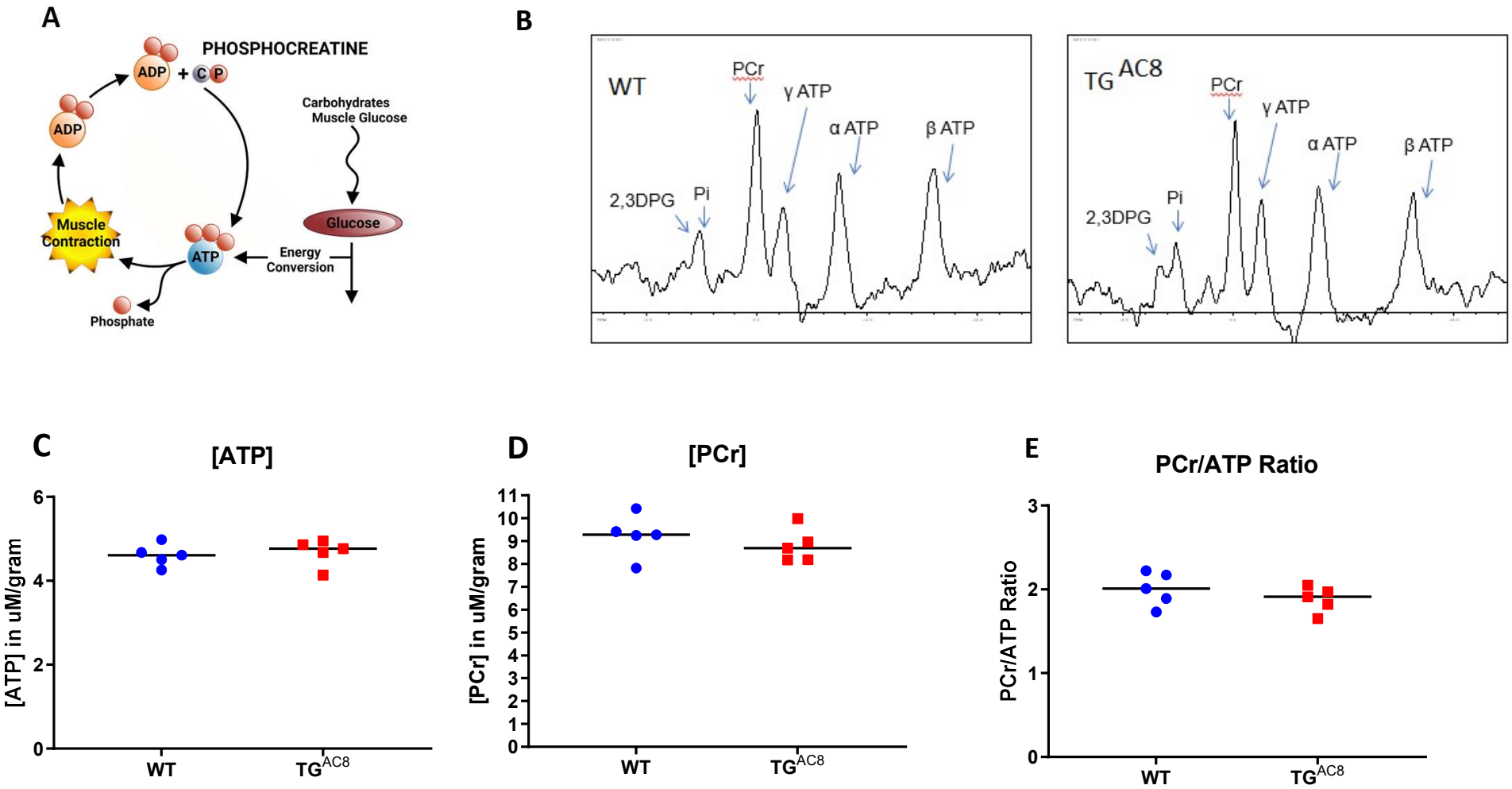
A
PHOSPHOCREATINE
ADP
+ C P
ADP
Carbohydrates
Muscle Glucose
Muscle Contraction
ATP
Glucose
Energy Conversion
Phosphate
B
WT
PCr
γ ATP
α ATP
β ATP
2,3DPG
Pi
TG AC8
PCr
γ ATP
α ATP
β ATP
2,3DPG
Pi
C
[ATP]
[ATP] in uM/gram
0
2
4
6
WT
TGAC8
D
[PCr]
[PCr] in uM/gram
0
1
2
3
4
5
6
7
8
9
10
11
WT
TGAC8
E
PCr/ATP Ratio
PCr/ATP Ratio
0
1
2
3
WT
TGAC8

Figure 9

Figure 10

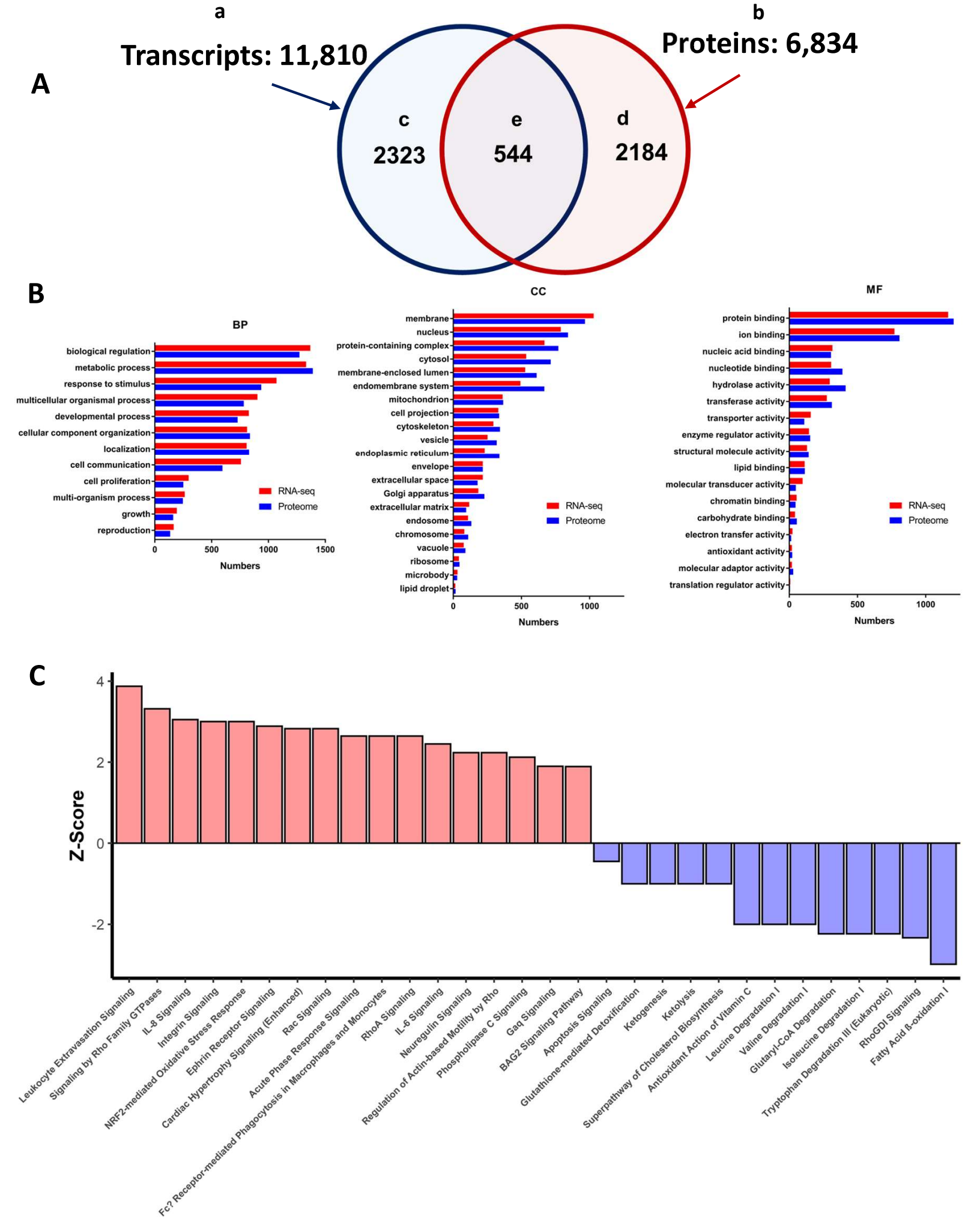
A
a
Transcripts: 11,810
b
Proteins: 6,834
c
2323
e
544
d
2184
B
BP
biological regulation
metabolic process
response to stimulus
multicellular organismal process
developmental process
cellular component organization
localization
cell communication
cell proliferation
multi-organism process
growth
reproduction
RNA-seq
Proteome
0
500
1000
1500
Numbers
CC
membrane
nucleus
protein-containing complex
cytosol
membrane-enclosed lumen
endomembrane system
mitochondrion
cell projection
cytoskeleton
vesicle
endoplasmic reticulum
envelope
extracellular space
Golgi apparatus
extracellular matrix
endosome
chromosome
vacuole
ribosome
microbody
lipid droplet
RNA-seq
Proteome
0
500
1000
Numbers
MF
protein binding
ion binding
nucleic acid binding
nucleotide binding
hydrolase activity
transferase activity
transporter activity
enzyme regulator activity
structural molecule activity
lipid binding
molecular transducer activity
chromatin binding
carbohydrate binding
electron transfer activity
antioxidant activity
molecular adaptor activity
translation regulator activity
RNA-seq
Proteome
0
500
1000
Numbers
C
Z-Score
4
2
0
-2
Leukocyte Extravasation Signaling
Signaling by Rho Family GTPases
IL-8 Signaling
Integrin Signaling
NRF2-mediated Oxidative Stress Response
Ephrin Receptor Signaling
Cardiac Hypertrophy Signaling (Enhanced)
Rac Signaling
Acute Phase Response Signaling
Fc? Receptor-mediated Phagocytosis in Macrophages and Monocytes
RhoA Signaling
IL-6 Signaling
Neuregulin Signaling
Regulation of Actin-based Motility by Rho
Phospholipase C Signaling
Gaq Signaling
BAG2 Signaling Pathway
Apoptosis Signaling
Glutathione-mediated Detoxification
Ketogenesis
Ketolysis
Superpathway of Cholesterol Biosynthesis
Antioxidant Action of Vitamin C
Leucine Degradation I
Valine Degradation I
Glutaryl-CoA Degradation
Isoleucine Degradation I
Tryptophan Degradation III (Eukaryotic)
RhoGDI Signaling
Fatty Acid ß-oxidation I

Figure 11

Regulatory Networks Centered on Adenylyl Cyclase and Protein Kinase A Signaling.

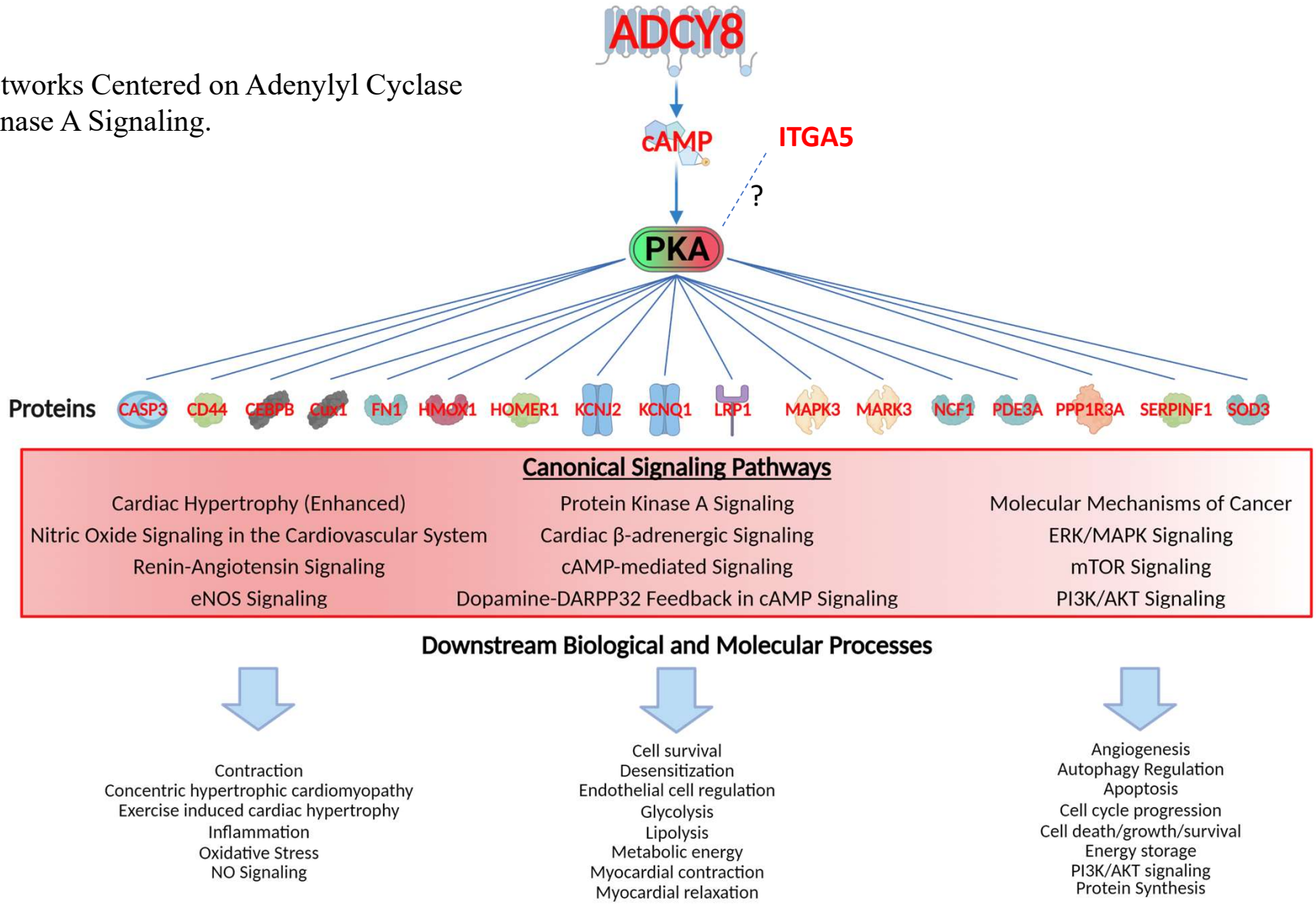

Figure 12

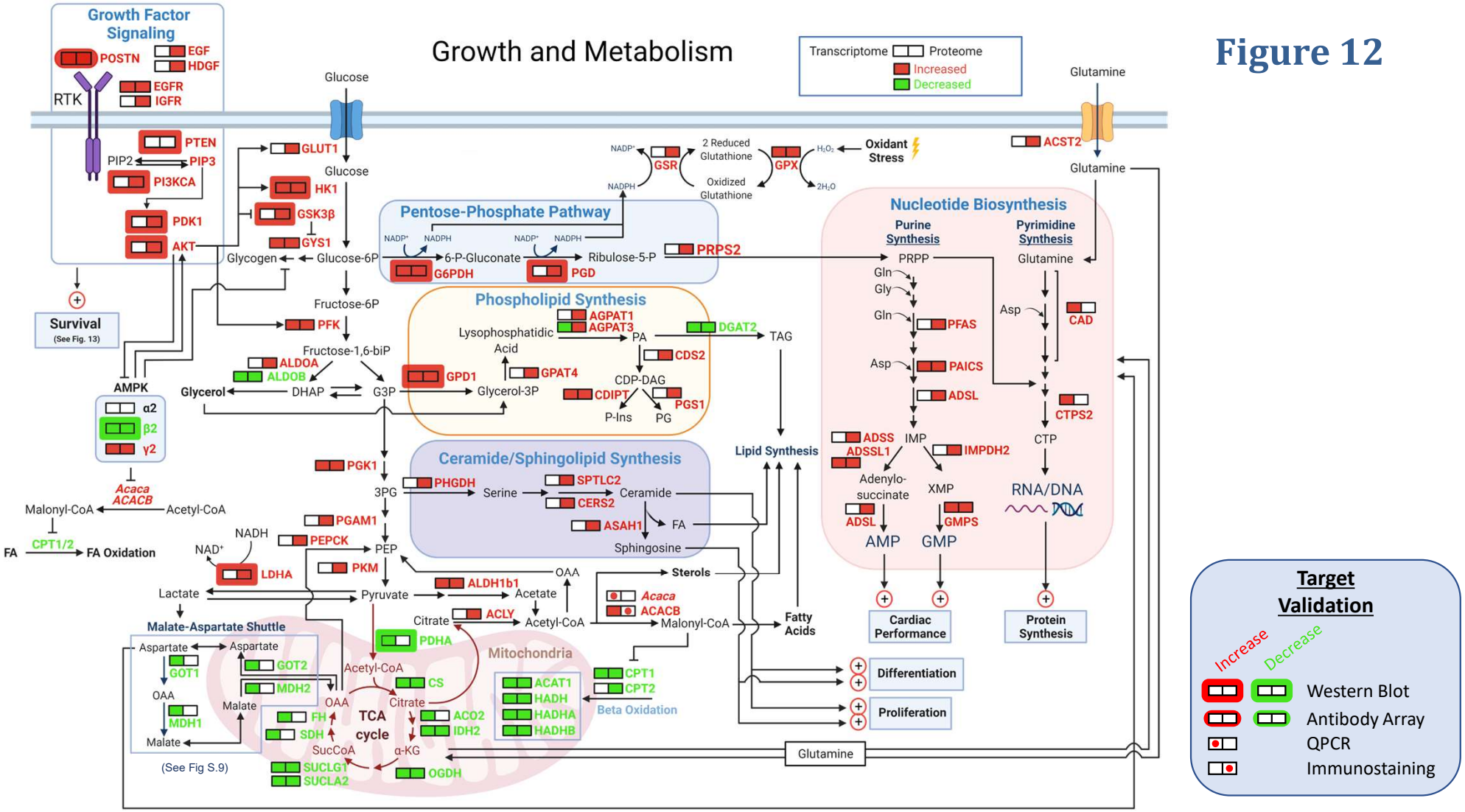

Created with BioRender.com

Figure 13

A Schematic of TG^{AC8} Heart Performance and Protection Circuits

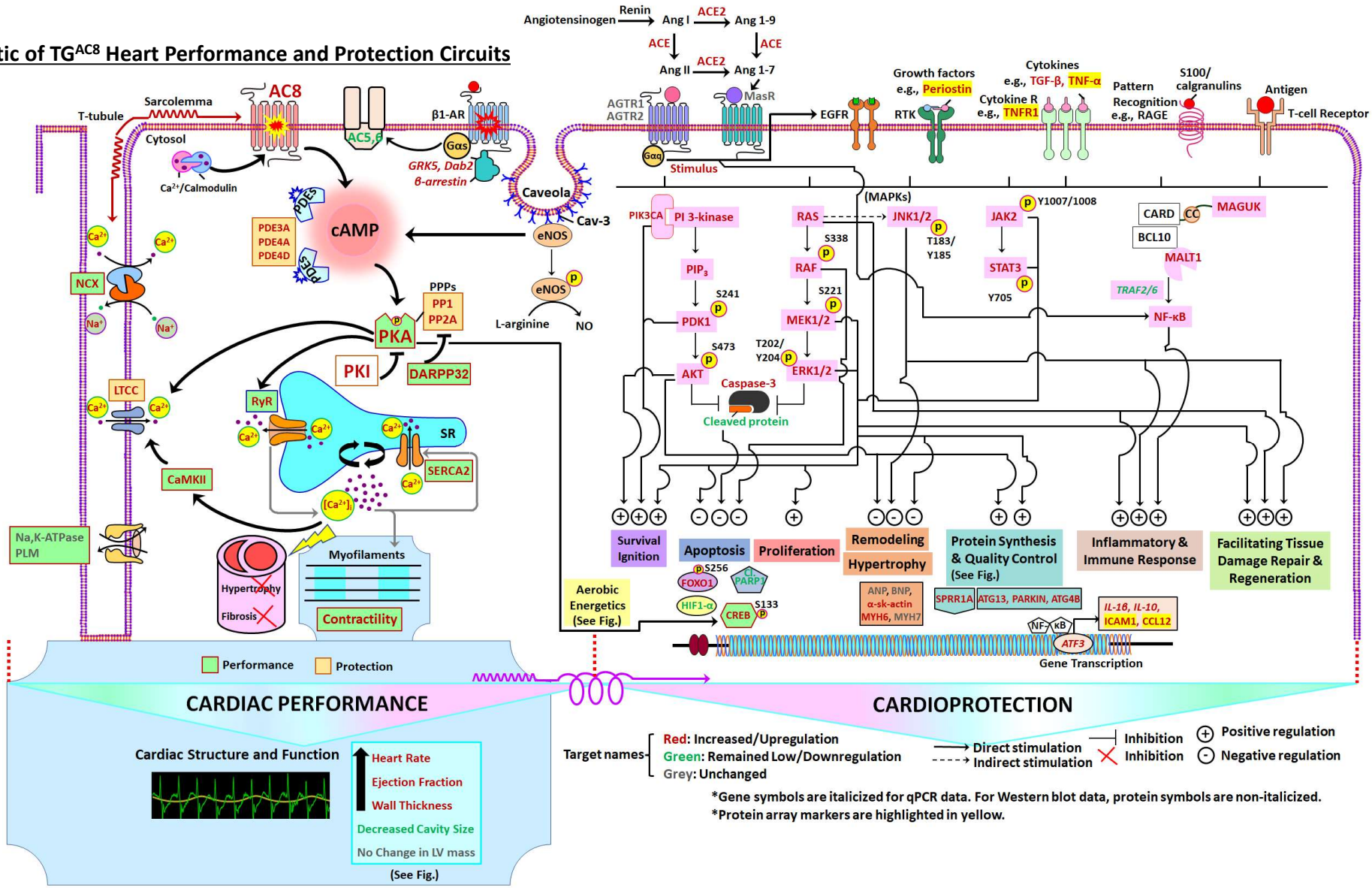

Supplemental Methods

A REMARKABLE ADAPTIVE PARADIGM OF HEART PERFORMANCE AND PROTECTION EMERGES IN RESPONSE TO THE CONSTITUTIVE CHALLENGE of MARKED CARDIAC-SPECIFIC OVEREXPRESSION OF ADENYLYL CYCLASE TYPE 8

Kirill V. Tarasov[1], Khalid Chakir[1], Daniel R. Riordon[1], Alexey E. Lyashkov[2], Ismayil Ahmet[1], Maria Grazia Perino[1], Allwin Jennifa Silvester[1], Jing Zhang[1], Mingyi Wang[1], Yevgeniya O. Lukyanenko[2], Jia-Hua Qu[1], Miguel Calvo-Rubio Barrera[2], Magdalena Juhaszova [1], Yelena S Tarasova[1], Bruce Ziman[1], Richard Telljohann[1], Vikas Kumar[1], Mark Ranek[3], John Lammons[1], Rostislav Beshkov[1], Rafael deCabo[2], Seungho Jun[3], Gizem Keceli[3], Ashish Gupta[3], Dongmei Yang[1], Miguel A. Aon[1], Luigi Adamo[3], Christopher H. Morrell[1], Walter Otu[1], Cameron Carroll[1], Shane Chambers[1], Nazareno Paolocci[3], Thanh Huynh[5], Karel Pacak[5], Robert G Weiss[3], Loren Field[4], Steven J. Sollott[1] and Edward G Lakatta[1]*.

[1] LABORATORY of CARDIOVASCULAR SCIENCE, [2]TRANSLATIONAL GERONTOLOGY BRANCH, INTRAMURAL RESEARCH PROGRAM, NATIONAL INSTITUTE ON AGING, NATIONAL INSTITUTES OF HEALTH, BALTIMORE, MARYLAND,
[3] DIVISION OF CARDIOLOGY, DEPARTMENT OF MEDICINE, JOHNS HOPKINS UNIVERSITY SCHOOL OF MEDICINE, BALTIMORE, MD 21205, USA

[4] KRAENNERT INSTITUTE OF CARDIOLOGY, INDIANNA UNIVERSITY SCHOOL OF MEDICINE, INDIANAPOLIS, INDIANA

[5] SECTION ON MEDICAL NEUROENDOCRINOLOGY, EUNICE KENNEDY SHRIVER NATIONAL INSTITUTE OF CHILD HEALTH AND HUMAN DEVELOPMENT, NIH, BETHESDA, MARYLAND, USA

Echocardiography

Mice underwent echocardiographic (Echo) examination (40-MHz transducer; Visual Sonics 3100; Fuji Film Inc, Seattle, WA) under light anesthesia with isoflurane (2% in oxygen) via nosecone, temperature was maintained at 37°C using a heating pad. Mice were placed in the supine position; skin hair in the chest area was shaved. Standard ECG electrodes were placed on the limbs and ECG Lead II was recorded simultaneously with acquisition of echo images. Each Echo examination was completed within 10 min. Parasternal long-axis views of the LV were obtained and recorded to ensure that mitral and aortic valves and the LV apex were visualized. From the parasternal long-axis view of the LV, M-mode tracings of LV were obtained at mid-papillary muscle level. M-mode tracing of Left atrium and basal aorta were recorded at aortic valve level and Left atrial dimension (LAD) and Aortic lumen dimension (AoD) were measured. Mitral valve blood flow velocity (E and A waves) was recorded at the tip of the mitral valves at an angle of 450. Parasternal short-axis views of the LV were recorded at the mid-papillary muscle level. Endocardial area tracings, using the leading-edge method, were performed in the 2D mode (short-axis and long-axis views) from digital images captured on a cine loop to calculate the end-diastolic and end-systolic LV areas. LV End-diastolic volume (EDV) and end-systolic volume (ESV) were calculated by a Hemisphere Cylinder Model method. Stroke volume (SV) was calculated as SV = EDV-ESV. Cardiac output (CO) was calculated as CO = SV*HR. Ejection Fraction (EF) was derived as EF = 100 * (EDV -ESV) / EDV. Cardiac Index (CI) was calculated as CI = CO / BW. LV Posterior Wall (PW) and Inter Ventricular Septal thicknesses (IVS) were measured from the LV M-mode tracing LV. LV mass (LVM) was calculated from EDV, IVS and PW. LV early (E) and late (A) diastolic filling rates, and early/late ratio (E/A) were calculated from mitral valve blood flow velocities.

48 All measurements were made by a single observer who was blinded to the identity of the tracings.
49 All measurements were reported an average of five consecutive cardiac cycles covering at least
50 one respiration cycle (100 times/min in average). The reproducibility of measurements was
51 assessed by repeated measurement a week apart in randomly selected images; the repeated-
52 measure variability was less than 5%.

53 Echocardiography data are expressed as mean ± SEM. Differences between two groups were
54 assessed by a t-test. Statistical significance was assumed at $p<0.05$.

55 Heart and cardiac tissue isolation.

56 Mice were injected (intraperitoneally) with heparin and acutely anesthetized with pentobarbital-
57 based euthanasia solution. The heart then was quickly removed and placed into cold PBS solution.
58 The left ventricle free wall, without the septum, was identified anatomically, under a dissecting
59 microscope, and pieces of tissue 2x3mm were dissected and snap frozen in liquid nitrogen.

60 LV Histology

61 The LV free wall, (excluding the septum) was cut into base, mid-portion, and apex segments, fixed
62 with formalin, embedded in paraffin, and sectioned (5 µm in thickness). Sections were stained with
63 hematoxylin and eosin, silver (Reticulum stain kit, American MasterTech Scientific, Inc, Lodi,
64 CA) and Masson's trichrome (American MasterTech Scientific, Inc, Lodi, CA) as previously
65 reported4. Myocyte cross-sectional area was measured from images captured from silver-stained
66 5-µm-thick sections of the LV mid portion sections as described5. Suitable cross sections were
67 defined as having nearly circular-to-oval myocytes at the nuclear level. Outlines of ~25 myocytes
68 were traced in each section. Morphometric Analyses were performed using the computerized
69 imaging program MetaMorph (MetaMorph Imaging System, Universal Imaging Corp) using light
70 microscopy.

71 ## EdU labeling for detection and Imaging of cardiac cell DNA synthesis.

72 Mice were administered 0.35mg/L 5-ethynyl-2'-deoxyuridine (EdU) for 28 days via drinking
73 water, changed every third day. Mice were then administered pentobarbital IP, heart removed and
74 placed in PBS. The aorta was cannulated, and the heart perfused with PBS for 5 min followed by
75 perfusion at ~100mmHg with 4% paraformaldehyde for approximately 10 min or until flow rate
76 was greatly reduced. Hearts were stored in fresh 4% formaldehyde for 24hr at 4 degrees. Hearts
77 were washed with phosphate buffer and imbedded in 4% low melting point agarose. Sequential
78 transverse sections from the heart of WT and TG^{AC8} transgenic mice were sectioned on the Leica
79 Vibratome VT1000s from 200u-300uM. Sections were permeabilized with 0.2% triton, glycine,
80 and 2% DMSO for 3 days. EDU labeling (Click Chemistry Tools), and primary antibodies
81 Vimentin 1:500 (Synaptic Systems), Actinin (Sigma) 1:500, WGA 1:500 (Vector Labs), 4′,6-
82 diamidino-2-phenylindole DAPI 1:300 (Sigma). Five microscopic fields, per mouse, in the left
83 ventricle were visualized in cardiomyocytes via fluorescent imaging (Zeiss LSM 980) at 400 x
84 magnification, and the number of cardiac nuclei staining positively for EdU was counted in each.

85 ## BRDU labeling

86 To monitor cardiomyocyte S-phase activity, TG^{AC8} mice were crossed with MHC-nLAC mice
87 (which express a nuclear-localized β-galactosidase reporter under the transcriptional regulation of
88 the mouse α-cardiac MHC promoter; these mice are useful to identify cardiomyocyte nuclei in
89 histologic sections) [1]. The resulting TG^{AC8}, MHC-nLAC double-transgenic mice and MHC-nLAC
90 single-transgenic mice were identified and sequestered. At 28-to-30 days of age, the mice were
91 administered BrdU via drinking water (0.5 mg/ml, changed every 2nd day) for a total of 12 days.
92 Hearts were then harvested, fixed (1% paraformaldehyde, 50 mM cacodylate, 0.665% NaCl, pH
93 7.3) for 24 hours at 4°C, cryopreserved (30% sucrose) for 24 hours at 4°C, embedded and

94 cryosectioned at 10 microns using standard methods.[2] Sections were subjected to antigen retrieval
95 (10 mM trisodium citrate, 0.05% Tween20, pH 6) for 30 min at 100°C, and non-specific signal
96 was then blocked using MOM blocking reagent (Vector Labs, Burlingame California) following
97 manufacture's recommendations. Sections were then processed for β-galactosidase (#A-11132,
98 Invitrogen Life Sciences, Grand Island New York) and BrdU (#11296736001, Roche, Indianapolis
99 Indiana) immune reactivity; signal was developed using Alexa 555 goat anti-rabbit for β-
100 galactosidase and Alexa 488 goat anti-mouse for BrdU (secondary antibodies were #A21429 and
101 #A1100, respectively, Invitrogen). Sections were counterstained with Hoechst 33342 (Sigma-
102 Aldrich, St. Louis Missouri, blue signal) and cover slipped. After processing, the sections were
103 imaged sequentially for the red, green and blue signals using Surveyor software (version 9.0.4.5,
104 Digital Imaging Systems Ltd., Buckinghamshire, UK) interfaced with a Leica DM5500 (Leica
105 AG, Wetzlar, Germany) microscope. The percentage of S-phase cardiomyocyte nuclei (as
106 evidenced by the overlay of red βGAL signal and green BrdU immune reactivity) was then
107 quantitated.

108 ## Electron Microscopy

109 Mice left ventricles were dissected and processed for transmission electron microscopy
110 visualization. Fixation for electron microscopy was performed using 2.5% glutaraldehyde in 0.1
111 M sodium cacodylate buffer, pH 7-7.4. Samples were post fixed in 1% osmium tetroxide for 1 h
112 at 4°C in the same buffer, dehydrated and then embedded in Embed 812 resin (Electron
113 Microscopy Sciences, Hatfield, PA) through a series of resin resin-propylene oxide gradients to
114 pure resin. Blocks were formed in fresh resin contained in silicon molds, and the resin was
115 polymerized for 48-72 h at 65°C. Blocks were trimmed and sectioned in an EM UC7
116 ultramicrotome (Leica Microsystems, Buffalo Grove, IL) to obtain both semi-thick (0.5-1 µm

117 width) and ultrathin (40-60 nm width) sections. Semi-thick sections were mounted on glass slides
118 and stained with 1% toluidine blue in a 1% borax aqueous solution for 2 min. Micrographs were
119 obtained using a Leica AXIO Imager light microscope with a Axiocam 512 color camera (Carl
120 Zeiss, White Plains, NY). Ultrathin sections were stained with uranyl acetate and lead citrate, and
121 then imaged on a FEI Tecnai G^2 12 Transmission Electron Microscope (TEM) with a Gatan
122 OneView 16 Megapixel Camera.

123 Electron microscopy image analysis.

124 Micrographs at ×1,200 and x2,900 magnification were obtained from randomly selected areas of
125 cardiomyocytes cytoplasm for illustration and quantitative analysis purposes of mitochondrial
126 population and lipid droplets quantification. We determined two stereological parameters: (a) Na,
127 which is the numerical profile density (number of figures of interest / µm2 of cell fraction), and
128 (b) volume density of figures of interest (Vv; i.e., the volume fraction of cardiomyocyte cytoplasm
129 occupied by figures of interest). Volume density was obtained following a point analysis using a
130 simple square lattice test system.[3] Stereological measurements were performed using ImageJ
131 software (NIH). Mitochondria were identified as electron dense double membrane organelles
132 vesicles with identifiable cristae. Damaged mitochondria presented swollen and disrupted
133 electron-"lighter" cristae. Lipid droplets were denoted as electron-light, not-limited by any
134 membrane vesicles with very clear and homogeneous content. For stereological analysis, only
135 micrographs depicting longitudinal sections of cardiomyocytes with visible sarcomeres were
136 utilized, and from each of these ten pictures were taken from four to six cells/fibers. From each
137 picture, mitochondria were counted and measured to determine the number and area, doing the
138 average of these metrics in each picture, and finally the average for each cell. With this procedure,
139 a total of ~500 mitochondria per animal were counted/measured.

140

141 ## Adenylyl Cyclase Activity in Cell Membranes of LV Tissue.

142 Pieces of left ventricular (LV) tissues from wild type and AC8-TG mice were frozen in liquid
143 nitrogen, homogenized with Bel-Art™ SP Scienceware™ liquid nitrogen-cooled Mini Mortar and
144 stored at -80°C till use in the AC assay. On the day of the assay, 1 ml of ice-cold Lysis buffer (LB)
145 was added to each sample (LB composition: 10 mM Tris, pH 7.6, 0.5 mM DTT, 1 mM EGTA, 0.2
146 mM IBMX and 0.33% PIC). Samples were sonicated on ice (3 x 15 sec at setting 2, with 15 sec of
147 rest between bursts). 1800 µl of lysates (combined from two mice) were used for membrane
148 isolation. To each such combined sample a Sample Separation Buffer (SSB, composition: 10 mM
149 Tris, pH 7.6, 0.5 mM DTT, 1 mM EGTA, and 0.01% PIC) was added to a total volume of 11 ml.
150 These samples were centrifuged for 10 min at 1,000xg to remove big clumps. Supernatants were
151 further centrifuged for 30 min at 48,254xg at 40C in the Ultra-Clear 14x89 mm ultracentrifuge
152 tubes filled almost to the top with SSB. Membrane proteins precipitated on the bottom of the tubes
153 were washed three times with SSB via ultracentrifugation in the same conditions. At the end of
154 the last wash the pure pellets were resuspended in 300 µl of the Sample Reaction Buffer (SRB,
155 composition: 70 mM Tris, pH 7.6, 0.5 mM DTT, 1 mM EGTA, 5 mM $MgCl^2$, 0.2 mM IBMX, and
156 0.33% PIC) via sonication (on ice, 3 sec x 10 bursts on setting 2, rest between bursts 15 sec).
157 Protein content in the membrane preparations was quantified using a Reducing Agent Compatible
158 Pierce® Microplate BCA Protein Assay Kit # 23252.

159 Purified LV membranes were further diluted with SRB to a 0.2 µg/µl protein concentration and
160 used in the AC reaction. For the AC activity detection reaction, Stock AC reaction media
161 (SACRM) was prepared: 70 mM Tris (pH 7.6), 0.5 mM DTT, 1 mM EGTA, 5 mM $MgCl^2$, 0.2
162 mM IBMX, 4 mM ATP, 20 mM Creatine Phosphate, and 240 U/ml Creatine phosphokinase. The

163 end AC reaction composition was: 70 mM Tris (pH 7.6), 0.5 mM DTT, 1 mM EGTA, 5 mM
164 MgCl2, 0.2 mM IBMX, 0.25% PIC, 1 mM ATP, 5 mM Creatine Phosphate, 60 U/ml Creatine
165 phosphokinase, 0.2% DMSO, and 0.15 µg/µl membrane proteins.

166 To proceed the reaction, to the tube, preheated to 35ºC with 25 µl of the SACRM, 75 µl of the
167 membrane sample was added. The AC reaction lasted for 5 min at 35ºC at 400 RPM, and was
168 stopped by immersion of the tube into a 100ºC steel shot for 5 min. Then tube was cooled down,
169 centrifuged for 5 min at 40ºC at 15,000xg, and the supernatant was used for cAMP measurement.
170 0 time samples were prepared the following way: first to the tubes 75 µl of membrane proteins
171 were added, then proteins were denatured for 5 min at 100ºC and cooled down, after that 25 µl of
172 the SACRM was added to the tubes, and they were immediately immersed into 100ºC steel shot
173 for 5 min. Then these 0 time samples were processed exactly the same way as other samples.

174 The cAMP concentration was quantified via a LANCE kit protocol (Lance cAMP384 kit 500
175 points, Perkin Elmer, AD0262) in 96-well OptiPlates (Perkin Elmer). 15 µl of the sample was used
176 in the LANCE assay in a total volume of 40 µl (including 5 µl of 2x cAMP antibodies and 20 µl
177 of the Detection Mix). 2x cAMP antibodies stock preparation: 40 µl of Ab stock, 107 µl of 7.5%
178 BSA, 1853 µl of Detection buffer. Preliminary experiments demonstrated that cAMP LANCE
179 standard curves depend a lot on the buffer in which they were prepared; because of that cAMP
180 standards were prepared in the same buffers that were used for samples (75% SRB, 25% SACRM),
181 they were heated, cooled down and centrifuged. Right before fluorescence detection, plates were
182 centrifuged for 2 min at 1000xg to remove bubbles from the wells and to increase accuracy of the
183 measurements. All measurements were done in triplicate and the average of the 3 taken as the
184 cAMP value of that sample. Three pairs of WT and three pairs of TG^{AC8} mice LV samples were
185 used in this experiment. Statistic – values as mean ± St Error.

186 ## Immunostaining of isolated intact mice ventricular myocytes for ADCY8, SPRR1A and
187 ACACB detection.

188 Immunolabeling was performed in freshly isolated LV mouse cells. Cells were plated on laminin
189 coated MatTek dishes for 1h, 4% paraformaldehyde for 10 minutes, washed 3 times with PBS, and
190 then permeabilized with 0.2 % Triton X-100 in PBS for 10 minutes at room temperature. The
191 plates were washed two more times with PBS and then incubated with 10% goat serum for 1 hour
192 to minimize nonspecific staining. Afterwards, samples were incubated at 4 °C overnight with
193 primary antibodies against SPRR1 (ab125374), ADCY8 (bs-3925R) and ACACB(sc-390344).
194 Cells were then washed 3 times with PBS and incubated with fluorescence-conjugated secondary
195 antibodies (1:1000) (Sigma, USA) for 45 min at 37 °C. Cell nuclei were labeled with DAPI (Sigma,
196 USA). Cells were visualized using a LSM 710 laser-scanning confocal microscope (Carl Zeiss)
197 and images were captured using the Carl Zeiss Zen software. Quantitative fluorescence image
198 analysis was performed with ImageJ software, according to the following protocol:
199 http://theolb.readthedocs.io/en/latest/imaging/measuring-cell-fluorescence-using-imagej.html.
200 Images of stained cells were transferred and analyzed with Image J software to calculate the basic
201 characteristics of each image, including Area, Mean Gray Value and Integrated Density. To
202 calculate the corrected total cell fluorescence (CTCF). Small areas of positively stained fluorescent
203 cells were selected using a free hand selection tool. A background reading was created by selecting
204 a negatively stained rectangular section near the analyzed cell. Total fluorescence per cell was
205 calculated in Excel with the following formula: CTCF = Integrated Density – (Area of selected
206 cell X Mean fluorescence of background readings)

207 ## Immunostaining of isolated intact mice ventricular myocytes for RyR2 detection.

208 Immunostaining was performed as previously described. Specifically, freshly isolated mice
209 ventricular myocytes from TG^{AC8} and WT control mice were fixed with 4% paraformaldehyde,

210 permeabilized with 1% Triton and incubated with blocking solution (1×PBS containing 2% IgG-
211 free BSA+ 5% goat serum+0.02% NaN3+0.2% Triton). Then, the cells were incubated with
212 primary antibody anti-total RyR (Santa Cruse, R128, 1:500) overnight. After several wash,
213 secondary Atto 647N-conjugated anti-mouse IgG (Sigma-Aldrich, 1:500) antibody was used, and
214 only secondary antibody was applied to negative controls, which displayed negligible
215 fluorescence. Confocal images of middle section were obtained via Zeiss LSM 510 (Carl Zeiss
216 Inc., Germany) using 633 nm laser to excite the fluorophore Atto 647N. The images were analyzed
217 using ImageJ software (1.8V, Wayne Rasband, National Institutes of Health). Please note that the
218 RyR2 immunolabeling in TG^{AC8} mice ventricular myocytes was saturated if using the same
219 sampling setting as WT controls. So, the sampling condition was adjusted when sampling
220 ventricular myocytes from TG^{AC8} mice, and the density was converted to the same setting as WT
221 control for comparison. [4]

222 ## Protein synthesis

223 Protein synthesis was assessed by SUnSET-Western Blot as previously described 6. Briefly, the
224 puromycin solution was prepared in PBS, sterilized by filtration, and a volume of 200µl was
225 injected in mice intraperitoneally, to achieve a final concentration of 0.04µmol/g of body mass.
226 After 30 minutes, mice were sacrificed, the LV was harvested and snap frozen in liquid nitrogen.
227 Protein extraction was performed using Precellys, quantified with BCA assay 25µg of total protein
228 were separated by SDS-PAGE; proteins were then transferred onto PVDF membrane and
229 incubated overnight in the anti-puromycin primary antibody (MABE343, Sigma-Aldrich, St.
230 Louis, MO). Visualization of puromycin-labelled bands was obtained using horseradish
231 peroxidase conjugated anti-mouse IgG Fc 2a secondary antibody (Jackson ImmunoResearch
232 Laboratories Inc., West Grove, PA, USA), using Pierce Super Signal ECL substrate kit (Pierce/

233 Thermo Scientific Rockford, IL). Chemiluminescence was captured with the Imager AI600 and
234 densitometry analysis was performed using ImageQuantTL software (both by GE, Boston, MA).
235 Total protein was used as control for protein loading.

236 Genotypic differences of protein synthesis were tested via an as unpaired t-test.

237 Proteosome activity assay

238 Flash frozen tissue was homogenized in ice-cold cytosolic extraction buffer (50 mM Tris-HCl pH
239 7.5, 250 mM Sucrose, 5 mM $MgCl_2$, 0.5 mM EDTA, and 1 mM DTT). A bicinchoninic acid (BCA)
240 assay (Pierce) was used to determine the protein concentrations. All samples were equally
241 concentrated in proteasome assay buffer (50 mM Tris-HCl pH 7.5, 40 mM KCl, 5 mM $MgCl_2$, and
242 1 mM DTT). Proteasome activity was determined in the presence of 28 µM ATP using the Suc-
243 LLVY-AMC (18 µM, Boston Biochem #S280) fluorogenic substrate with and without proteasome
244 inhibition (MG 132, 1 mM, Sigma). The plate was read at an excitation wavelength of 380 nm and
245 an emission wavelength of 469 nm using a Spectramax M5 (Molecular Devices). Activity was
246 calculated by subtracting the background (proteasome inhibited value) from the reading
247 (proteasome activated value).

248 Protein Aggregation Assays

249 Protein aggregates were measured using Proteostat (Enzo, ENZ-51023) following the
250 manufacturer's instructions. For this assay left ventricle myocardial lysate (Cell Signaling lysis
251 buffer) was obtained, protein concentration assayed (BCA assay [Pierce]). Ten µg of protein
252 loaded into a 96-well microplate and protein aggregates were analyzed using the Proteostat assay
253 kit (Enzo Life Sciences) following the manufacturer's instructions. Background readings were
254 subtracted from sample recordings and were normalized to wild-type values.

255 ## Quantibody® Mouse Inflammation and Periostin Arrays

256 Fresh LV tissue from 3 months old mice was homogenized and lysed in RIPA buffer (Sigma
257 Aldrich) supplemented with protease inhibitor (Roche Inc.) using a Precellys homogenizer with
258 the CKMix Tissue Homogenizing Kit. The supernatant was collected after centrifugation at
259 10,000×g for 10 min at 4 °C. The protein concentration was determined using the Bicinchoninic
260 Acid (BCA) Assay (Thermo Fisher Scientific). The assay was performed using the Quantibody®
261 Mouse Inflammation Array kit (QAM-INF-1-1, RayBiotech Inc.). The samples (tissue lysates)
262 were diluted 2x using the sample diluent. 100 ul of both samples and standards were loaded on to
263 the glass slide (labelled with the 40 different cytokines and chemokines) and incubated for 2 hours
264 at room temperature. Samples and standards were decanted and from each well and washed with
265 150 µl of 1X Wash Buffer I at room temperature. The detection antibody cocktail was added to
266 each well and incubated at room temperature for 1 hour. The samples were decantyed and washed
267 with 150 µl of 1X Wash Buffer I at room temperature. A Cy3 equivalent dye-conjugated
268 streptavidin was added to each well and incubated in dark at room temperature for 1 hour. The
269 samples were decanted from each well, washed with 1x wash buffer and dried. The slide was
270 visualised for signals using a laser scanner equipped with a Cy3 wavelength (green channel). The
271 data was extracted, computed in the standard format as provided by the company and analyzed for
272 relative levels of different cytokines in both WT and TG^{AC8} mice. Periostin was assessed in an
273 array-based ELISA system (Growth Factor Quantibody Array, RayBiotech Life, Inc., Peachtree
274 Corners, GA). Briefly, after a blocking step, 100uL of LV-tissue lysates were added on a slide
275 containing a periostin antibody, and incubated 4C overnight. Nonspecific proteins were then
276 washed off, and the arrays incubated with a cocktail of biotinylated detection antibodies, followed
277 by a streptavidin-conjugated fluorophore. Signals were visualized using a fluorescence laser

278 scanner. Relative quantification was calculated using the median, after subtracting the background
279 intensity.

280 PKA Activity

281 Enzymatic activity assays with heart tissue lysates were performed for cAMP-dependent protein
282 kinase (PKA) using the PKA Kinase Activity Assay Kit (Abcam, ab139435), in accordance with
283 the manufacturer's instructions. The units are expressed in OD/mg protein/min.

284 Western Blotting

285 Snap-frozen left ventricle (LV) tissue from 3 month old mice was homogenized and lysed in ice
286 cold RIPA buffer (Thermo Fisher Scientific: 25 mM Tris-HCl (pH 7.6), 150 mM NaCl, 1% NP-
287 40, 1% sodium deoxycholate, 0.1% SDS) supplemented with a Halt protease inhibitor cocktail
288 (Thermo Fisher Scientific), Halt phosphatase inhibitor cocktail (Thermo Fisher Scientific) and
289 1 mM phenylmethyl sulfonyl fluoride, using a Precellys homogenizer (Bertin Instruments) with
290 tissue homogenization kit CKMix (Bertin Instruments) at 4 °C. Extracts were then centrifuged at
291 10,000×g for 10 min at 4 °C and the protein concentration of the soluble fraction determined using
292 the Bicinchoninic Acid (BCA) Assay (Thermo Fisher Scientific). Samples were denatured in
293 Laemmli sample buffer (BioRad Laboratories) containing 355 mM 2-mercaptoethanol at 95oC for
294 5 minutes, and proteins (10-50 µg/lane) resolved on 4-20% Criterion™ TGX Stain Free™ gels
295 (Bio-Rad Laboratories) by SDS/PAGE. Gels then exposed to UV transillumination for 2.5 minutes
296 to induce crosslinking of Stain Free™ gel trihalo compound with protein tryptophan residues.
297 Proteins were then transferred to low fluorescence polyvinylidene difluoride (LF-PVDF)
298 membranes (BioRad Laboratories) using an electrophoretic transfer cell (Mini Trans-Blot, Bio-
299 Rad). Membrane total protein was visualized using an Amersham Imager 600 (AI600) (GE
300 Healthcare Life Sciences) with UV transillumination to induce and a capture fluorescence signal.

301 Blocked membranes (5% milk/tris-buffered saline with Tween-20, TBST) were incubated with the
302 following primary antibodies: anti-MYH6 (MA5-27820) at 1:2,500 working concentration, anti-
303 ANP (PA5-29559) at 1:1,000, and anti-BNP (PA5-96084) at 1:1,000 from ThermoFisher
304 Scientific; anti-MYH7 (ab173366) at 1:500, anti-α-Sk. Actin (ab179467) at 1:1,000, and anti-
305 SERCA2 ATPase (ab91032) at 1:2000 from Abcam. Primary antibodies were then detected using
306 horseradish peroxidase (HRP) conjugated antibody (Invitrogen) at 1:10,000. Bands were
307 visualized using Pierce SuperSignal™ West Pico Plus ECL substrate kits (Thermo Scientific), the
308 signal captured using an Amersham Imager 600 (AI600) (GE Healthcare Life Sciences) and
309 quantified using ImageQuant TL software (GE Healthcare Life Sciences). Band density was
310 normalized to total protein.

311 RT-qPCR

312 RT-qPCR of LV tissue was performed to determine the transcript abundance of human AC8, genes
313 that mediate neural autonomic input to LV (n=4 WT and 4 TG^{AC8} mice) and to detect genes
314 regulating cytokines level in the heart (n=6 in WT and TG^{AC8}). RNA was extracted from left
315 ventricular myocytes (VM) with RNeasy Mini Kit (Qiagen, Valencia, CA) and DNAse on column
316 digestion. The cDNA was prepared using MMLV reverse transcriptase (Promega). RT-qPCR was
317 performed using a QuantStudio 6 Flex Real-Time PCR System (Thermo Fisher Scientific) with a
318 384-well platform. The reaction was performed with a FastStart Universal SYBR Green Master
319 Kit with Rox (Roche) using the manufacturer's recommended conditions; the sizes of amplicons
320 were verified. Each well contained 0.5 µl of cDNA solution and 10 µl of reaction mixture. Each
321 sample was quadruplicated and repeated twice using de novo synthesized cDNA sets. Preliminary
322 reactions were performed to determine the efficiency of amplification. RT-qPCR analysis was

323 performed using the ddCt method. Primers were selected with Primer Express 3.0 software
324 (Applied Biosystems). Full list of primers used for amplification provided in **Table S.12.**

325 RNASEQ

326 LV RNA was extracted from 8 of TGAC8 and WT animals. Following a quality control check,
327 RNA was processed with a SMARTer Stranded Total RNA-Seq Kit - Pico Input Mammalian
328 (Takara Bio USA, Inc.). 75 bp single end reads generated 30 to 40 million reads per library. Raw
329 RNA sequencing (RNASeq) reads were aligned and after quality trimming was mapped to the
330 UCSC mm10 mouse reference genome and cDNA of human AC8 and assembled using Tophat
331 v2.0 to generate BAM files for each sample. Cufflinks v.2.1.1 was used to calculate FPKM
332 (Fragments per Kilobase of transcript per Million mapped reads) for each sample. Differential
333 gene expression analysis was performed with a Cuffdiff package (Cufflinks v2.1.1)

334 LV Proteome analysis.

335 Four LV samples from WT and TG^{AC8} mouse hearts were snap frozen in liquid nitrogen and stored
336 at -80°C. On average, 2 mg of muscle tissue from each sample was pulverized in liquid nitrogen
337 and mixed with a lysis buffer containing (4% SDS, 1% Triton X-114, 50 mM Tris, 150mM NaCl,
338 protease inhibitor cocktail (Sigma), pH 7.6. Samples were sonicated on ice using a tip sonicator
339 for 1 min with 3 sec pulses and 15 sec rest periods at 40% power. Lysates were centrifuged at
340 +4°C for 15 min at 14000 rpm, aliquoted and stored at -80°C until further processing. Protein
341 concentration was determined using commercially available 2-D quant kit (GE Healthcare Life
342 Sciences). Sample quality was confirmed using NuPAGE® protein gels stained with fluorescent
343 SyproRuby protein stain (Thermo Fisher).

344 In order to remove detergents and lipids 500 µg of muscle tissue lysate was precipitated using a
345 methanol/chloroform extraction protocol (sample:methanol:chloroform:water – 1:4:1:3).[5] Proteins

346 were resuspended in 50 ul of concentrated urea buffer (8M Urea, 150 mM NaCl (Sigma)), reduced
347 with 50 mM DTT for 1 hour at 36°C and alkylated with 100 mM iodoacetamide for 1 hour at 36°C
348 in the dark. The concentrated urea/protein mixture was diluted 12 times with 50 mM ammonium
349 bicarbonate buffer, and proteins were digested for 18 hours at 36°C, using trypsin/LysC mixture
350 (Promega) in 1:50 (w/w) enzyme to protein ratio. Protein digests were desalted on 10 x 4.0 mm
351 C18 cartridge (Restek, cat# 917450210) using Agilent 1260 Bio-inert HPLC system with a fraction
352 collector. Purified peptides were speed vacuum dried and stored at -80°C until further processing.

353 A subset of 8 muscle samples (100 µg) each corresponding to 4 controls and 4 TGAC8 LVs and
354 one averaged reference sample were labeled with 10-plex tandem mass spectrometry tags (TMT)
355 using standard TMT labeling protocol (Thermo Fisher). 200 femtomole of bacterial beta-
356 galactosidase digest (SCIEX) was spiked into each sample prior to TMT labeling to control for
357 labeling efficiency and overall instrument performance. Labeled peptides from 10 different TMT
358 channels were combined into one experiment and fractionated.

359 High-pH RPLC fractionation and concatenation strategy

360 High-pH RPLC fractionation was performed in an Agilent 1260 bio-inert HPLC system using a
361 3.9 mm X 5 mm XBridge BEH Shield RP18 XP VanGuard cartridge and a 4.6 mm X 250 mm
362 XBridge Peptide BEH C18 column (Waters). The solvent contained 10mM ammonium formate
363 (pH 10) as mobile phase (A), and 10mM ammonium format and 90% ACN (pH 10) as mobile-
364 phase B 9.

365 TMT labeled peptides prepared from the ventricular muscle tissues were separated using a linear
366 organic gradient from 5% to 50% B over 100 min. Initially, 99 fractions were collected at 1 min
367 intervals. Three individual high-pH fractions were concatenated into 33 master fractions at 33 min
368 intervals between fractions (fraction 1, 34, 67 = master fraction 1, fraction 2, 35, 68 = master

369 fraction 2 and so on). Combined fractions were speed vacuum dried, desalted and stored at -80°C
370 until final LC-MS/MS analysis.

371 ## Capillary nano-LC-MS/MS analyses

372 Purified peptide fractions were analyzed using UltiMate 3000 Nano LC Systems coupled to the Q
373 Executive HF Orbitrap mass spectrometer (Thermo Scientific, San Jose, CA). Each fraction was
374 separated on a 35 cm capillary column (3µm C18 silica, Hamilton, HxSil cat# 79139) with 200
375 µm ID on a linear organic gradient at a 500 nl/min flow rate. Gradient applied from 5 to 35 % in
376 205 min. Mobile phases A and B consisted of 0.1% formic acid in water and 0.1% formic acid in
377 acetonitrile, respectively. Tandem mass spectra were obtained using Q Exactive HF mass
378 spectrometer with a heated capillary temperature +280°C and spray voltage set to 2.5 kV. Full
379 MS1 spectra were acquired from 300 to 1500 m/z at 120000 resolution and 40 ms maximum
380 accumulation time with automatic gain control [AGC] set to $3x10^6$. Dd-MS2 spectra were acquired
381 using a dynamic m/z range with fixed first mass of 100 m/z. MS/MS spectra were resolved to
382 30000 within of a maximum accumulation time, 120 ms with AGC target set to $2x10^5$. Twelve
383 most abundant ions were selected for fragmentation using 28% normalized high collision energy.
384 A dynamic exclusion time of 45 sec. was used to discriminate against the previously analyzed ions.

385 ## Bioinformatics Analysis of the LV Proteome

386 Acquired raw data files from Q Exactive HF were converted to mascot generic format (MGF)
387 using MSConvert, an open source software developed by ProteoWizard
388 (http://proteowizard.sourceforge.net). Conversion filters were specified as follows: at MS level 1
389 with activation:HCD, threshold:count 900 most-intense, zeroSamples:remove Extra 1-,
390 peakPicking;true 1-. Produced MGF files were searched in Mascot against the SWISS-PROT
391 mouse database (02/06/2017) with the following parameters: enzyme trypsin/P, 2 missed

392 cleavages, MS1 tolerance 20 ppm, MS2 tolerance 0.08 Da, quantification TMT10plex. Variable
393 modifications were set to methionine oxidation, carbamidomethylation of cysteines, deamidation
394 at glutamine and asparagine, carbamylation of lysin. Searched mascot data files were processed
395 using commercially available Scaffold Q+ software package (Proteome Software, Inc). Files were
396 merged in to one summary file using MudPIT algorithm, and researched against SWISS-PROT
397 mouse database (02/06/2017), using XTandem search engine for deeper protein coverage with
398 both protein prophet scoring algorithm and protein clustering analysis turned on. Raw reporter ion
399 intensities from unique peptides were extracted into excel file and used in the final analysis.

400 Minor variations in protein amounts between TMT channels was adjusted by calculating a ratio
401 between signal intensity in each TMT channel (In). Adjusted intensity for each channel (Incorr)
402 was calculated by taking a sum of all intensities in each TMT channel divided by the average (μ)
403 of all calculated sum intensities and multiplied by the initial intensity in each TMT cannel for each
404 peptide: $(\sum I126+\sum I127+\sum I128+\sum I129+\sum I130+\sum I131)/6=\mu$; $\sum In/\mu*In=Incorr$.

405 Fold change for each unique peptide in each experiment was calculated by dividing Incorr by the
406 median of all intensities in all TMT channels. The fold change between genotypes for each
407 expressed protein was calculated by taking a median of fold change for all unique peptides of a
408 given protein detected by mass spectrometry. Genotype differences were compared via Student's
409 t-test. A P value < 0.05 was considered to be significant.

410

411 ## MR spectroscopy High Energy Phosphate

412 In vivo MRI/MRS experiments were performed on a Bruker spectrometer equipped with a 4.7-
413 T/40-cm Oxford magnet and actively shielded gradients. A one-dimensional 31P chemical shift
414 imaging (1D-CSI) sequence was used to obtain high-energy phosphate data, as previously

415 described. [6] The PCr and [β-P] ATP peaks in 31P MR localized spectra were quantified by
416 integration of the peak areas. [6]

417 ## ROS measurements

418 ROS measurements were conducted using electron paramagnetic resonance (EPR) spectroscopy
419 as previously described.[7] Snap-frozen heart tissue (apex, ~20 mg) was homogenized in phosphate-
420 buffered saline (PBS) containing protease inhibitor cocktail (Roche Applied Science, Indianapolis,
421 IN) and 0.1 mM of the metal chelator, diethylenetriaminepentaacetic acid (DTPA), at pH 7.4.
422 Nonsoluble fractions were removed by centrifugation at 15,000 g for 10 min (4ºC). The
423 homogenates were kept on ice and analyzed immediately. Stock solutions of 1-hydroxy-3-
424 methoxycarbonyl-2,2,5,5-tetramethyl-pyrrolidine hydrochloride (CMH; Enzo Life Sciences,
425 Farmingdale, NY) were prepared daily in nitrogen purged 0.9% (w/v) NaCl, 25 g/L Chelex 100
426 (Bio-Rad) and 0.1 mM DTPA, and kept on ice. The samples were treated with 1 mM CMH at 37
427 oC for 2 min, transferred to 50-µl glass capillary tubes, and analyzed immediately on a Bruker E-
428 Scan (Billerica, MA) EPR spectrometer at room temperature. Spectrometer settings were as
429 follows: sweep width, 100 G; microwave frequency, 9.75 GHz; modulation amplitude, 1 G;
430 conversion time, 5.12 ms; receiver gain, 2 x 103; number of scans, 16. EPR signal intensities were
431 normalized with respect to the protein concentrations of the tissue homogenates as determined by
432 Pierce BCA protein assay kit (Life Technologies).

433

434 ## Determination of mPTP-ROS Threshold.

435 Experiments were conducted as described previously,[8] using a method to quantify the ROS
436 susceptibility for the induction of mPTP in individual mitochondria within cardiac myocytes. [9]

437 Briefly, isolated cardiomyocytes were resuspended in HEPES buffer: 137 mM NaCl, 4.9 mM KCl,
438 1.2 mM $MgSO_4$, 1.2 mM NaH_2PO_4, 15 mM glucose, 20 mM HEPES, and 1.0 mM $CaCl_2$ (pH to
439 7.3). To assess the susceptibility of the mPTP to induction by ROS, cells were loaded with 100
440 nM tetramethylrhodamine methyl ester (TMRM; Invitrogen I34361) for at least 2 h at room
441 temperature. Cells were imaged with an LSM-510 inverted confocal microscope, using a Zeiss
442 Plan-Apochromat 63×/1.4 numerical aperture oil immersion objective (Carl Zeiss Inc., Jena,
443 Germany) with the optical slice set to 1 µm. Images were processed by MetaMorph software
444 (Molecular Devices, San Jose, CA). Line scan images at 2 Hz were recorded from ~22
445 mitochondria arrayed along individual myofibrils with excitation at 543 nm and collecting
446 emission at >560 nm, and the confocal pinhole was set to obtain spatial resolutions of 0.4 µm in
447 the horizontal plane and 1 µm in the axial dimension. Repetitive laser scanning of this row of
448 mitochondria in a myocyte loaded with TMRM results in incremental, additive exposure of only
449 the laser-exposed area to the photodynamic production of ROS and consequent mPTP induction.
450 The occurrence of mPTP induction is clearly identified by the immediate dissipation of $\Delta\Psi$ in
451 individual mitochondria and is seen at the point in time where "columns" of the line scan image
452 suddenly lose TMRM fluorescence intensity and become black (Fig.6). The ROS threshold for
453 mPTP induction (tmPTP) was determined as the average time necessary to induce mPTP in the
454 exposed row mitochondria (N=3 in each genotype) (Fig. 6 M,N).

455 ### Determination of autophagolysosome accumulation

456 Cardiomyocytes were loaded with the autophagy dye from CYTO-ID Autophagy detection kit
457 (ENZO 51031-K200), according the manufacturer protocol (dilution 1:500 in HEPES buffer) and
458 incubated for 30 minutes at room temperature. Then the dye was washed out by HEPES buffer and
459 cell imaged with a confocal microscope (see above) in frame mode using 488 nm excitation and

460 >505 nm emission filter. Images were processed by MetaMorph software. To discriminate the
461 fluorescent spots representing autophagolysosomes from background and to ensure that all staining
462 analyzed was only the true positive labelling, a defined threshold value was set for 488 nm excited
463 fluorescence pixel intensity. The area of cell occupied by autophagolysosomes was expressed as
464 fraction of total cell area. [10]

465 ## References

466 1. Soonpaa MH, Koh GY, Klug MG and Field LJ. Formation of nascent intercalated disks
467 between grafted fetal cardiomyocytes and host myocardium. *Science*. 1994;264:98-101.

468 2. Junqueira LCU CJ, Kelley RO. *Basic histology*. Norwalk, Conn.: Appleton & Lange; 1992.

469 3. Weibel ER. *Stereological methods. Practical methods for biological morphometry.*
470 London: Academic Press; 1979.

471 4. Yang D, Lyashkov AE, Li Y, Ziman BD and Lakatta EG. RGS2 overexpression or G(i)
472 inhibition rescues the impaired PKA signaling and slow AP firing of cultured adult rabbit
473 pacemaker cells. *J Mol Cell Cardiol*. 2012;53:687-94.

474 5. Wessel D and Flugge UI. A method for the quantitative recovery of protein in dilute
475 solution in the presence of detergents and lipids. *Anal Biochem*. 1984;138:141-3.

476 6. Gupta A, Akki A, Wang Y, Leppo MK, Chacko VP, Foster DB, Caceres V, Shi S, Kirk
477 JA, Su J, Lai S, Paolocci N, Steenbergen C, Gerstenblith G and Weiss RG. Creatine kinase-
478 mediated improvement of function in failing mouse hearts provides causal evidence the failing
479 heart is energy starved. *J Clin Invest*. 2012;122:291-302.

480 7. Chelko SP, Keceli G, Carpi A, Doti N, Agrimi J, Asimaki A, Beti CB, Miyamoto M, Amat-
481 Codina N, Bedja D, Wei AC, Murray B, Tichnell C, Kwon C, Calkins H, James CA, O'Rourke B,
482 Halushka MK, Melloni E, Saffitz JE, Judge DP, Ruvo M, Kitsis RN, Andersen P, Di Lisa F and
483 Paolocci N. Exercise triggers CAPN1-mediated AIF truncation, inducing myocyte cell death in
484 arrhythmogenic cardiomyopathy. *Sci Transl Med*. 2021;13.

485 8. Juhaszova M, Zorov DB, Kim SH, Pepe S, Fu Q, Fishbein KW, Ziman BD, Wang S,
486 Ytrehus K, Antos CL, Olson EN and Sollott SJ. Glycogen synthase kinase-3beta mediates
487 convergence of protection signaling to inhibit the mitochondrial permeability transition pore. *J*
488 *Clin Invest*. 2004;113:1535-49.

489 9. Zorov DB, Filburn CR, Klotz LO, Zweier JL and Sollott SJ. Reactive oxygen species
490 (ROS)-induced ROS release: a new phenomenon accompanying induction of the mitochondrial
491 permeability transition in cardiac myocytes. *J Exp Med*. 2000;192:1001-14.

492 10. Aon MA, Cortassa S, Juhaszova M, Gonzalez-Reyes JA, Calvo-Rubio M, Villalba JM,
493 Lachance AD, Ziman BD, Mitchell SJ, Murt KN, Axsom JEC, Alfaras I, Britton SL, Koch LG, de
494 Cabo R, Lakatta EG and Sollott SJ. Mitochondrial health is enhanced in rats with higher vs. lower
495 intrinsic exercise capacity and extended lifespan. *NPJ Aging Mech Dis*. 2021;7:1.

496

Supplemental Figures

A REMARKABLE ADAPTIVE PARADIGM OF HEART PERFORMANCE AND PROTECTION EMERGES IN RESPONSE TO THE CONSTITUTIVE CHALLENGE of MARKED CARDIAC-SPECIFIC OVEREXPRESSION OF ADENYLYL CYCLASE TYPE 8

Kirill V. Tarasov[1], Khalid Chakir[1], Daniel R. Riordon[1], Alexey E. Lyashkov[2], Ismayil Ahmet[1], Maria Grazia Perino[1], Allwin Jennifa Silvester[1], Jing Zhang[1], Mingyi Wang[1], Yevgeniya O. Lukyanenko[2], Jia-Hua Qu[1], Miguel Calvo-Rubio Barrera[2], Magdalena Juhaszova [1], Yelena S Tarasova[1], Bruce Ziman[1], Richard Telljohann[1], Vikas Kumar[1], Mark Ranek[3], John Lammons[1], Rostislav Beshkov[1], Rafael deCabo[2], Seungho Jun[3], Gizem Keceli[3], Ashish Gupta[3], Dongmei Yang[1], Miguel A. Aon[1], Luigi Adamo[3], Christopher H. Morrell[1], Walter Otu[1], Cameron Carroll[1], Shane Chambers[1], Nazareno Paolocci[3], Thanh Huynh[5], Karel Pacak[5], Robert G Weiss[3], Loren Field[4], Steven J. Sollott[1] and Edward G Lakatta[1]*.

[1] LABORATORY of CARDIOVASCULAR SCIENCE, [2]TRANSLATIONAL GERONTOLOGY BRANCH, INTRAMURAL RESEARCH PROGRAM, NATIONAL INSTITUTE ON AGING, NATIONAL INSTITUTES OF HEALTH, BALTIMORE, MARYLAND,
[3] DIVISION OF CARDIOLOGY, DEPARTMENT OF MEDICINE, JOHNS HOPKINS UNIVERSITY SCHOOL OF MEDICINE, BALTIMORE, MD 21205, USA

[4] KRAENNERT INSTITUTE OF CARDIOLOGY, INDIANNA UNIVERSITY SCHOOL OF MEDICINE, INDIANAPOLIS, INDIANA

[5] SECTION ON MEDICAL NEUROENDOCRINOLOGY, EUNICE KENNEDY SHRIVER NATIONAL INSTITUTE OF CHILD HEALTH AND HUMAN DEVELOPMENT, NIH, BETHESDA, MARYLAND, USA

Figure S.1 Representative images of Echocardiograms of TG^{AC8} and WT LV.

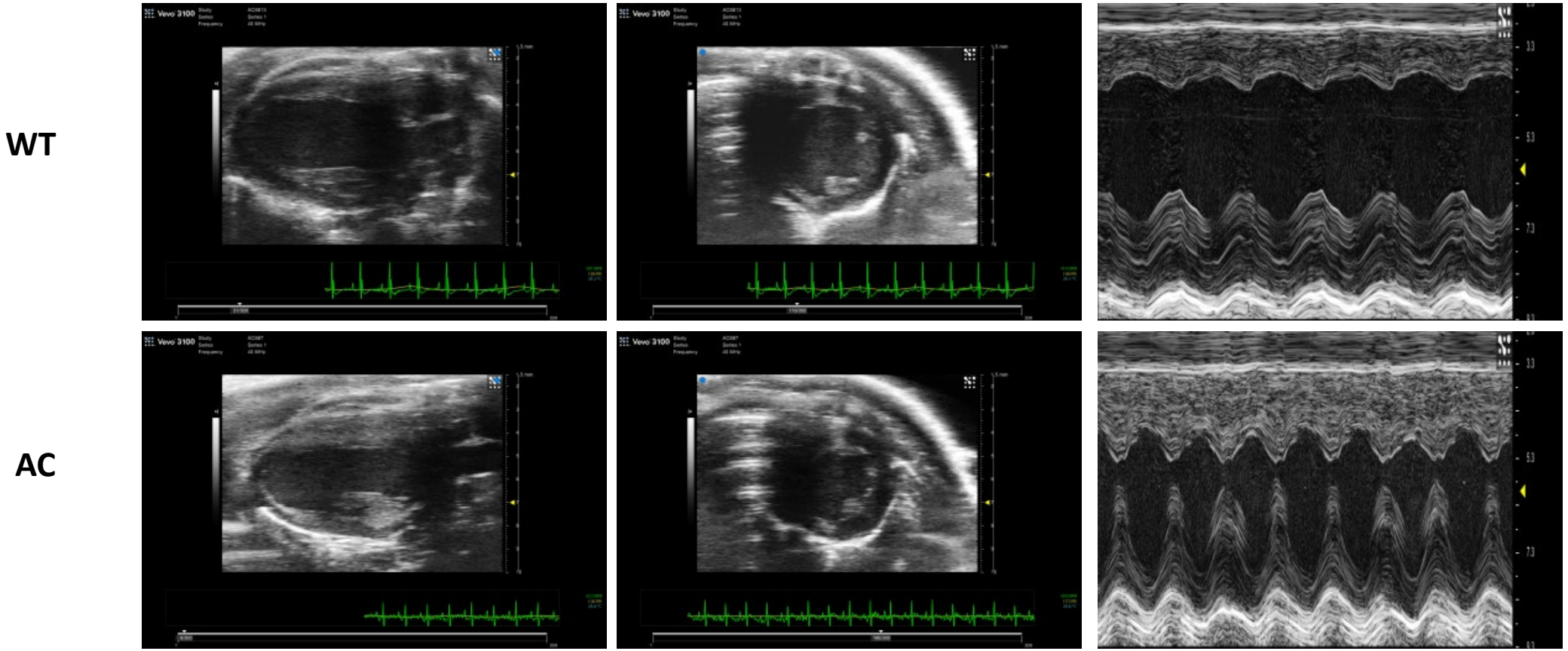

Figure S.2 Representative LV sections, labeled with picrosirius red (A) and (B) average collagen density (picrosirius red labeling) in TG^{AC8} vs WT LV.

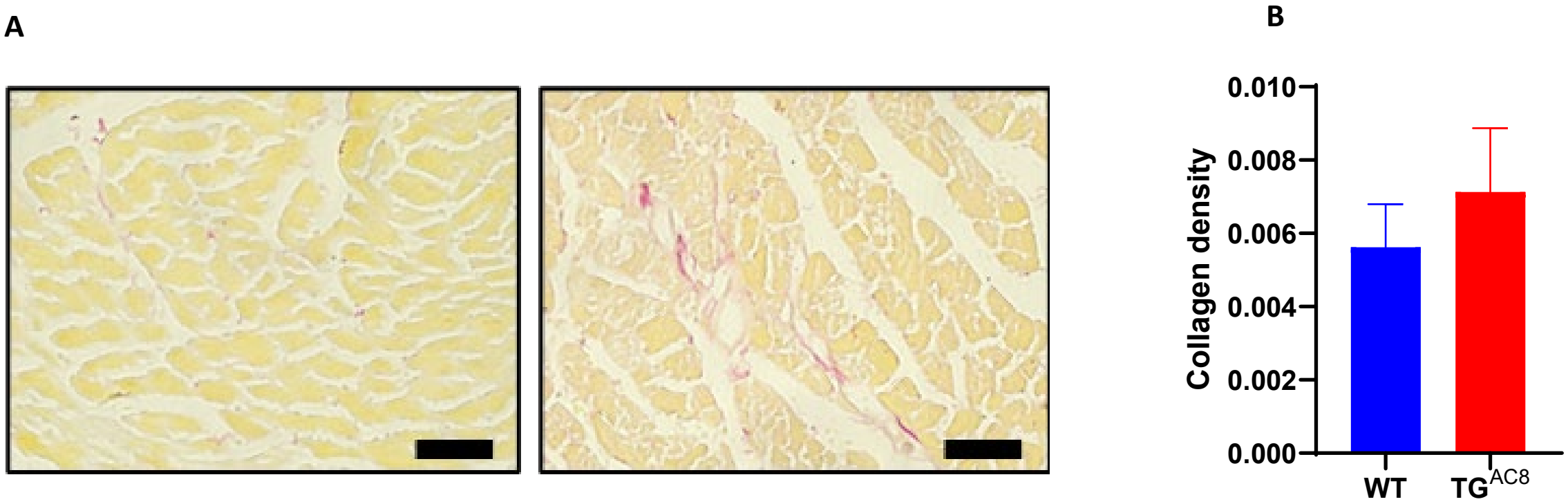

Figure S.3 (A) Pathway for catecholamine synthesis and breakdown; (B) Myocardial catecholamine levels.

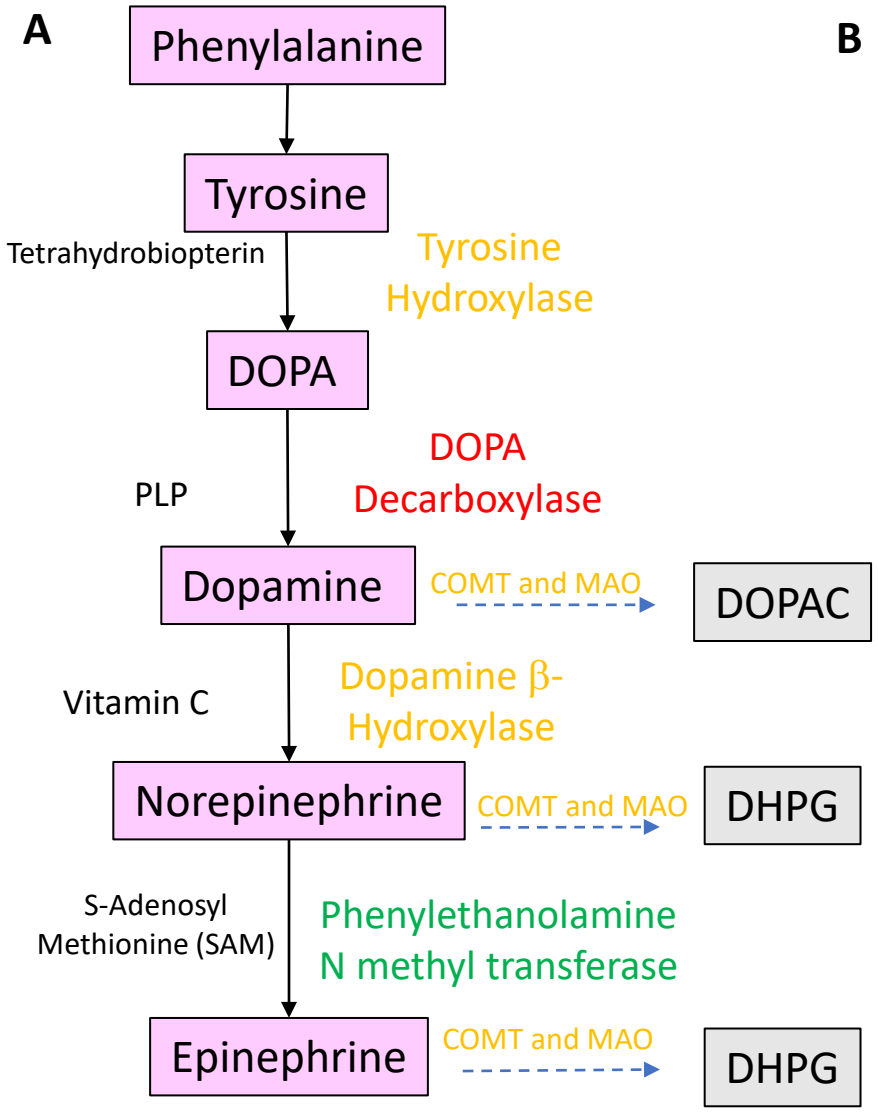

LV Proteomics:
RED – Upregulated
Yellow- No Change
Green- Downregulated

DOPAC: dihydroxyphenylacetic acid
DHPG: dihydroxyphenylglycol
COMT: catechol O-methyltransferase
MAO: monoamine oxidase

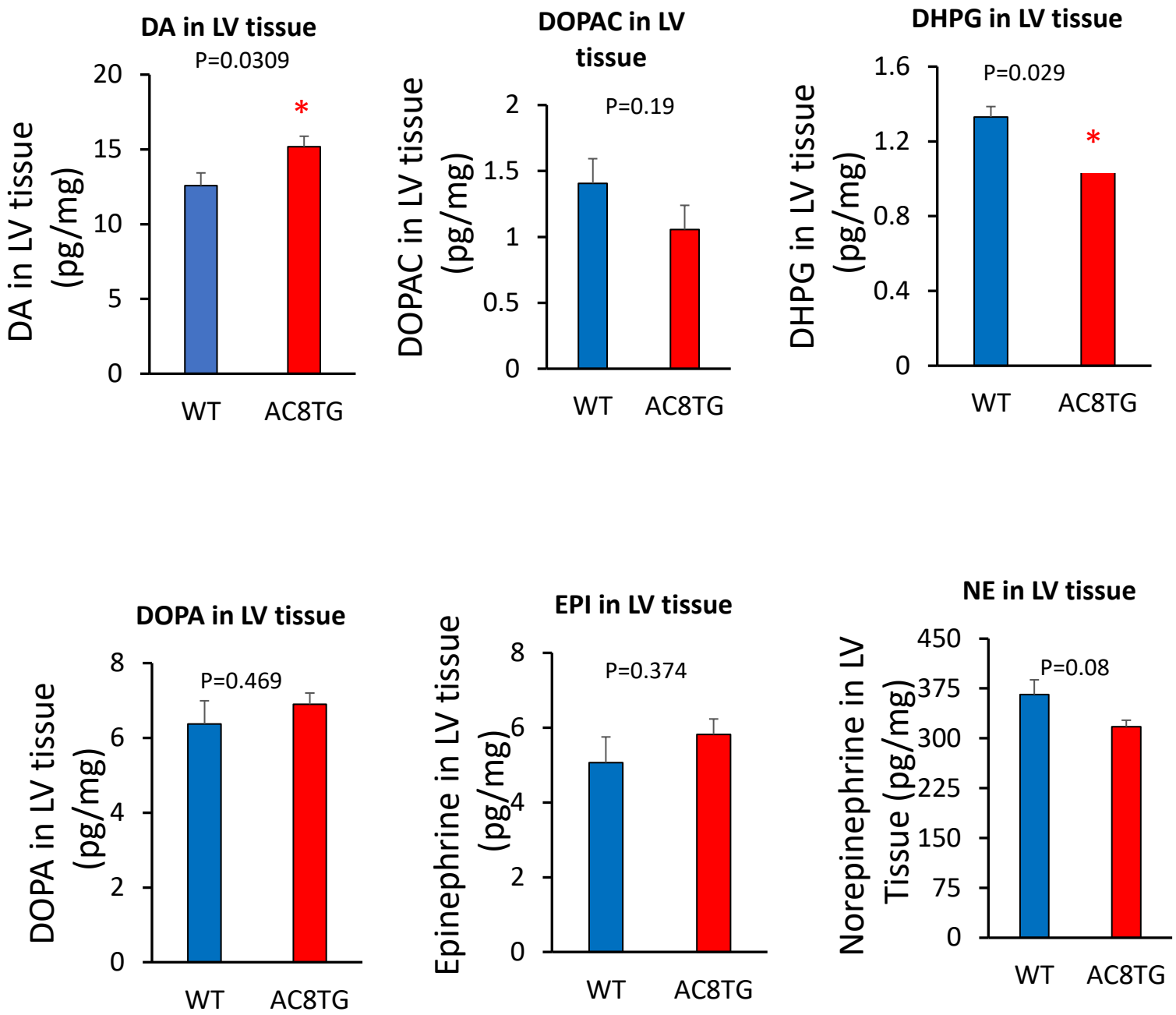

Figure S.3 (C) plasma catecholamine levels. Published in Front Neurosci 2019 Jun 18;13:615

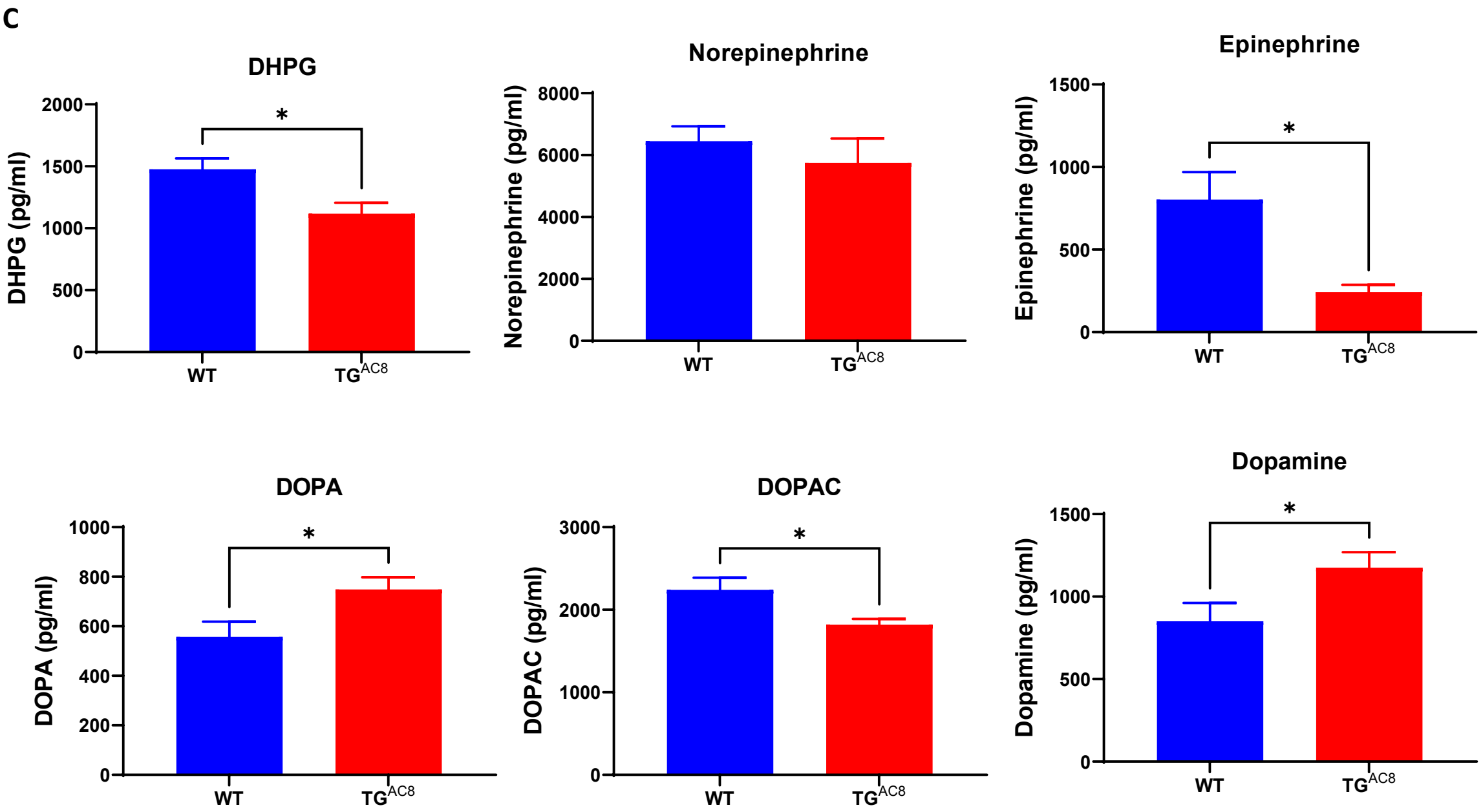

Figure S.4 Volcano plots (A and B) and heat maps of transcripts (C) and proteins (D); (E) expression of mouse and human types of *Adcy8* in LV

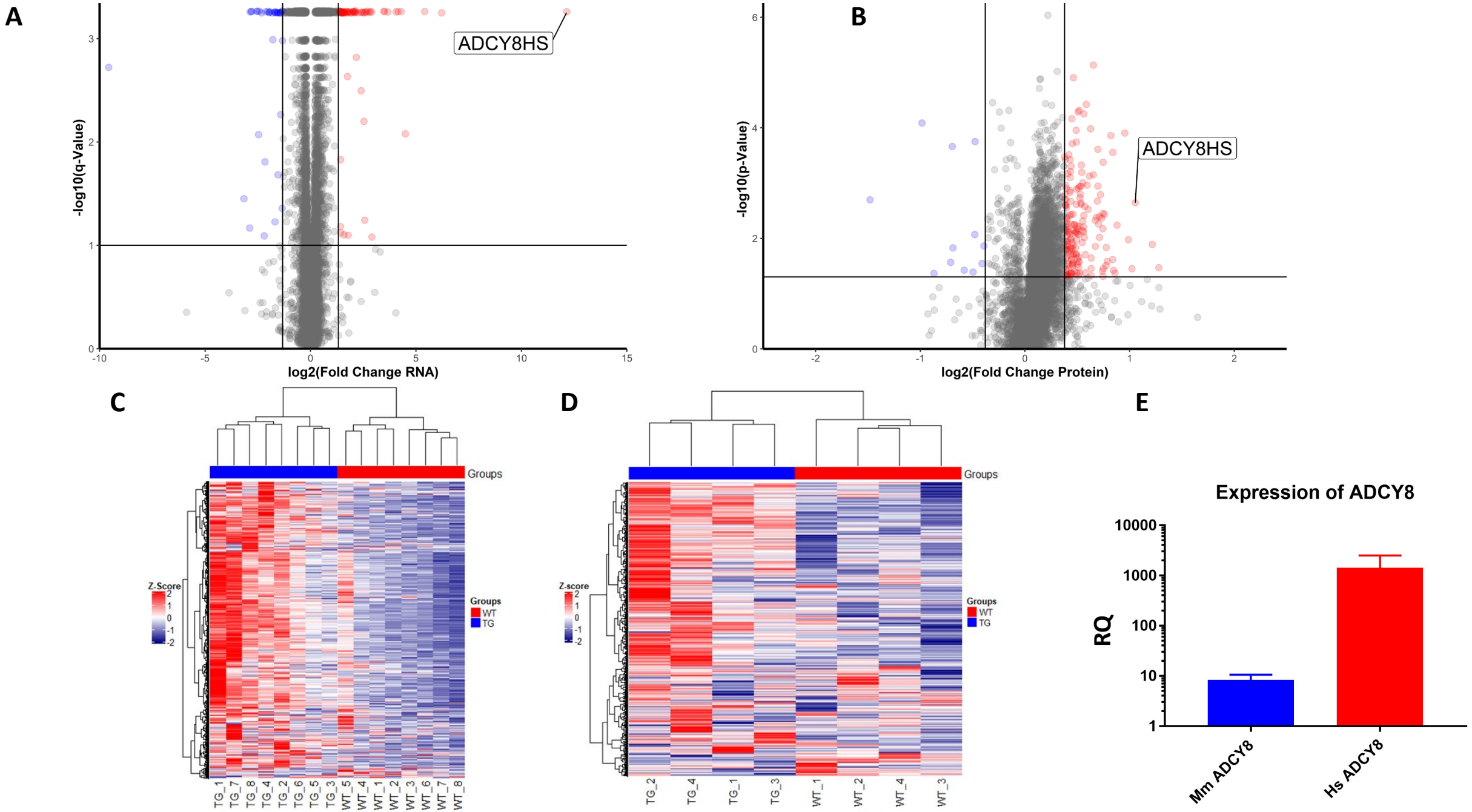

Figure S.5. Plot of the ranks of Z-scores of IPA transcriptome and proteome canonical pathways that significantly differed by genotype.

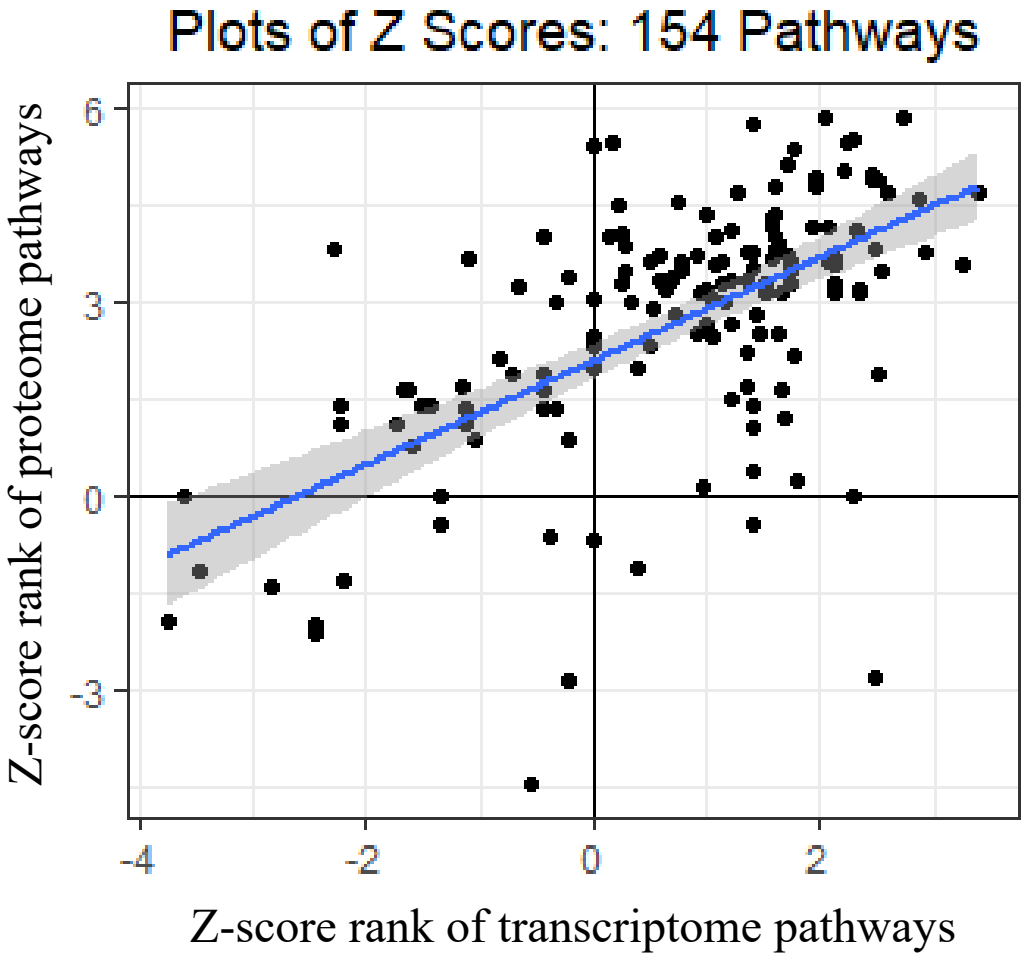

154 pathways in transcriptome or proteome were activated and r_s was 0.57, $p < 0.0001$;

Figure S6. Correlation plot of 544 identified molecules of which *both* transcripts and proteins differed by genotype.

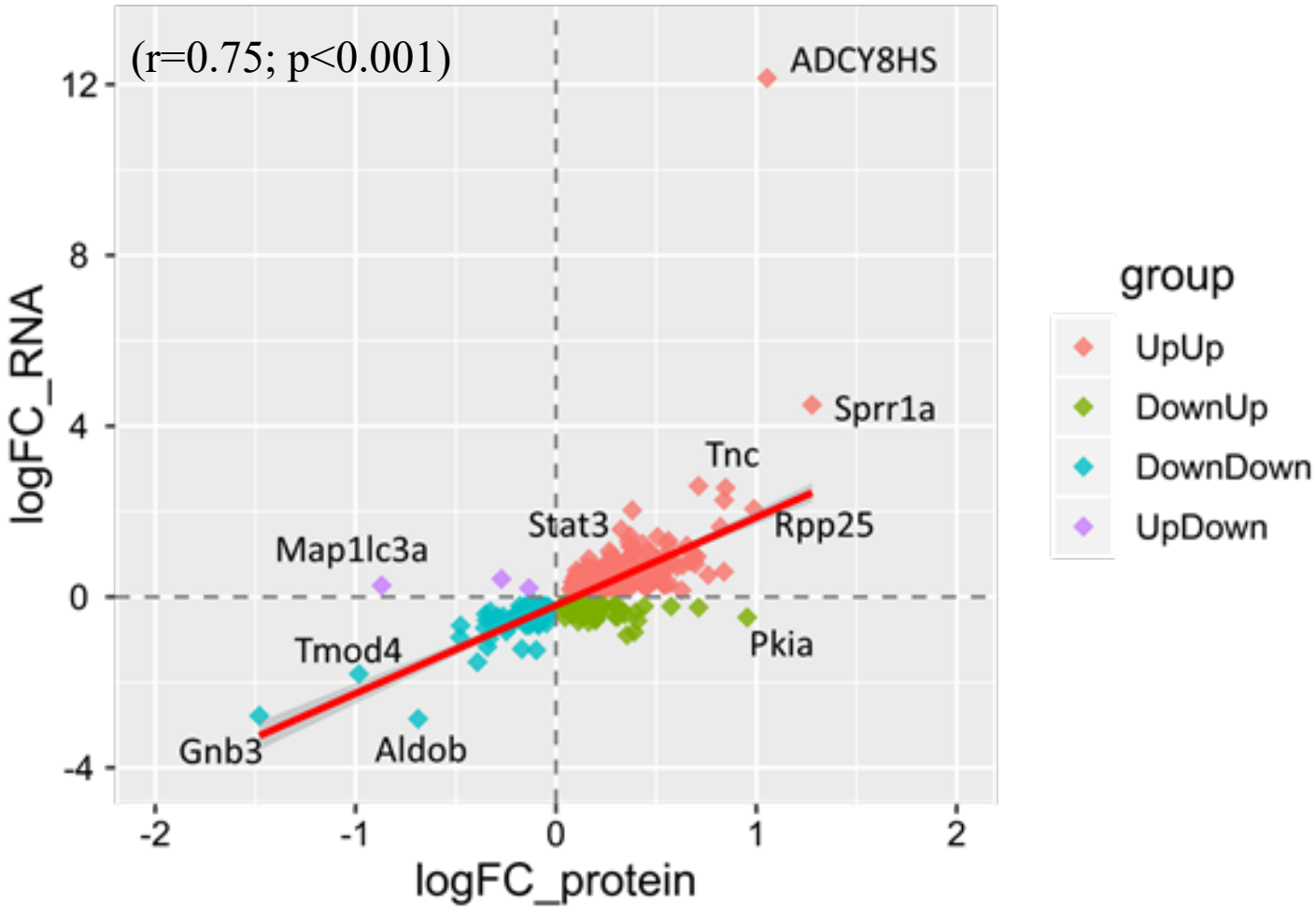

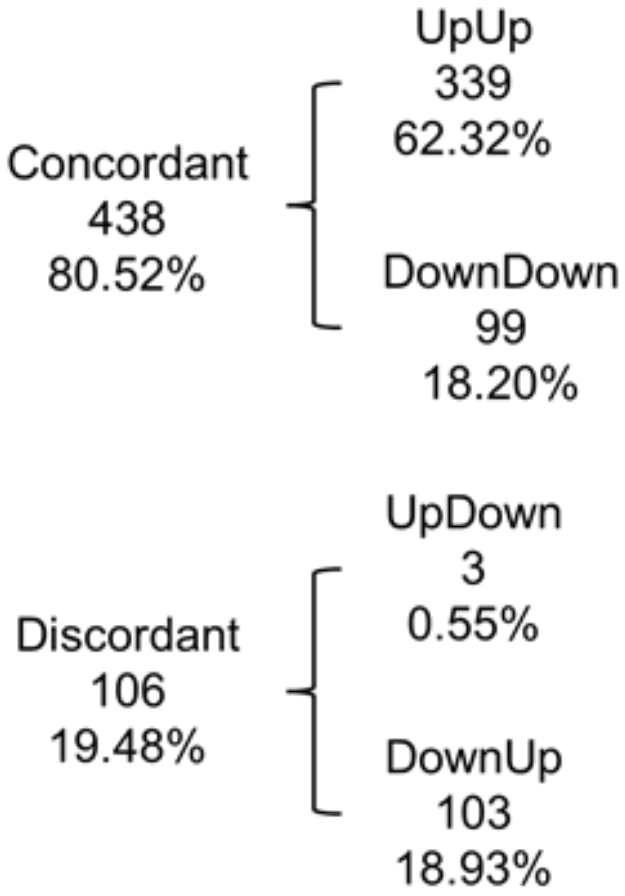

Figure S.7. PROTEOMAP. Areas of polygons within each tier reflect genotypic differences in protein abundances, weighted by protein size.

Tree level:1

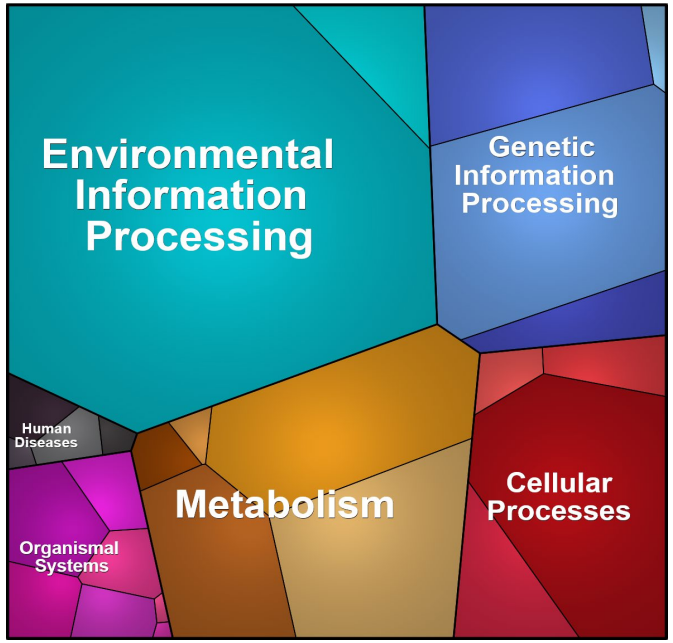

Tree level:2

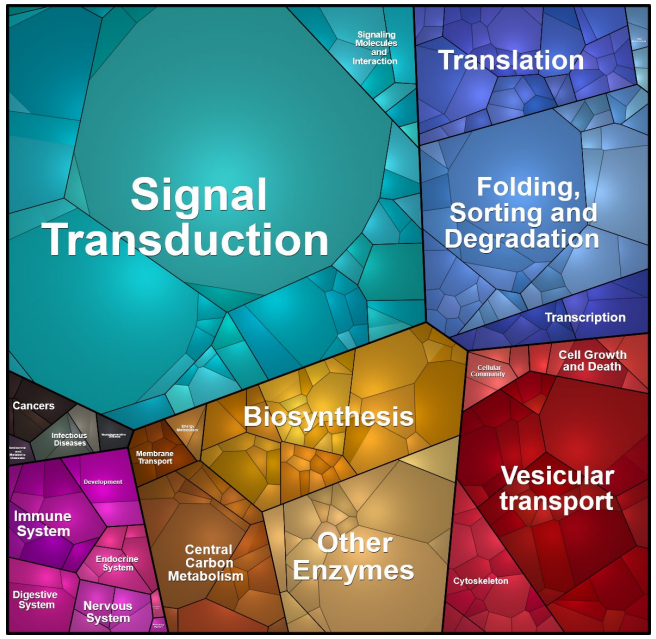

Tree level:3

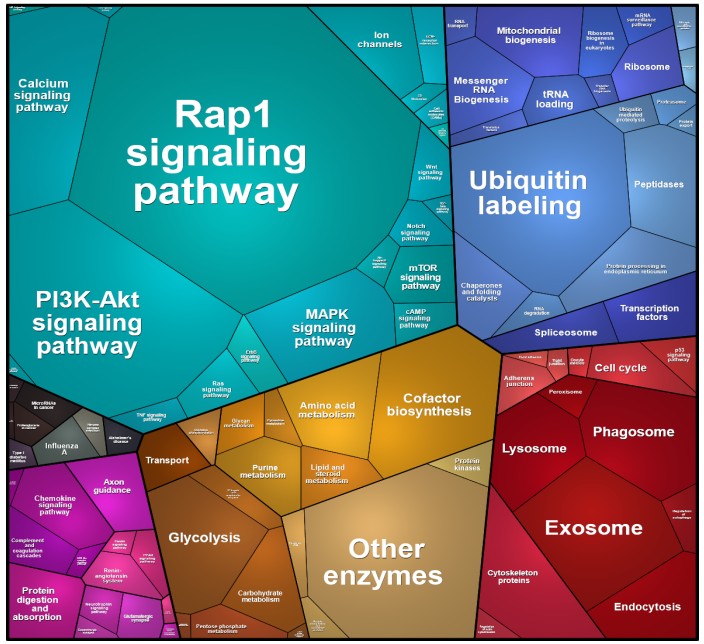

Tree level:4

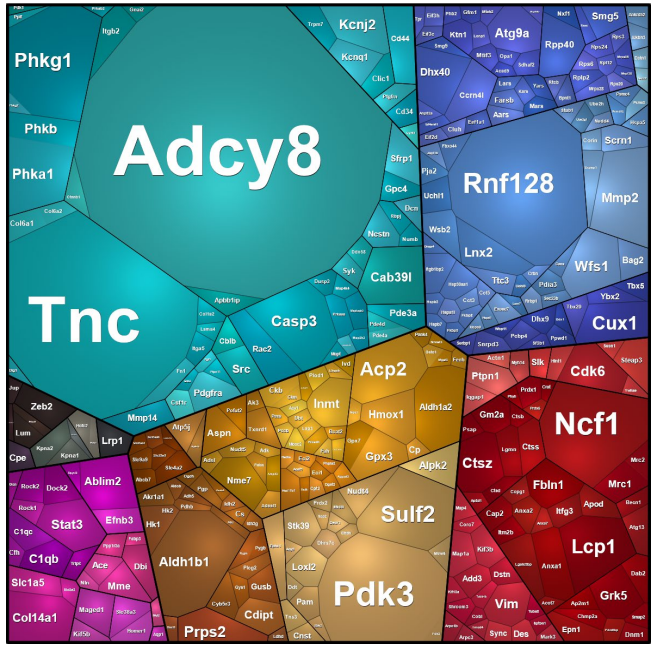

Fig S.8 (A-E) WB and ELISA (F) analyses and of proteins that mediate PIP3 Kinase Signaling and Metabolism

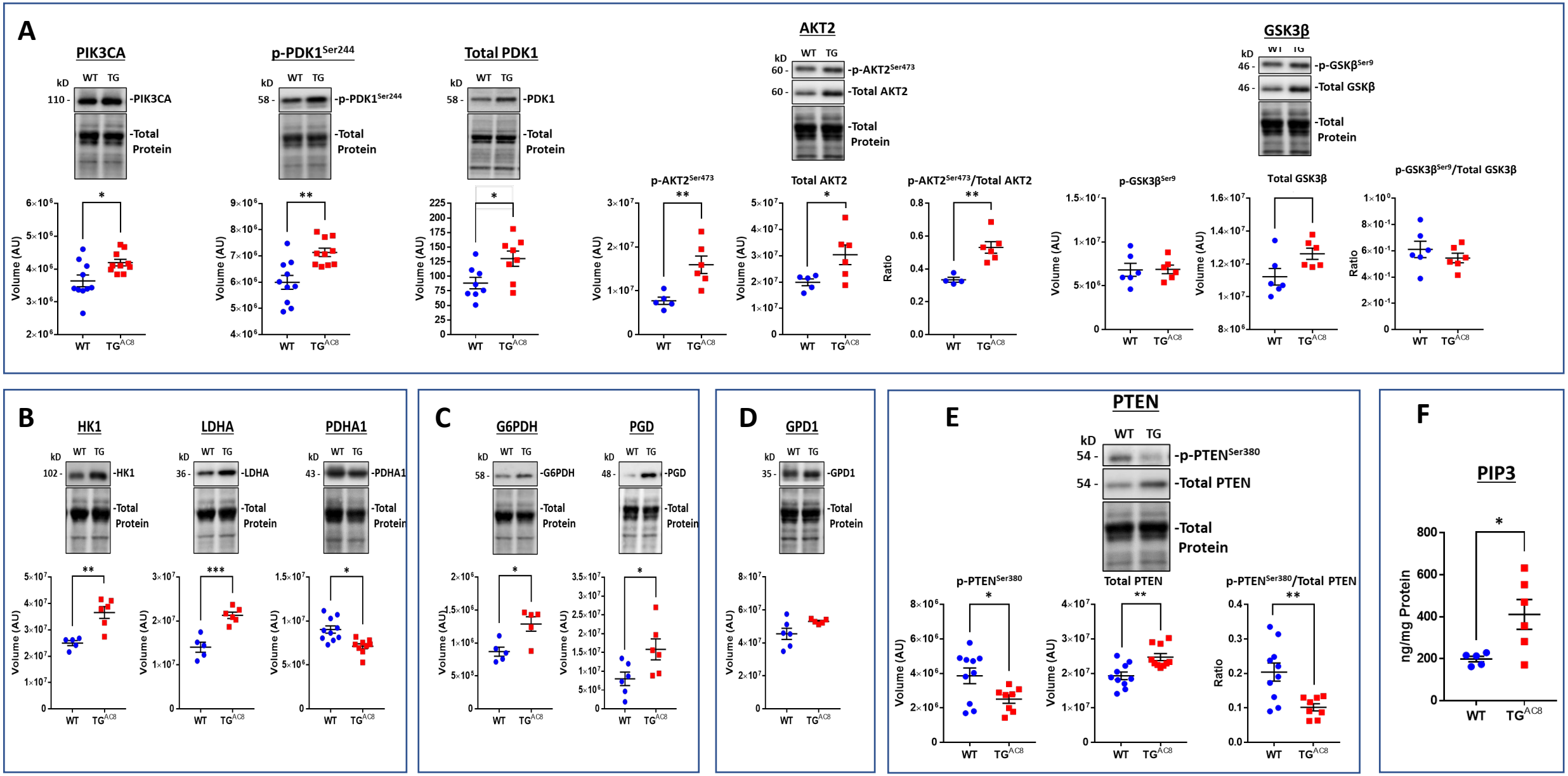

Fig S.9 Detailed schematic malate-aspartate shuttle based on signals derived from bioinformatic analyses of the transcriptome and proteome and on selected WBs.

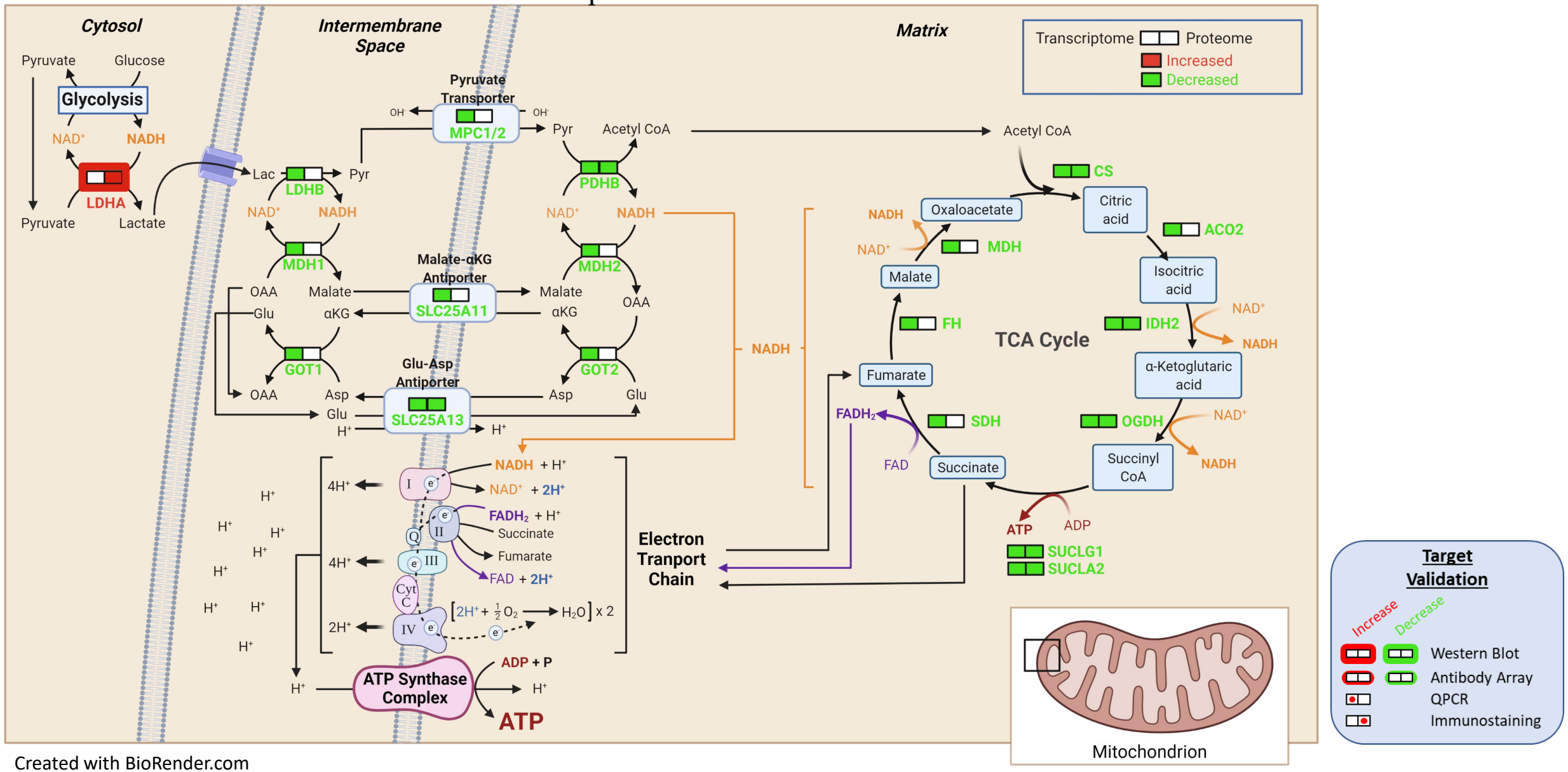

Created with BioRender.com

Figure S.10 Representative examples of (A) ACACB immunolabeling of TG^{AC8} and WT LV myocytes; (B) average ACACB fluorescence in LV cardiomyocytes (n=25 for each group); (C) Relative Quantification of *Acaca* mRNA expression in LV tissue (n=4 for each group).

A

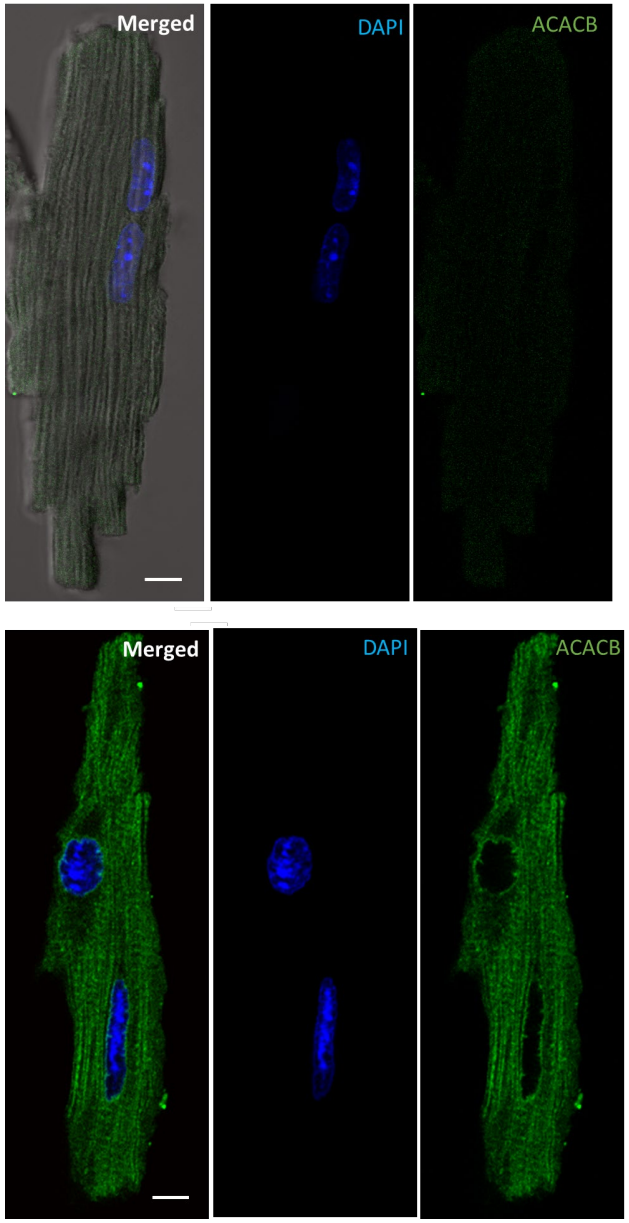

B

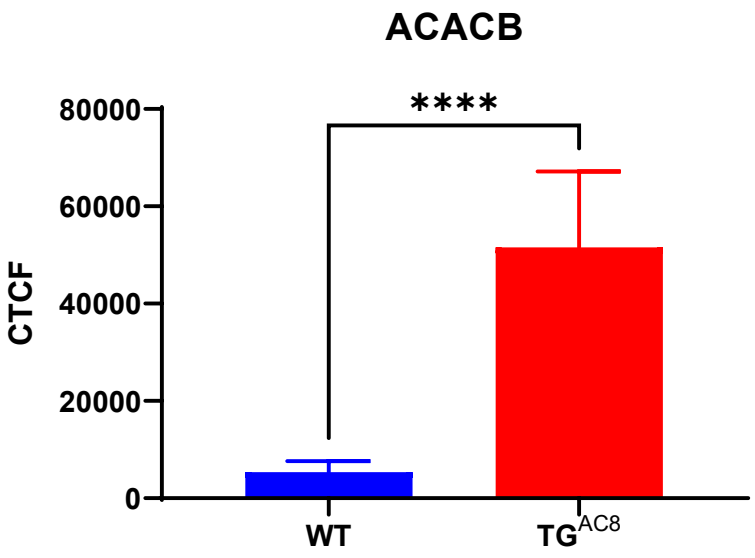

C

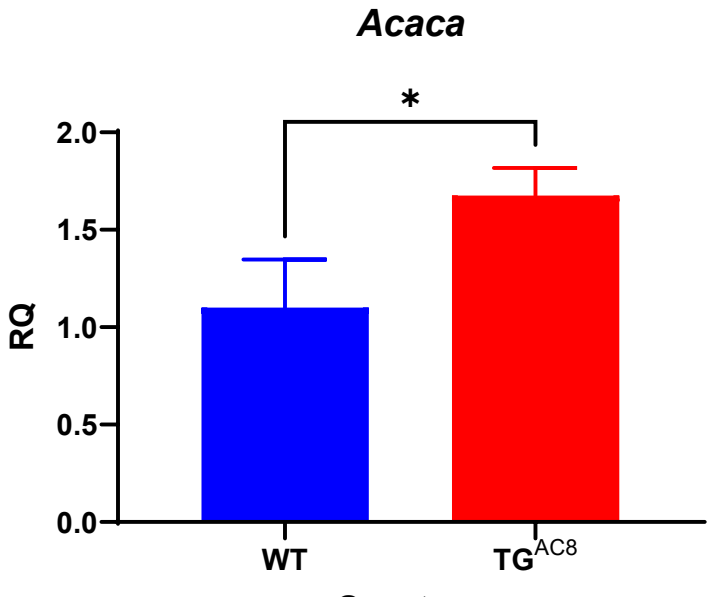

Figure S.11 (A) Negative feedback adaptations on AC/PKA signaling

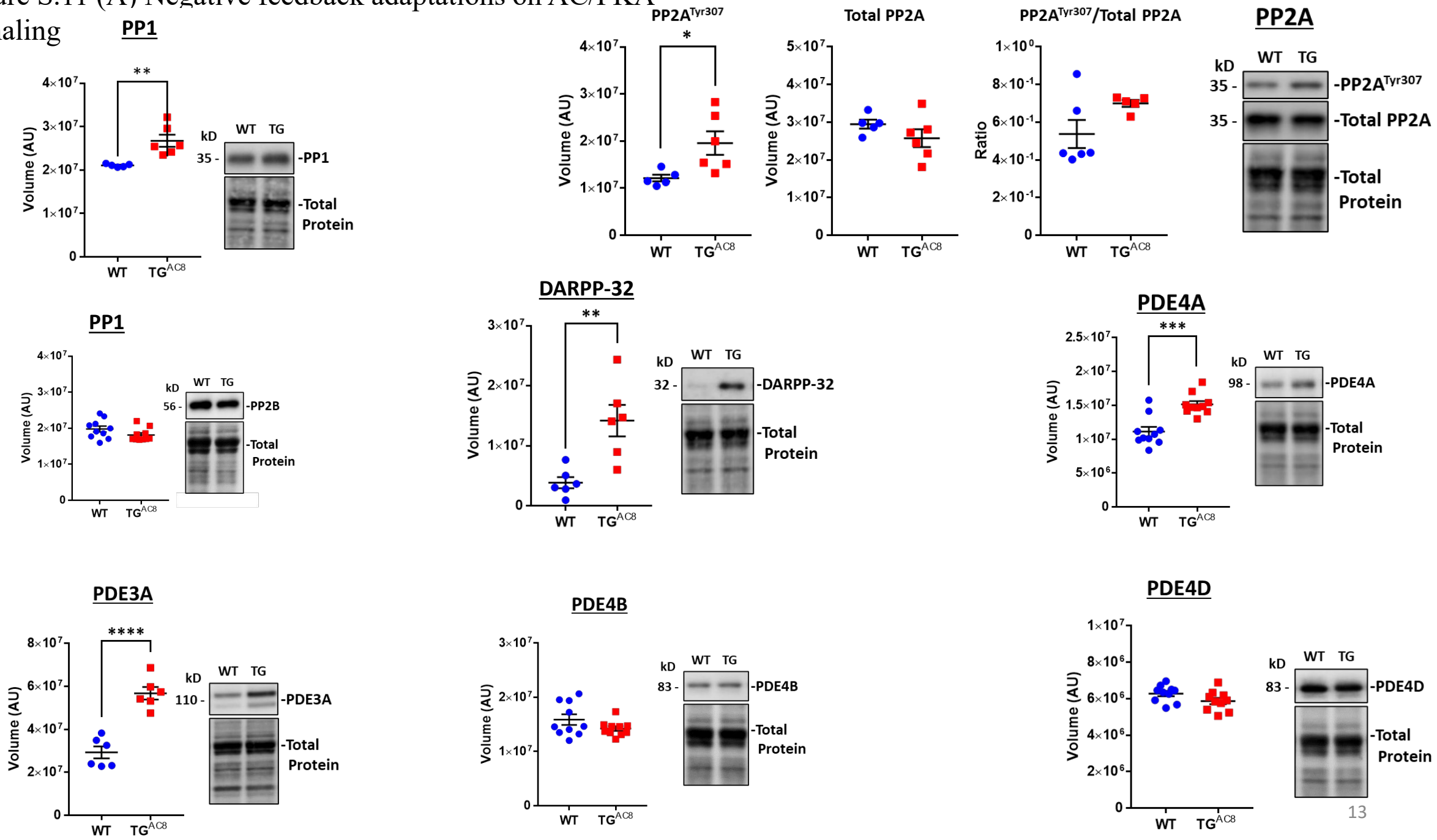

Figure S.11 (B) WB analysis of selected proteins involved in Jak/Stat/Jnk/Caspase signaling

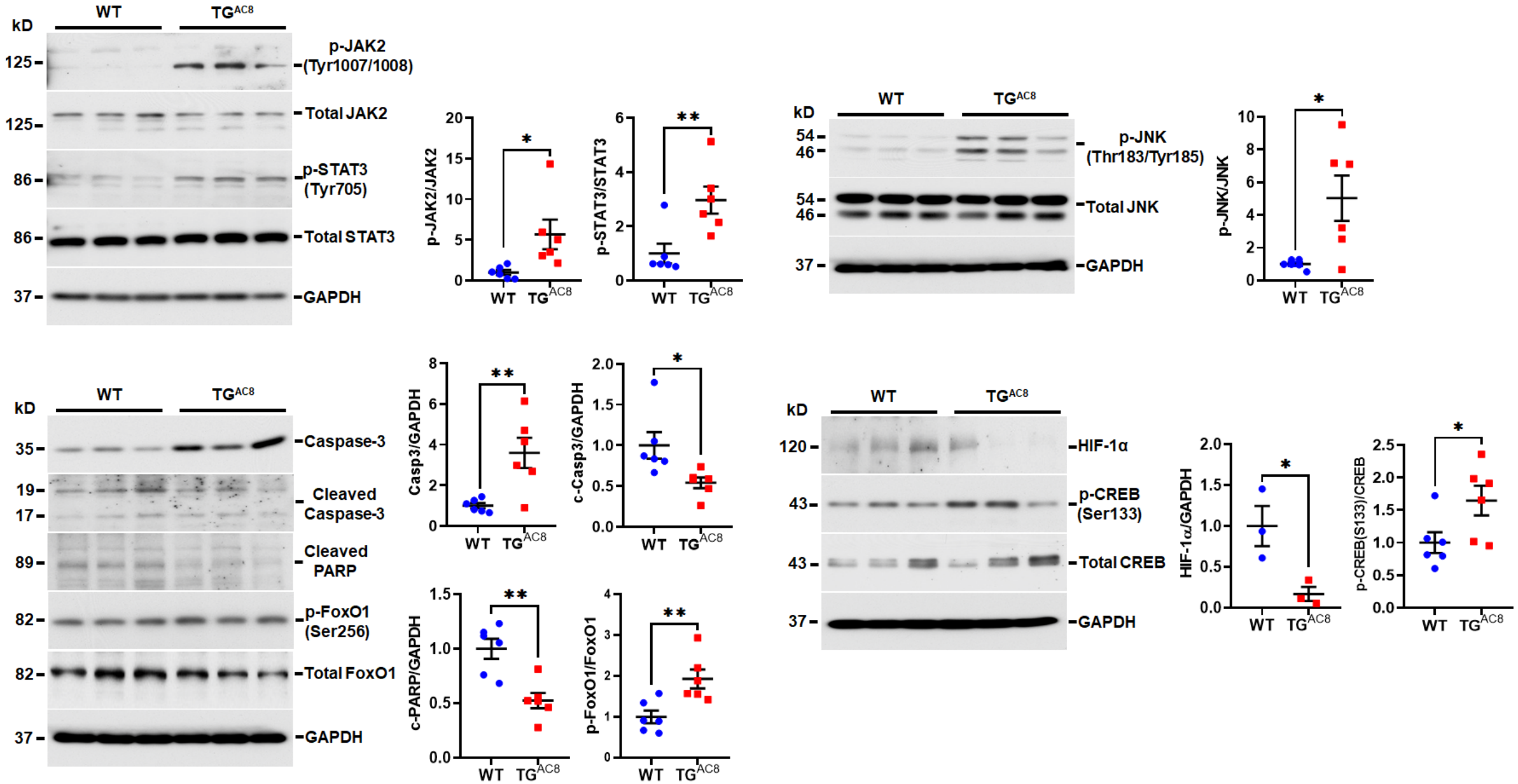

Figure S.11 (C) WB analyses of selected proteins involved in angiotensin receptor signaling

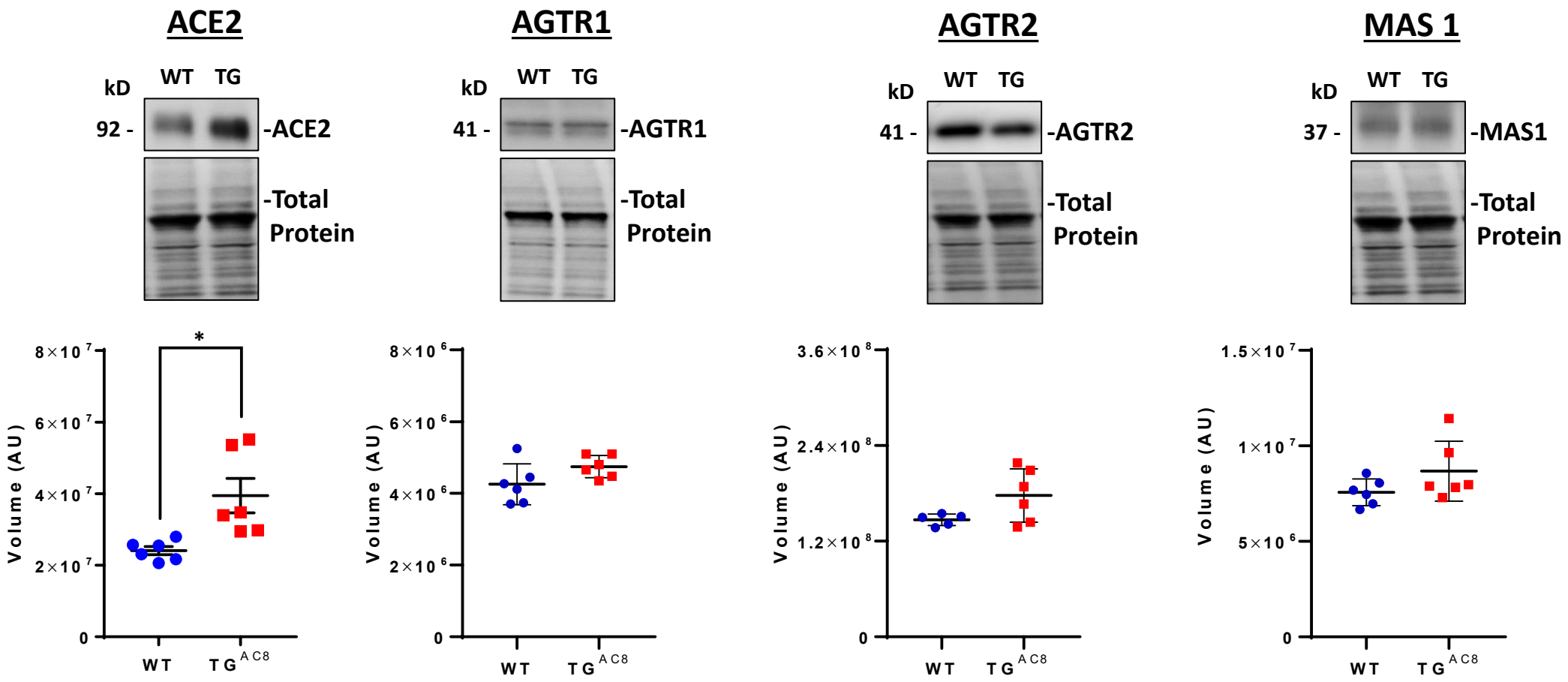

Figure S.11 (D) WB analysis of Calnexin and Calreticulin, proteins involved in ER protein processing.

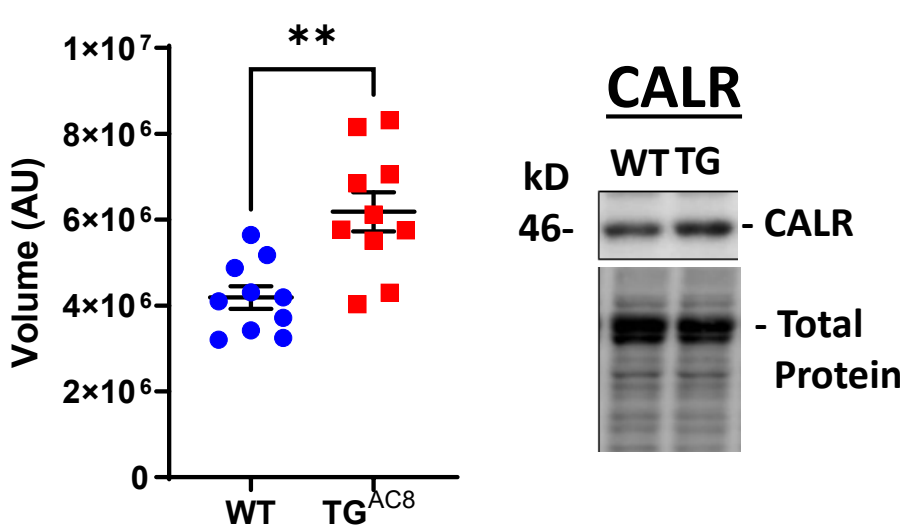

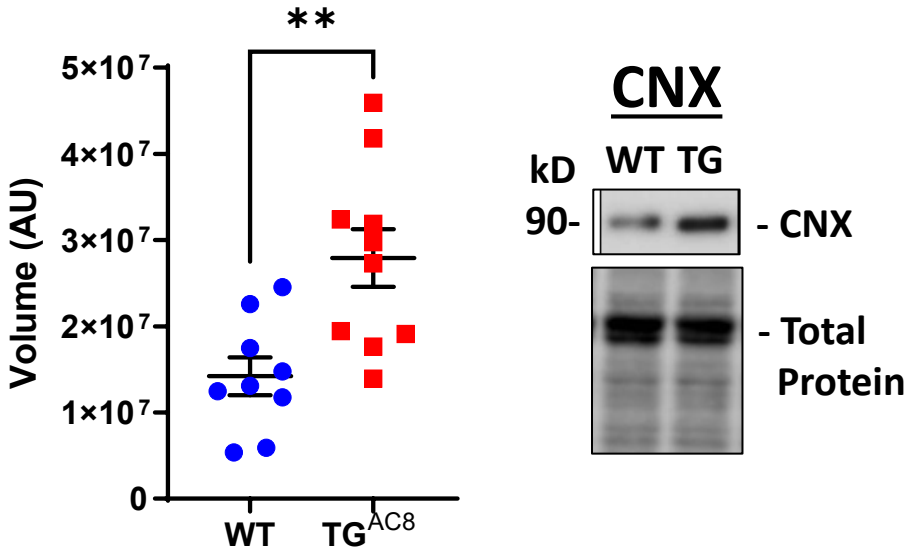

Figure S.12 (A) . QRT-PCR analysis of genes regulating cytokines level in the heart.

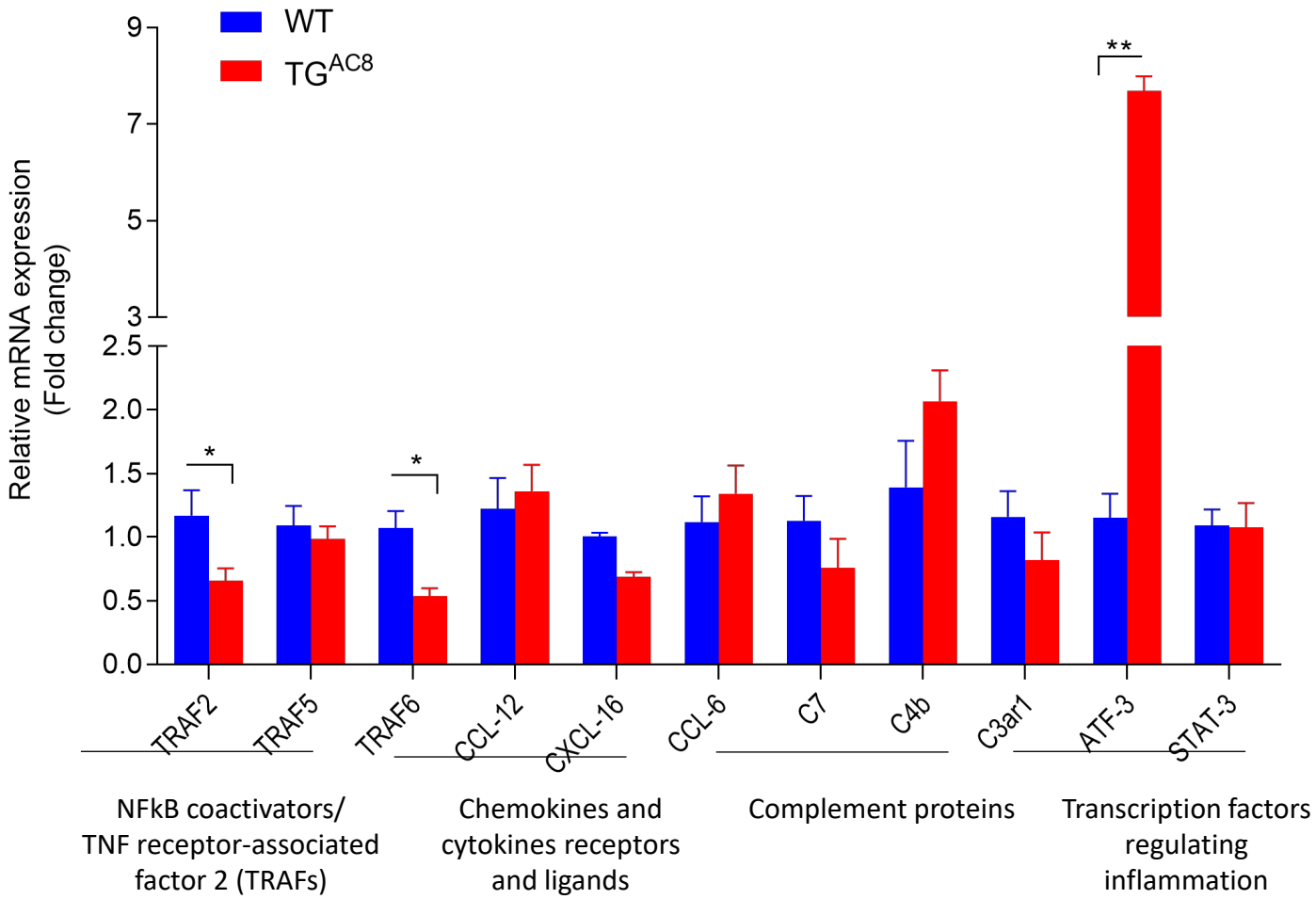

Data are represented as mean± SD (n=5-6). p values are determined using a student's t test.

Figure S.12 (B) Cytokines levels measured from heart tissue lysates.

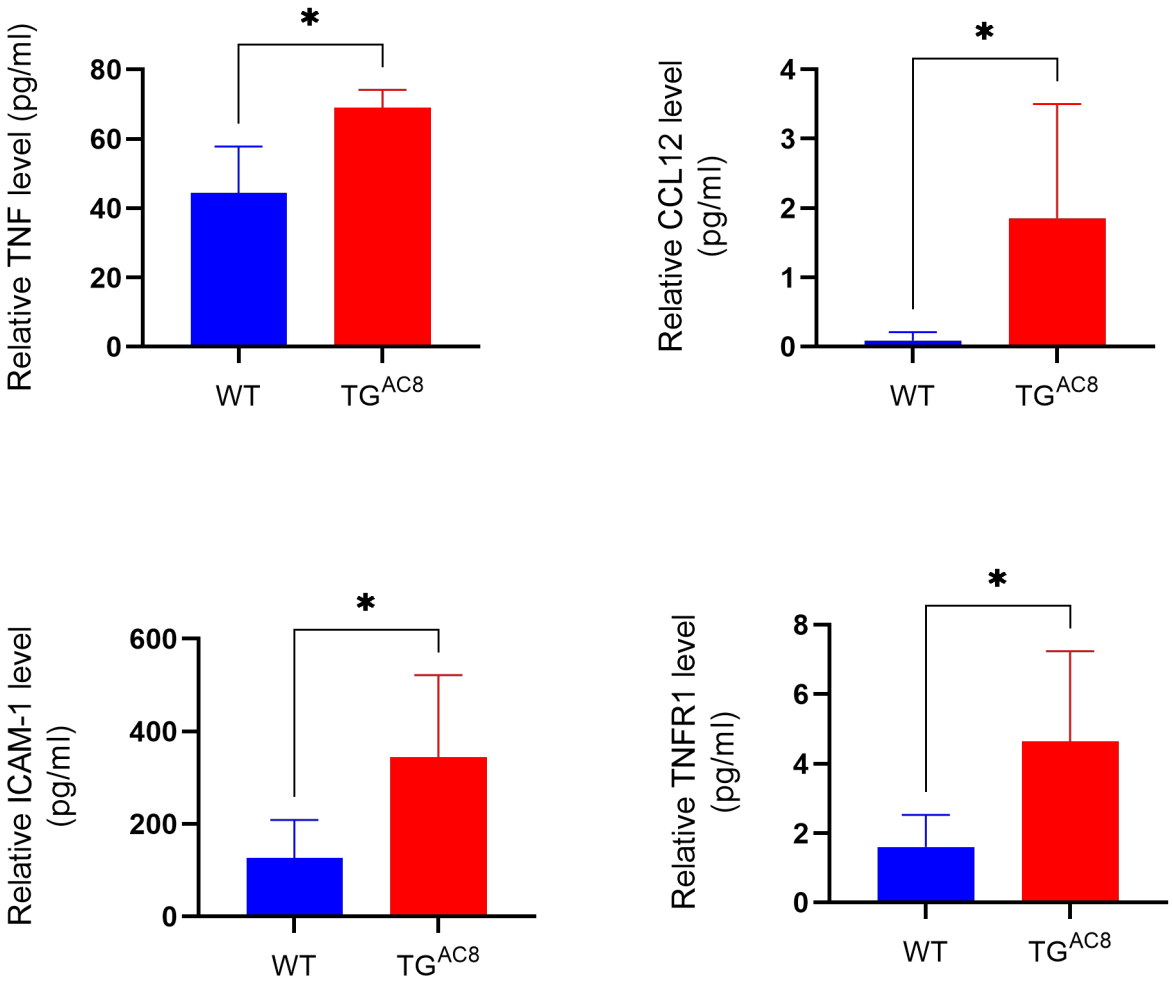

Cytokine levels measured from heart tissue lysates using a Quantibody® Mouse Inflammation Array. Data are represented as mean± SD (n=5). P values are determined using a student's t test.

Figure S. 13 LV Tissue Staining for (A) apoptosis and (B) Glycogen

A

TUNEL

WT LV

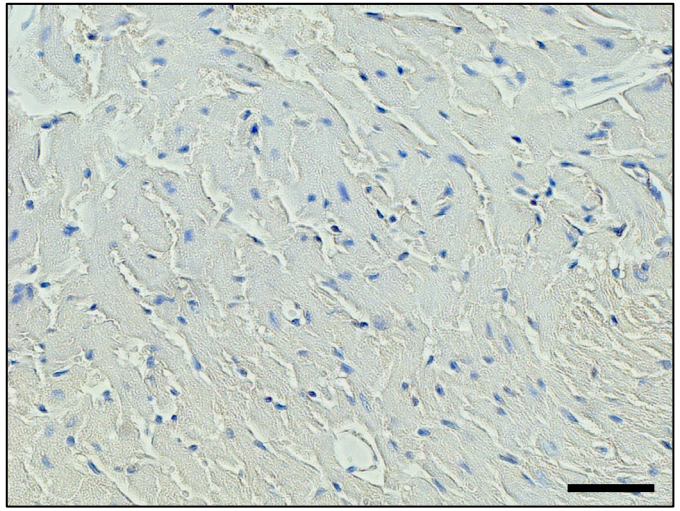

TG^{AC8} LV

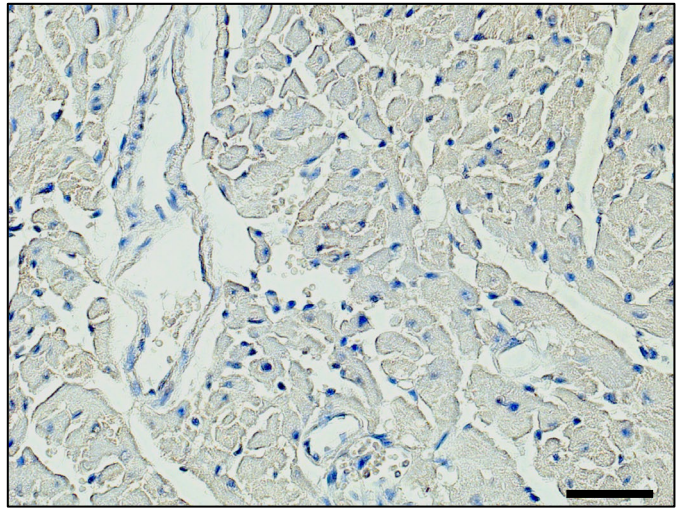

Liver (Positive Control)

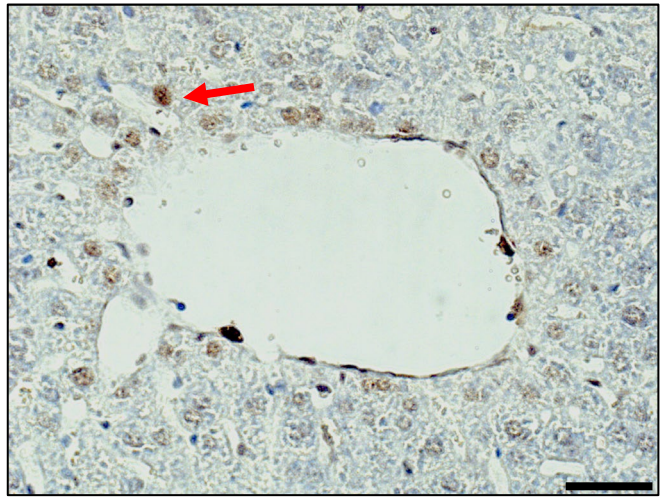

B

PAS

WT LV

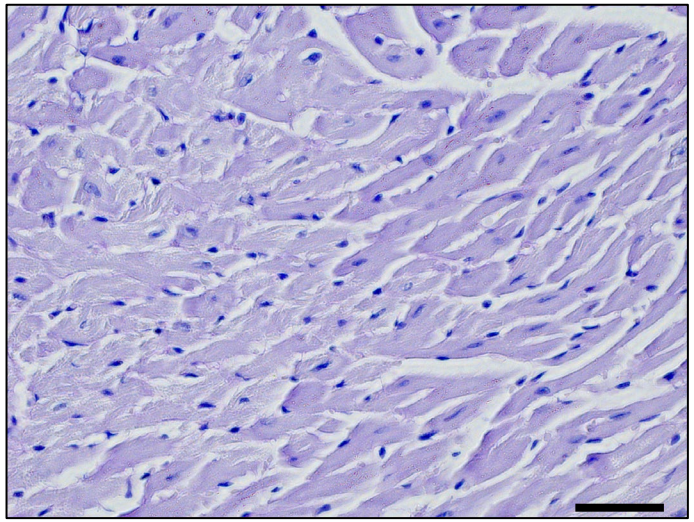

TG^{AC8} LV

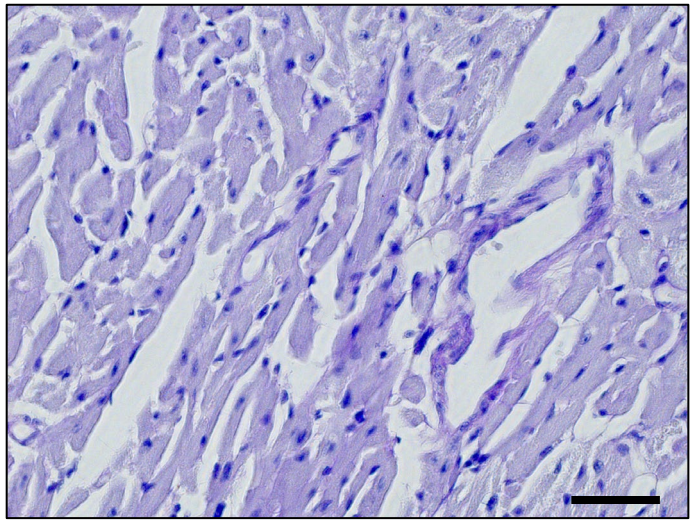

Liver (Positive Control)

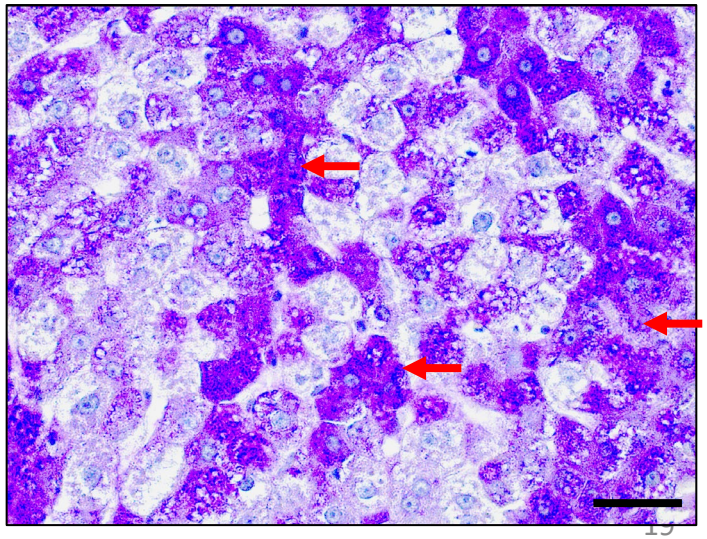

Figure S.14 Periostin levels detected in TGAC8 vs WT LV (Growth Factor Quantibody Array)

A

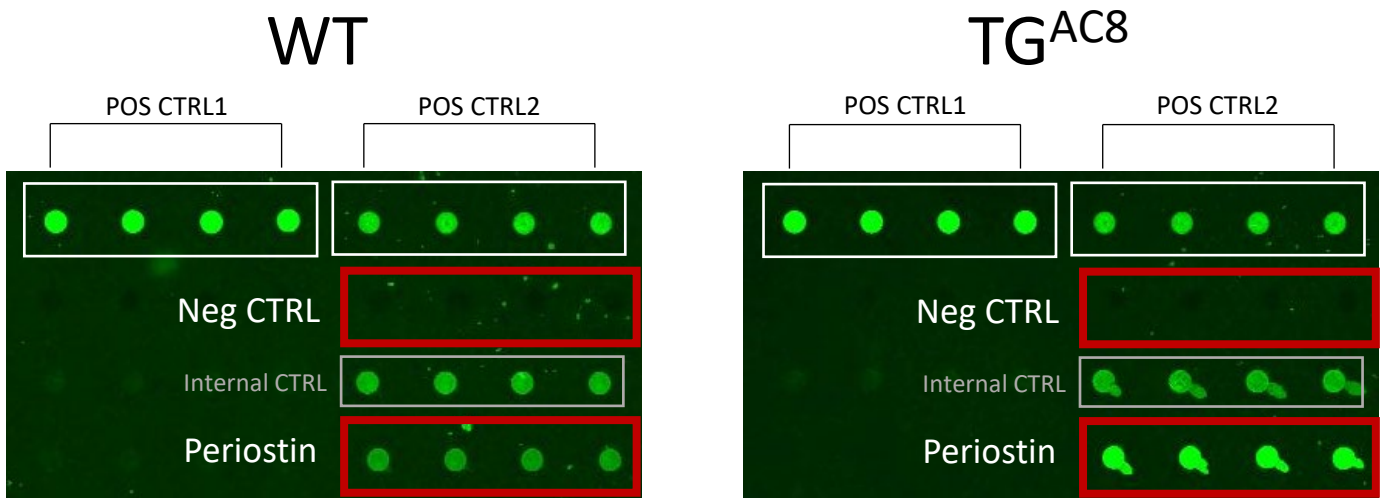

B

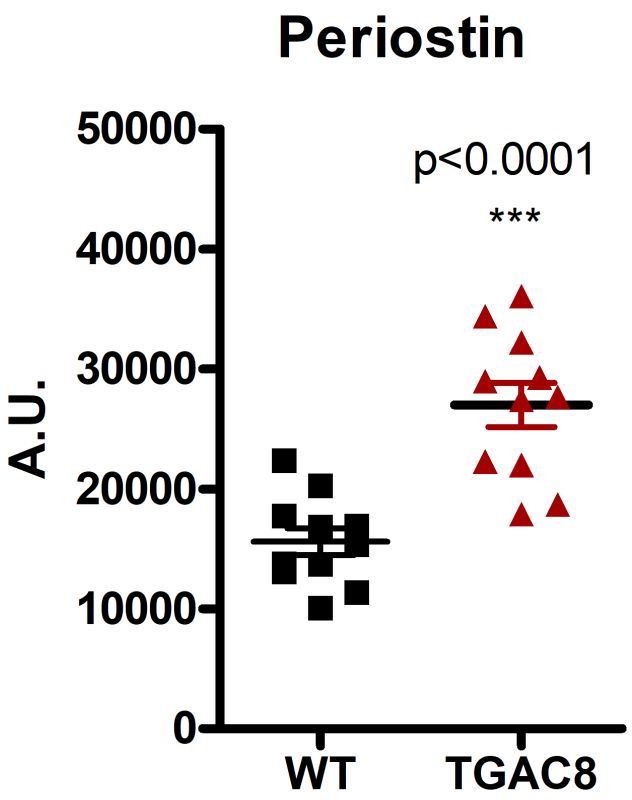

Representative example of the median (fluorescence expression) after subtraction of the background (fluorescence noise). N=12 animals in each group.

Figure S. 15. (A) Sprr1 signaling network. (B) Immunolabeling of Sprr1a in LV myocytes isolated from TG^{AC8} and WT. (C) WB analysis of Rtn4 expression

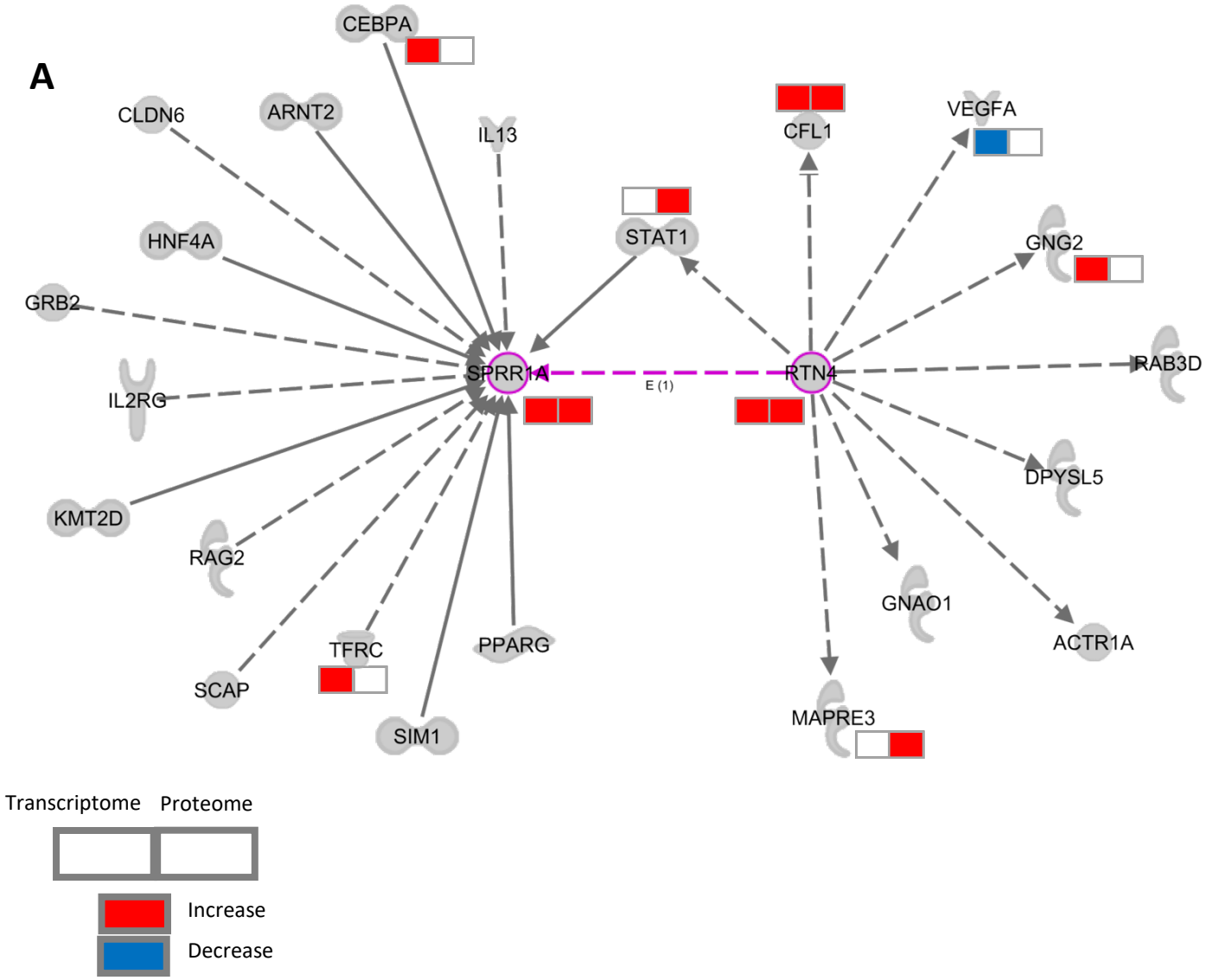

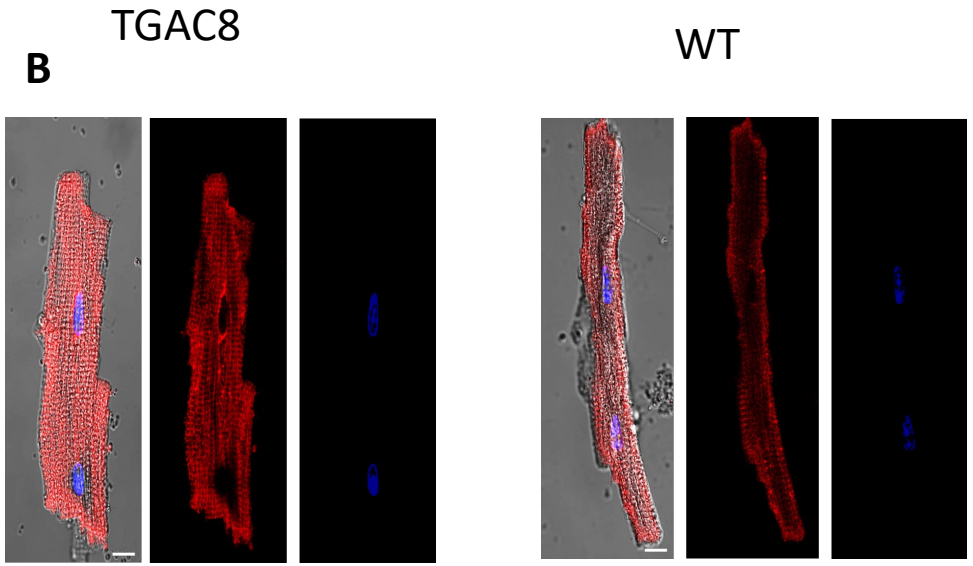

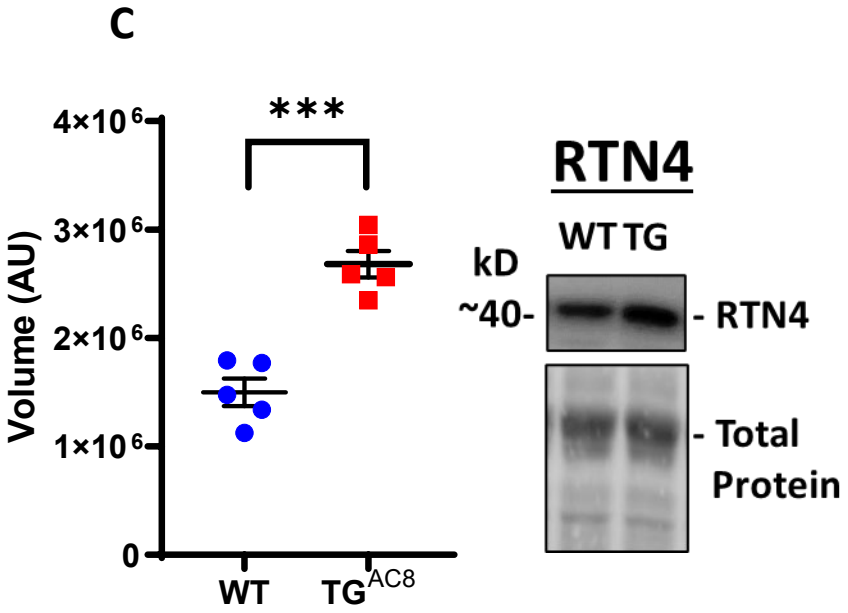
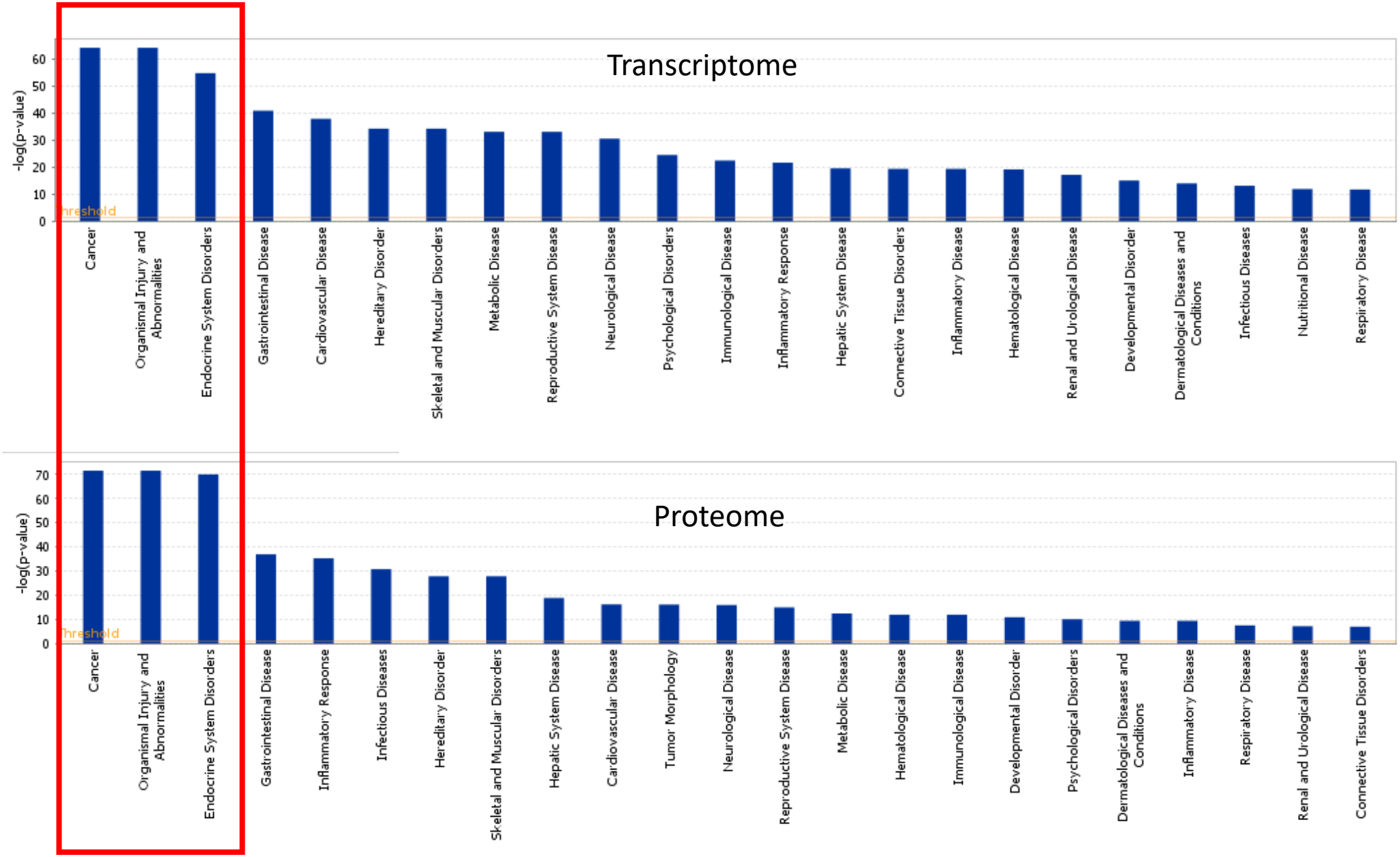
Figure S.16 IPA representation of top Disease-related functions within the LV transcriptome and proteome of TGAC8 and WT.